Small-Scale Gravity Waves generated by Hurricanes in the Upper Troposphere - Lower Stratosphere

Yuying (Alice) Wang

A Thesis Submitted to the Faculty of Graduate Studies
in Partial Fulfillment of the Requirements
for the Degree of Master of Science

Graduate Program in Earth and Space Science
York University
Toronto, Ontario

January 24, 2024

Abstract

In this thesis, we present a detailed study of the small-scale gravity waves in the upper troposphere-lower stratosphere region that are generated by hurricanes. The goal is to understand the spectral properties of the convectively generated gravity waves and their variations with respect to the hurricane intensity.

First, we investigate the gravity wave characteristics for four selected hurricanes using the high vertical resolution temperature measurements from the GPS-Radio Occultation (RO) and the fine horizontal resolution wind data from the ECMWF reanalysis dataset, with the application of the least squares spectral analysis and wavelet analysis. We then examine the variations of the gravity wave characteristics as the hurricane intensity decreases.

Our results show that the pure thermal forcing mechanism generates the primary waves at the surface level in an almost identical way, while the overshooting convection and the background wind filtering seem to weaken as the hurricane intensity drops. The obstacle effect appears to dominate in the lower stratosphere which further contributes to the wave field asymmetry. We then consider a two-layer convection model to simulate the hurricane convection that innovatively connects the wave generation and dissipation mechanisms with the ambient background atmosphere.

This study is important for understanding the couplings between the hurricanes and the lower atmosphere through the vertically propagating gravity waves, which heuristically provides the observational evidence for concepts that were discussed theoretically in the previous studies.

Dedication

To my loving parents,

Lianbin and Xiaojing,

your endless love and support are the greatest inspiration of my life.

Acknowledgements

I would like to express my deepest appreciation to people who have greatly motivated and assisted me during my master studies.

First and foremost, I would like to extend my deepest gratitude to my guide and supervisor Professor Spiros Pagiatakis for his unconditional support, insightful suggestions and continuous encouragement. It has been a great pleasure to learn from his expertise and enthusiasm, which profoundly inspire me in both research and life.

My sincere appreciation goes to Dr. Panagiotis Vergados. I have benefited significantly from his keen perception of research and high-level of professionalism in carrying out this research project.

I am very grateful to my Supervisory Committee member, Professor Yongsheng Chen. His valuable suggestions and answers have been a great contribution to this work.

I wish to thank Professor Gary P. Klaassen for his suggestions in advancing the research methodology of this work.

Special thanks to my thesis examiners Professor Costas Armenakis and Professor William van Wijngaarden for their time to review my thesis and for their constructive comments.

Thanks also to my peers Myrto Tzamali and Nikeet Pandit for their help and accompany.

I would also like to acknowledge that this research was financially supported by an NSERC Discovery Grant held by Professor Pagiatakis.

Finally, my deepest and warmest thanks go to my parents and my partner Fisher, who supported me along the way with their unconditional love and companion.

Contents

Abstract ii

Dedication iii

Acknowledgements iv

Contents v

List of Tables viii

List of Figures ix

1 Introduction 1

1.1 Atmospheric gravity waves 1
1.2 Convection and hurricanes 5
1.3 Overview and scope of the thesis 8

2 Gravity Wave Generation and Dissipation Mechanisms 12

2.1 Gravity wave generation 13
2.2 Gravity wave dispersion relation 16
2.3 Wind filtering effect 22
2.4 Previous work and motivation 25

3 Extraction and Analysis of Wave-induced Perturbations 30

3.1 Introduction to GPS - Radio Occultations 30

3.2 Wave-induced temperature perturbations 34
3.3 Wave-induced vertical wind perturbations 39
3.4 Least squares spectral analysis and wavelet analyses..... 42

4 Gravity Waves Generated by Hurricane Dean (2007) 47

4.1 Eyewall temperature perturbations and thermodynamics..... 48
4.2 Spectral analysis of the GW characteristics and variations..... 51
4.3 Vertical wind perturbations and the GW propagations 54

5 Gravity Waves Generated by Hurricane Julia (2010) 59

5.1 Eyewall temperature perturbations and thermodynamics..... 60
5.2 Spectral analysis of the GW characteristics and variations..... 62
5.3 Vertical wind perturbations and the GW propagations 65

6 Gravity Waves Generated by Hurricane Bill (2009) 68

6.1 Eyewall temperature perturbations and thermodynamics..... 69
6.2 Spectral analysis of the GW characteristics and variations..... 72
6.3 Vertical wind perturbations and the GW propagations 74

7 Gravity Waves Generated by Hurricane Bertha (2008) 77

7.1 Eyewall temperature perturbations and thermodynamics..... 78
7.2 Spectral analysis of the GW characteristics and variations..... 80
7.3 Vertical wind perturbations and the GW propagations 82

8 Comparison of Hurricane Thermodynamics and Gravity Wave Behaviours 85

8.1 Hurricane intensity and eyewall temperature perturbations..... 85
8.2 Hurricane thermodynamics in the eyewall and rainband region.. 90
8.3 Gravity waves in the eyewall and rainband region 93
8.4 Gravity wave intensity and wind perturbations..... 96

9 Comparison of Gravity Wave Variability and Wave Generation Mechanisms **99**

9.1 Gravity wave variability in the eyewall region..... 99

9.2 Gravity wave variability in the rainband region.....103

9.3 Two-layer convection and wave generation mechanism effects..105

10 Conclusions **109**

10.1 Summary 109

10.2 Future work.....113

Bibliography **114**

Appendix A **123**

List of Tables

8.1. A summary of the information for the RO temperature retrievals selected in the eyewall region and the rainband region for different hurricanes. 90

8.2. A summary of the maximum magnitude of the vertical wind perturbations $w'(z)$ for different hurricanes. Maximum values are reported at 10km, 15km and 25km altitude in Pa/s. 96

List of Figures

1.1. The layered structure of the Earth's atmosphere and the vertical variation of the average temperature in the atmosphere (red). 2

1.2. A vertical cross section of the internal structure of a hurricane. The calm and clear core of the hurricane is the eye, which is surrounded by the most convective region called the eyewall. Further from the eye, the warm rising air produces precipitation in the spiral rainbands..... 6

2.1. Determination of the horizontal and vertical wavelength. Lines indicate the constant phase for the wave, λx and λz are the wavelengths in the x and z directions vector (Markowski, & Richardson, 2010). 17

2.2. Energy propagation and phase propagation for an internal gravity wave (Markowski, & Richardson, 2010). 19

2.3. Effects of the background wind filtering on gravity waves. Eastward and westward propagating waves are simulated (black arrows) with varying vertical wavelength (varying arrow length). 23

3.1. Diagram of GPS-RO technique where GPS signals are bent over the horizon (Hand, 2015). Illustrations of the tangent point and the bending angle α are presented as well. 31

3.2. Diagram of GPS-RO with tangent points along the signal path. The retrieved vertical profile is illustrated as the blue dashed line that connects the tangent points. 33

3.3. Diagram of the temperature retrieval selection for the eyewall (blue triangle) and the rainband region (orange triangle). 36

4.1. Best track of Hurricane Dean during Aug. 13-23, 2007. Locations of the temperature retrievals on Aug. 18 in the eyewall region (blue triangle) and in the rainband region (orange triangle) are shown. 47

4.2. Temperature profiles from the RO retrieval at 0:11 UTC on Aug. 18, 2007 inside the eyewall region: (a) the background temperature profile $T0(z)$ (black) and the retrieved temperature profile $T(z)$ inside eyewall (red), (b) the temperature perturbation profile $T'(z)$ (blue) and an attenuating window (grey dashed) and (c) the windowed temperature perturbation profile $T'(z)$..... 49

4.3. (a) Vertical profile of the horizontal background wind speed from ERA5 dataset at 0:00 UTC on Aug. 18, 2007 inside the eyewall region and (b) the normalized least squares wavelet spectrogram of the windowed temperature perturbation $T'(z)$ inside the eyewall.. .. 52

4.4. Vertical wind perturbation w' with the best track of Hurricane Dean (black): (a)-(b) at 25km altitude, (c)-(d) at 15km altitude and (e)-(f) at 10km altitude. The blue triangle denotes the recorded eye location at 0:00 UTC and the black arrows indicate the propagation direction of GWs. Left and right columns are captured at 0:00 and 2:00 UTC on Aug. 18, respectively. 55

5.1. Best track of Hurricane Julia during Sept.12-25, 2010. Locations of the temperature retrievals on Sept. 14 in the eyewall region (blue triangle) and in the rainband region (orange triangle) are shown. 59

5.2. Temperature profiles from the RO retrieval at 16:45 UTC on Sept. 14, 2010 inside the eyewall region: (a) background temperature profile $T0(z)$ (black) and retrieved temperature profile $T(z)$ inside eyewall (red), (b) temperature perturbation profile $T'(z)$ (blue) and an attenuating window (grey dashed) and (c) the windowed temperature perturbation profile $T'(z)$..... 60

5.3. (a) Vertical profile of the horizontal background wind speed from ERA5 dataset at 17:00 UTC on Sept. 14, 2010 in the eyewall region and (b) the normalized least squares wavelet spectrogram of the windowed temperature perturbation $T'(z)$ inside the eyewall.. .. 63

5.4. Vertical wind perturbation w' with the best track of Hurricane Julia (black): (a)-(b) at 25km altitude, (c)-(d) at 15km altitude and (e)-(f) at 10km altitude. The blue triangle denotes the recorded eye location at 18:00 UTC and the black arrows indicate the propagation direction of GWs. Left and right columns are captured at 17:00 and 19:00 UTC on Sept. 14, respectively. 66

6.1. Best track of Hurricane Bill during Aug. 15-26, 2009. Locations of the temperature retrievals on Aug. 17 in the eyewall region (blue triangle) and in the rainband region (orange triangle) are shown. 69

6.2. Temperature profiles from the RO retrieval at 13:35 UTC on Aug. 17, 2009 inside the eyewall region: (a) the background temperature profile $T0(z)$ (black) and the retrieved temperature profile $T(z)$ inside eyewall (red), (b) the temperature perturbation profile $T'(z)$ (blue) and an attenuating window (grey dashed) and (c) the windowed temperature perturbation profile $T'(z)$..... 70

6.3. (a) Vertical profile of horizontal background wind speed from ERA5 dataset at 14:00 UTC on Aug. 17, 2009 in the eyewall region and (b) the normalized least squares wavelet spectrogram of the windowed temperature perturbation $T'(z)$ inside the eyewall. 72

6.4. Vertical wind perturbation w' with the best track of Hurricane Bill (black): (a)-(b) at 25km altitude, (c)-(d) at 15km altitude and (e)-(f) at 10km altitude. The blue triangle denotes the recorded eye location at 12:00 UTC and the black arrows indicated the propagation direction of GWs. Left and right columns are captured at 13:00 and 15:00 UTC on Aug. 17, respectively. 75

7.1. Best track of Hurricane Bertha during July 3-21, 2008. Locations of the temperature retrievals on July 8 in the eyewall region (blue triangle) and in the rainband region (orange triangle) are shown. 77

7.2. Temperature profiles from the RO retrieval at 14:19 UTC on July 8, 2008 inside the eyewall region: (a) the background temperature profile $T0(z)$ (black) and the retrieved temperature profile $T(z)$ inside the eyewall (red), (b) the temperature perturbation profile $T'(z)$ (blue) and an attenuating window (grey dashed) and (c) the windowed temperature perturbation profile $T'(z)$..... 79

7.3. (a) Vertical profile of horizontal background wind speed from ERA5 dataset at 14:00 UTC on July 8, 2008 in the eyewall region and (b) the normalized least squares wavelet spectrogram of the windowed temperature perturbation $T'(z)$ inside the eyewall. 80

7.4. Vertical wind perturbation w' with the best track of Hurricane Bertha (black): (a)-(b) at 25km altitude, (c)-(d) at 15km altitude and

(e)-(f) at 10km altitude. The blue triangle denotes the recorded eye location at 0:00h UTC on July 10 and the black arrows indicate the propagation direction of the GWs. Left and right columns are captured at 21:00h and 23:00h UTC on July 9, respectively. 83

8.1. The background temperature profiles (black) and the individual temperature profiles (red) in the eyewall region of different hurricanes: (a) Dean, (b) Julia, (c) Bill and (d) Bertha. The normal tropopause level (orange dashed) for each hurricane is illustrated as well. 87

8.2. The temperature perturbation profiles (blue) in the eyewall region of different hurricanes: (a) Dean, (b) Julia, (c) Bill and (d) Bertha. The mean (black dashed), standard deviation (gray shaded) and the normal tropopause level (orange dashed) are also shown for each perturbation. 87

8.3. Comparisons of the windowed temperature perturbations induced in the eyewall (blue) and in the rainband region (orange) of different hurricanes: (a) Dean, (b) Julia, (c) Bill and (d) Bertha. 91

8.4. Differences of the windowed temperature perturbations (green) between eyewall and the rainband region of different hurricanes: (a) Dean, (b) Julia, (c) Bill and (d) Bertha. The mean (black dashed) and standard deviation (gray shaded) of each perturbation profile are also shown. 91

8.5. Comparisons of the least squares spectra for the windowed temperature perturbations in the eyewall (blue) and the rainband region (orange), as well as their spectra product (green) for different hurricanes: (a)-(b) Dean, (c)-(d) Julia, (e)-(f) Bill and (g)-(h) Bertha. The threshold of significance for each spectrum (gray dashed) at the 99% confident level is also shown. 94

9.1. Normalized least squares wavelet spectrograms of the windowed temperature perturbation $T'(z)$ inside the eyewall of different hurricanes: (a) Dean, (b) Julia, (c) Bill and (d) Bertha. The estimated tropopause level (white dashed) is also shown. 100

9.2. Normalized least squares wavelet spectrograms of the windowed temperature perturbation $T'(z)$ in the rainband region of different

hurricanes: (a) Dean, (b) Julia, (c) Bill and (d) Bertha. The estimated tropopause level (white dashed) is also shown.....103

9.3. Diagram of two-layer convection that simulates the convective regime of hurricanes. 106

Chapter 1

Introduction

1.1 Atmospheric gravity waves

The Earth's atmosphere can be considered as a stably stratified fluid with a density decreasing exponentially with height. Based on the vertical variations of the temperature, the atmosphere can be divided into layers. *Troposphere* is the lowest part of the Earth's atmosphere where most weather systems occur. The top of the troposphere is called *tropopause*, which has a minimum height of about 10km. The temperature in the troposphere decreases with the increasing altitude (Hewitt & Jackson, 2003).

Stratosphere is the region above the troposphere, which extends from the tropopause to an altitude of about 50km. The temperature in the stratosphere usually increases with height to a maximum value at the *stratopause*. This increase is caused by the ozone layer that absorbs the solar ultraviolet radiation (Hewitt & Jackson, 2003).

The region above the stratopause is called *mesosphere* where the temperature decreases with height again, because the cooling processes above 50km altitude are stronger than the warming caused by the absorption of the ultraviolet radiation. The minimum temperature in the mesosphere occurs at its upper boundary, namely the *mesopause*, which separates the mesosphere from the upper layers (ibid., 2003).

Thermosphere is the region that lies above the mesopause, where the temperature increases with height again. The region above 80km altitude is called *ionosphere*, where

the solar radiation excites the electrically neutral atoms and produces ions. The temperature in the ionosphere increases with height due to the release of energy from the ionization processes (ibid., 2003).

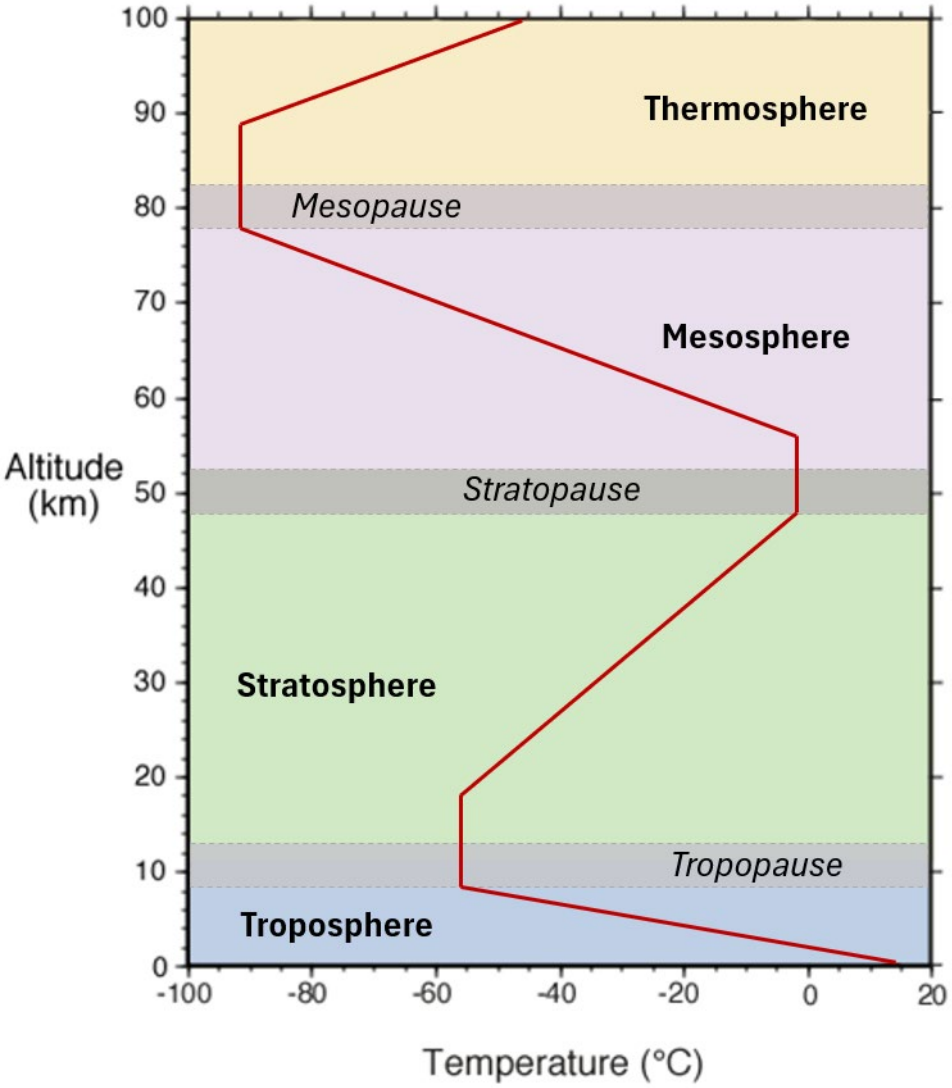

Figure 1.1. The layered structure of the Earth's atmosphere and the vertical variation of the average temperature in the atmosphere (red).

Within such a stratified atmosphere, a*tmospheric gravity waves* are generated when an air parcel is displaced from its equilibrium position. The *surface gravity waves*, or the external gravity waves are formed along the interface between the stratified layers. In contrast, the *internal gravity waves*, which are of our interest, oscillate within the stratified

layer with a restoring force of buoyancy and gravity (Markowski & Richardson, 2010). For simplicity, we will refer to the internal gravity waves as *gravity waves* (GWs).

A variety of sources can generate GWs, such as topography, wind shear and convection (Fritts & Alexander, 2003). Mountain waves are typical examples of topographically generated GWs, with a horizontal wavelength of tens to hundreds of kilometers. Unstable shears can also excite GWs, which are difficult to model due to their timescales. Likewise, convection can generate GWs through different mechanisms with a wide spectrum of frequencies (ibid., 2003).

Among the GWs generated by different sources, our study focuses on the vertically propagating, internal gravity waves that are generated via convection in the atmosphere. These *convectively generated gravity waves* (CGWs) are on a smaller scale (a time period less than a few hours with a horizontal wavelength smaller than 400km or a vertical wavelength of about 2-10km) compared to the large-scale gravity waves (a horizontal wavelength exceeding 1000km), which have profound effects in the mean circulation of the middle atmosphere (Kuester et al., 2008; Guo et al., 2019; Song et al., 2021).

CGWs are usually related to the weather systems in the troposphere with a time-dependent thermal forcing that cannot be easily quantified (Fritts & Alexander, 2003; Wang et al., 2021). For instance, deep convection associated with storms and hurricanes is an important convective source of our interest, which generates GWs via nonlinear heat flux and the heat release (Alexander & Holton, 2004; Müller et al., 2018; Shi et al., 2021).

Mathematically, a GW perturbation can be described by wave number components (k, l, m) in Cartesian coordinates (x, y, z) and a ground-based (ground-referenced) angular frequency ω. The term *intrinsic frequency* $\hat{\omega}$ is widely used to report the angular frequency of the wave that will be measured if the observer is in a frame moving with the

horizontal background wind velocity ($\bar{u}$, $\bar{v}$) i.e., $\hat{\omega}$ is wind-referenced:

$$\hat{\omega} = \omega - k\bar{u} - l\bar{v}. \tag{1.1}$$

For medium-to-high frequency GWs, their frequencies are generally much larger than the *Coriolis parameter* f, which depends on the Earth angular rotation rate Ω and latitude ϕ:

$$f = 2\Omega sin\phi. \tag{1.2}$$

Buoyancy force, one of the restoring forces for GWs, results from the vertical pressure or density gradient and lifts the air parcels upward. On the contrary, gravity acts as the other restoring force that leads to the vertical oscillation with a frequency given by the *Brunt-Väisälä frequency*, or the *buoyancy frequency* N:

$$N = \sqrt{g\frac{\partial ln\theta}{\partial z}}. \tag{1.3}$$

Here g is the acceleration due to gravity and z represents the altitude. The other parameter is the *potential temperature* θ, which is the temperature that an unsaturated air parcel would have if it were brought adiabatically[1] to a standard pressure p_0 (typically 100kPa) from its original pressure level p of temperature T:

$$\theta = T\left(\frac{p_0}{p}\right)^{\kappa}, \tag{1.4}$$

where κ is the *Poisson constant* which usually takes the value κ = 0.2854 for dry air (Goody, 1972).

Gravity waves can propagate both horizontally and vertically depending on their spectral properties. According to Fritts and Alexander (2003), the vertically propagating GWs of our interest have real wavenumber components (k, l, m) and an intrinsic frequency confined

[1] The adiabatic lifting refers to the process without heat exchange with the surroundings.

to the range of $N > \hat{\omega} > |f|$. These spectral properties, including the vertical wavenumber and the intrinsic frequency, are modulated by the background atmospheric conditions and vary significantly during the vertical propagation of the GWs (ibid., 2003).

GWs are considered to play an important role in the atmospheric circulation by determining the structure of the wind and the temperature (Shi et al., 2021). In addition, GWs transfer their energy to the background atmosphere when they dissipate or break, which significantly affect the thermodynamics in the middle and upper atmosphere (Alexander & Holton, 2004; Xu et al., 2019).

1.2 Convection and hurricanes

Convection is a major source of gravity wave generation. *Convection* refers to the process that transfers heat through the movement of a mass within a fluid, such as a gas or a liquid (Hewitt & Jackson, 2003). For example, within the Earth's atmosphere, the air parcels near the surface are radiatively heated and tend to rise and mix with the cold air parcels above, a process known as *free convection*. In addition, large-scale surface winds can also force the heated air parcels to rise and mix with the whole air mass, known as *forced convection*.

Convection can also be categorized as shallow convection and deep convection. *Deep convection*, or *deep moist convection* refers to the type of convection that extends from the surface to the level above the tropopause (Davison, 1999). More specifically, deep convection describes a process that an unsaturated air parcel rises above its *level of free convection*[2], which becomes saturated and remains positively buoyant, allowing itself to ascend further upward (Goody, 1972; Markowski & Richardson, 2010).

[2] Level of free convection refers to the altitude at which the saturated air parcel becomes warmer than the surroundings.

There are many weather systems related to convection, for example, a *tropical cyclone* is a fast-developing system closely associated with deep convection. Tropical cyclones are referred to as *hurricanes* over the Atlantic Ocean and are called *Typhoons* when they occur in the western Pacific region. In this thesis, we focus on the tropical cyclones that occur over the Atlantic Ocean and thus we will use the term '*hurricane*'.

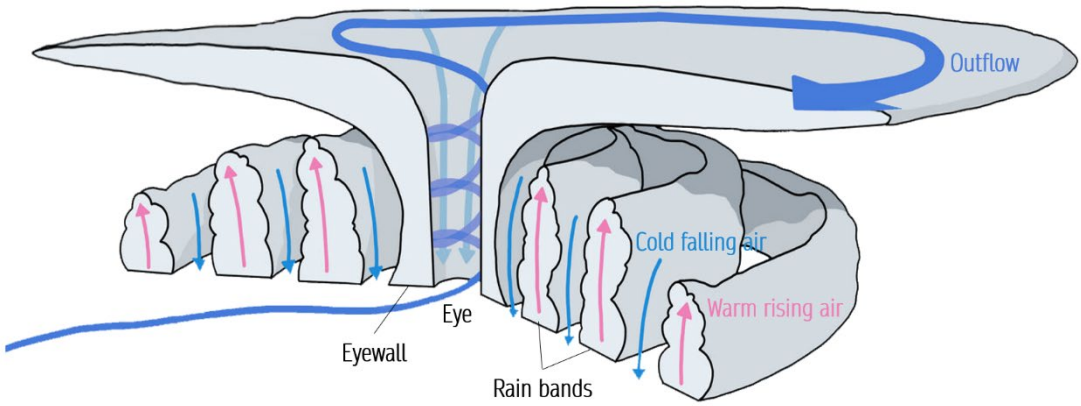

Figure 1.2. A vertical cross section of the internal structure of a hurricane. The calm and clear core of the hurricane is the eye, which is surrounded by the most convective region called the eyewall. Further from the eye, the warm rising air produces precipitation in the spiral rainbands.

Hurricanes are associated with a low-pressure warm core and strong low-level (low-altitude) winds that extend spirally away from the hurricane center (Hewitt & Jackson, 2003). The center of a tropical cyclone is a calm and clear area called *eye*, as shown in Fig. 1.2. The *eyewall* is the thin region surrounding the eye with ring bands of deep convective clouds that extends vertically upward from the ocean surface and occasionally reaches the tropopause.

In the Northern Hemisphere, the surface winds of a hurricane rotate in the counter-clockwise direction while the upper-level winds rotate clockwise. To be specific, the spinning air at the surface rises to the convective clouds due to the surface wind convergence, which forms the eyewall and circulates outward from the cloud top as an outflow around the tropopause height (cf., Fig. 1.2). The thermal rising of the air parcels

and the surface air turbulences cause heavy precipitation in the eyewall and in the surrounding spiral rainbands. In this thesis, we will refer to the outer region of a tropical cyclone with the spiral rainbands as the *rainband region* to distinguish it from the eyewall region.

The formation of the hurricanes requires a warm ocean surface with a *sea surface temperature* (SST) not below 26-27°C as the energy source, which produces warm and moist air mass that upwells to form the convective clouds (Emanuel, 1986; Tory & Dare, 2015). In order to attain the strength of a tropical storm, the outflow temperature[3] needs to achieve a value of -20°C or lower when the SST is less than 26°C (Emanuel, 1986).

As the air parcels ascend from the warm ocean surface in the hurricane region with a decreasing temperature, the condensation of the water vapour releases a large amount of heat, namely the latent heat. *Latent heat* is defined as the heat that is absorbed or released during the phase change of a substance (Smith & Montgomery, 2016). In the event of a hurricane, the release of the latent heat at the ocean surface helps to maintain the atmospheric instability, which generates precipitation and clouds that indicates the beginning of convection (Goody, 1972; Vergados et al., 2013).

Specifically, during a hurricane, the strong latent heat flux near the ocean surface is supplied by the entrainment of the water vapour through the boundary layer convergence, where the intense inflow in the boundary layer acquires moisture from the sea and provides it to fuel the convection (Smith & Montgomery, 2016; Yano, 2021). Hence, the boundary layer is essential in the hurricane genesis since it saturates and destabilises the lower atmosphere (Noh et al., 2003; Nolan, 2007).

[3] Outflow temperature is the air temperature along the constant angular momentum surface as the air spreads to large radii.

The *boundary layer* is usually referred to as the *atmospheric boundary layer* (ABL) or the *planetary boundary layer* (PBL). This layer is the bottom portion of the atmosphere that is in direct contact with the Earth's surface, which usually has a thickness of a few kilometers. The ABL is significantly affected by the surface heating due to the solar radiation and the vertical wind shear (Markowski, & Richardson, 2010).

When positive buoyancy exists at the surface and creates thermal instabilities, the boundary layer becomes a *convective boundary layer* (CBL). In the event of strong solar heating or strong latent heat released, the CBL may comprise the entire troposphere and extends to the height of tropopause (Stull, 1988). Under such circumstances, the deep moist convection is closely associated to continuously deepen the well-mixed boundary layer and the thickness of the CBL becomes 10-15km (Yano, 2021).

According to above, hurricanes are complicated weather systems that cause significant loss to mankind. Costal countries usually experience the most extensive damage from the hurricanes, including heavy rains, flooding, storm surge and even tornadoes (Emanuel et al., 2006). Therefore, a thorough study of the thermodynamic characteristics of the hurricanes including the temperature, water vapour and the rotational winds as well as their couplings with the lower atmosphere are necessary. This knowledge helps to improve the current cyclogenesis modeling and the hurricane intensity forecasting (Emanuel et al., 2006; Tory et al., 2006; Davis, 2018).

1.3 Overview and scope of the thesis

GWs are essential in coupling the Earth's troposphere with the middle to upper atmosphere (Xu et al., 2019). Recent studies suggested that the deep convective systems, such as the hurricanes can generate the upward-propagating, small-scale gravity waves

that potentially change the dynamics in the atmosphere via the momentum flux deposition (Kuester et al., 2008; Zhao et al., 2020).

For example, Huang and Kuo (1978) showed that the spiral bands of a hurricane propagate outward and grow with the presence of the horizontal shear, which behave like the gravity waves. Similarly, Wu et al. (2022) also presented that the hurricane-induced GWs in the stratosphere propagate spirally upward and spread away from the hurricane center using numerical simulations.

Previous studies have shown that the hurricanes can generate concentric gravity waves in the lower to middle atmosphere based on both satellite measurements and model simulations, which sometimes propagate into the upper atmosphere and create the traveling ionospheric disturbances[4] (Xu et al., 2019; Zhao et al., 2020).

However, given the fast-developing nature of the GWs and their convective sources such as hurricanes, the propagation and the variation of the GWs are hard to analyze due to the lack of high-resolution measurements. This shortcoming also poses difficulties in identifying the connection between the GWs and the lower atmosphere.

Hence, we aim to better understand the couplings between hurricanes and the *upper troposphere-lower stratosphere* (UTLS) region through the small-scale CGWs. In this thesis, we use the high vertical resolution measurements from the Global Positioning System – Radio Occultation (GPS-RO), in order to capture the small-scale GWs in the UTLS region that are induced by different hurricanes. We intend to learn more about the spectral properties of the hurricane-induced GWs and their variations with respect to the hurricane intensity.

[4] The traveling ionospheric disturbances are the ionospheric electron density perturbations that propagate as waves.

This study is essential in understanding the coupling between the GWs and the lower atmosphere. We aim to bridge the current knowledge gap of the CGWs by identifying the variability of the GWs during the intensity change of a hurricane. This knowledge will significantly help the small-scale GW parametrization in the global circulation models and leads to a detailed understanding of the energy exchange in the UTLS region (Choi et al., 2012; Xu et al., 2019).

An overview of the thesis is as follows. Chapter 2 introduces the current understanding for the hurricane-induced GWs. This chapter begins with a summary of the mechanisms that generate the GWs through convection. We then introduce the GW dispersion relation and describe the GW modification caused by the background wind filtering effect. We finish this chapter by reviewing the previous research results as well as introducing our research objectives.

Chapter 3 presents the methodology that we follow to analyze the GW characteristics. The GPS-RO technique and its data retrieval process are firstly introduced. We then present the extraction of the wave-induced temperature perturbations using the high vertical resolution RO measurements (Foelsche et al., 2008), as well as the extraction of the wave-induced wind perturbations using the fine horizontal resolution ECMWF dataset (Aragão, & Porcù, 2022). Lastly, we describe the spectral analysis methods that we apply for the temperature perturbations following a least squares approach (Pagiatakis, 1999).

In Chapters 4 to 7, we conduct individual hurricane case studies of four hurricanes with different intensities. For each hurricane, we first discuss the eyewall thermodynamics based on the analysis of the temperature perturbations. The GW characteristics are then introduced according to the spectral analysis results. Lastly, a wind perturbation analysis is shown to describe the GW propagation at different altitude levels.

In Chapter 8, we carry out a comparison of the hurricane thermodynamics as well as the GW behaviours for different hurricanes and in different regions of a hurricane. This chapter focuses on the temperature variations and the GW spectral properties when convection strength varies. Chapter 9 presents a similar comparison of the GW variability for all hurricanes but prioritized on investigating the GW variation with respect to the wave generation or dissipation mechanisms.

Lastly, we provide a summary of the main research outcomes and their significance in Chapter 10. The future direction of the relevant research is then discussed, in order to study the hurricane-induced GWs to a greater extent.

Chapter 2

Gravity Wave Generation and Dissipation Mechanisms

Previous studies have described several mechanisms that can generate the GWs through convection, including the pure thermal forcing, the obstacle effect, the mechanical oscillator effect and the overshooting convection (Stull, 1976; Fritts & Alexander, 2003; Kuester et al., 2008; Dutta et al., 2009), which we will introduce in detail in this chapter.

In addition to the generation of the CGWs, we also discuss the wave dissipation caused by the wind filtering effect in accordance with the GW dispersion relation (Cowling et al., 1971; Fritts & Alexander, 2003). We finish this chapter by reviewing previous studies of the hurricane-induced GWs and their limitations, from which we hope to contribute filling the knowledge gap of the current research.

Although the generation and the modification of the GWs are well studied theoretically, the parametrization of the convective generation is still incomplete due to the variability of the thermal forcing within the convection. In reality, different mechanisms may be coupled nonlinearly within one convective event, but one mechanism may dominate to explain the observations of a certain type of waves (Fritts & Alexander, 2003; Kuester et al., 2008).

2.1 Gravity wave generation

There have been many studies aiming at simulating the mechanisms of the GW generation via convection. Three main mechanisms are now widely accepted and referred to for studying the convectively generated gravity waves.

The first wave generation mechanism is the *pure thermal forcing mechanism*. This mechanism is also known as *deep heating mechanism* (Beres et al., 2002), suggesting that the GWs are generated by a thermal forcing inside the convective storms, such as the release of latent heat (Kuester et al., 2008). The thermal forcing is usually time-dependent and is bounded by heating depth[5]. According to Alexander et al. (1995), the vertical wavelength of the thermal forcing generated waves is about twice the heating depth in the troposphere, which becomes approximately equal to the heating depth in the stratosphere. Since the buoyancy frequency N doubles across the tropopause, as a result the vertical wavelength reduces by half (Fritts & Alexander, 2003).

The second mechanism is the *obstacle effect*. This mechanism is similar to the topographic wave generation, since the convective source in the boundary layer acts as an obstacle to the background flow (wind), just like the wind blowing over the mountain which excites the mountain waves (Kuettner et al., 1987). The GWs excited by the obstacle effect are primarily opposite to the background wind, with short horizontal wavelength but much larger amplitude compared to the GWs that are generated by the pure thermal forcing mechanism (Clark et al., 1986; Dutta et al., 2009). Besides, the obstacle effect also contributes to explaining the large-scale wave generation in the middle atmosphere[6] (Fritts & Alexander, 2003).

[5] Heating depth refers to the depth of the diabatic heating layer.

[6] Middle atmosphere usually indicates the stratosphere and the mesosphere.

Gravity waves can also be generated through the *mechanical oscillator mechanism*. This mechanism assumes that when the air parcel oscillates about its level of neutral buoyancy with a local buoyancy frequency, the GWs can be generated (Fovell et al., 1992). A time-varying thermal forcing is also considered as a nonlinear oscillator if it oscillates with a fixed period (Fritts & Alexander, 2003). The mechanical oscillator mechanism only generates high-frequency waves in the upper troposphere, since the GW frequency equals the oscillating frequency of the source that is, the local buoyancy frequency (Kuester et al., 2008; Dutta et al., 2009).

These conceptual models have well described the possible generation mechanisms of the CGWs. However, to the best of our knowledge, these assumptions have not been verified by the pervious studies using either numerical simulations or observational results. Our work is innovative in that for the first time, we link and illustrate the conceptual wave-generation models with the observational evidence using temperature measurements (vertical profiles) from GPS-RO and wavelet analysis results, shown in Chapters 4 to 9.

In addition to the three wave-generating mechanisms introduced above, Stull (1976) also proposed a mechanism that can excite GWs through the overshooting convection, which is also known as the *penetrative convection*. When the ABL is capped by a temperature inversion, the air parcels ascend from the turbulent layer[7] usually stop at the equilibrium level. However, if the air parcels ascend fast enough due to the strong instabilities, they are able to shoot upward from the turbulent mixed layer and enter the overlying stable layer due to the large momentum they carry. This process is called the *overshooting convection*, from which both the horizontally propagating and the vertically propagating GWs are excited (Stull, 1976). In the case of deep moist convection, where the CBL

[7] Turbulent layer contains many eddies that tend to cause mixing and dispersion of the air mass.

extends to the height of the tropopause, the overshooting convection exists if the temperature inversion caps the tropopause.

Correspondingly, Vergados et al. (2014) suggested that the vertical updrafts inside the hurricane eyewall possibly led to overshooting convection at stratospheric altitudes. In this thesis, we are able to verify this assumption using temperature perturbation profiles inside the eyewall region of intense hurricanes. Moreover, we further provide analytical results to confirm the generation of the small-scale GWs via the overshooting convection.

According to Stull (1976), overshooting convection generates GWs that propagate horizontally at the base of the temperature inversions, which are called the *interfacial waves* since they are generated along the interface between the turbulent layer and the overlying stable layer. Overshooting convection also generates the vertically propagating GWs in the stable layer above the capping inversion, which are the internal gravity waves of interest to us. When the vertically propagating GWs are generated, energy carried by the GWs is lost in the turbulent layer during the upward propagation; the loss is small if a strong temperature inversion is present. When the turbulent layer is vigorous and the inversion is weak, the loss of the GW energy is significant (Stull, 1976).

In mechanisms that can generate GWs via convection, the convective source is usually time-dependent and/or unstable. Following Alexander and Holton (2004), we refer to the short-duration or the time-varying thermal forcing as a *transient heat source*. The transient heat source is known to produce GWs through the nonlinear heat flux divergence and the release of latent heat, which leads to two types of wave packets that are distinct from each other with different characteristics (Alexander & Holton, 2004):

(1) The transient heat source can excite the GWs with high frequency and long vertical wavelength. This type of GWs propagate fast vertically, which are also known as the

primary waves or *deep waves* (Nolan, 2020). These primary waves quickly propagate upward, which can only be observed for a short period of time in the stratosphere at a close radial distance from the heat source (Alexander & Holton, 2004).

(2) The transient heat source can also excite the GWs with low frequency and short vertical wavelength, which are known as the *secondary waves* (Nolan, 2020). These secondary waves propagate slowly in the vertical direction and stay longer in the lower atmosphere, which can be observed for a long period of time at a longer distance from the heat source (Alexander & Holton, 2004).

However, the primary waves are usually trapped in the troposphere by the turbulent layer due to the convection in the upper troposphere and the temporal variation of the momentum flux. Thus, the secondary waves dominate in the stratosphere and are more likely to be observed (Alexander & Holton, 2004; Dutta et al., 2009).

Our work agrees notably well with the assumption brought up by Alexander and Holton (2004). We justify the trapping of the primary waves at low altitudes and the domination of the secondary waves in the stratosphere based on the analysis of wind perturbations. More importantly, we closely relate the concepts of two distinct wave packets generated by the transient heat source with a two-layer convection model to inventively describe the convection regime of intense hurricanes as we present in Chapter 9.

2.2 Gravity wave dispersion relation

In physics, a wave is associated with an angular frequency ω and a wavelength λ. It is also useful to describe the propagation of a wave using linear wavenumber, which measures the cycles that a wave completes per unit distance. The *angular wavenumber*, or simply *wavenumber*, is more commonly used nowadays.

In a local reference frame that captures the GWs with origin located at the source of the wave, z-axis points vertically upward to the opposite direction of the gravity vector, x-axis points toward east and y-axis forms a right-handed Cartesian coordinate system. For a wave perturbation with angular wavenumber components (k, l, m) in this local reference frame, the horizontal or the vertical wavelength of the wave is defined as the horizontal or the vertical distance between the line of constant phase. Fig. 2.1 below illustrates the determination of the wavelength using the constant phase line in the $x - z$ plane.

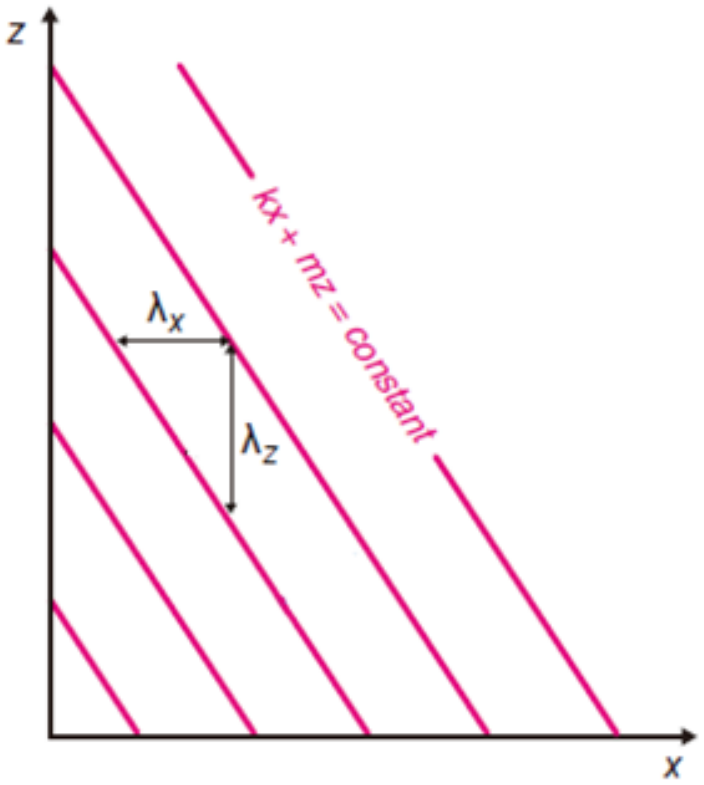

Figure 2.1. Determination of the horizontal and vertical wavelength. Lines indicate the constant phase for the wave, λ_x and λ_z are the wavelengths in the x and z directions vector (Markowski, & Richardson, 2010).

For simplicity, we define a horizontal wavenumber k_h to report the horizontal propagation of a wave in the $x - y$ plane:

$$|k_h| = \sqrt{k^2 + l^2}\,. \tag{2.1}$$

Hence, the horizontal wavelength λ_h can be linked to the horizontal wavenumber via:

$$\lambda_h = \frac{2\pi}{k_h} . \tag{2.2}$$

Similarly, the vertical wavelength λ_z of the wave is expressed as:

$$\lambda_z = \frac{2\pi}{m} . \tag{2.3}$$

Aside from the wavelength, another important parameter to describe the GWs is the intrinsic frequency $\hat{\omega}$. The intrinsic frequency of a GW is related to its angular frequency ω via Eq. (1.1), where $\hat{\omega}$ is defined as the frequency that will be measured in a frame moving with the horizontal background wind ($\bar{u}$, $\bar{v}$) (Fritts & Alexander, 2003).

When GWs exist in an environment with ambient wind, the intrinsic frequency of the GWs experiences a Doppler shift along the wind direction (Markowski, & Richardson, 2010). To highlight the Doppler shift effect, let $\bar{u}_h$ denote the horizontal background wind as:

$$|\bar{u}_h| = \sqrt{\bar{u}^2 + \bar{v}^2} , \tag{2.4}$$

then Eq. (1.1) can be written using the horizontal wavenumber k_h as:

$$\hat{\omega} = \omega - k_h \cdot \bar{u}_h . \tag{2.5}$$

As Eq. (2.5) states, the increase or decrease of the GW intrinsic frequency depends on the GW propagation with respect to the horizontal background wind direction, a wave-dissipating mechanism called the *background wind filtering* that we will introduce in the next section. Alternatively, the variation of the GW intrinsic frequency in turn causes a change in the GW wavenumber, which is stated by the *GW dispersion relation*.

When a wave packet is composed of waves with different wavelengths or frequencies, these waves may travel at different speeds. This phenomenon is known as the *wave*

dispersion. Specifically, the wave packet or wave envelope that is made up of different wavelength (frequency) components travels at a velocity called *group velocity* c_g, while each wavelength (frequency) component travels at its *phase speed* c (Fritts & Alexander, 2003).

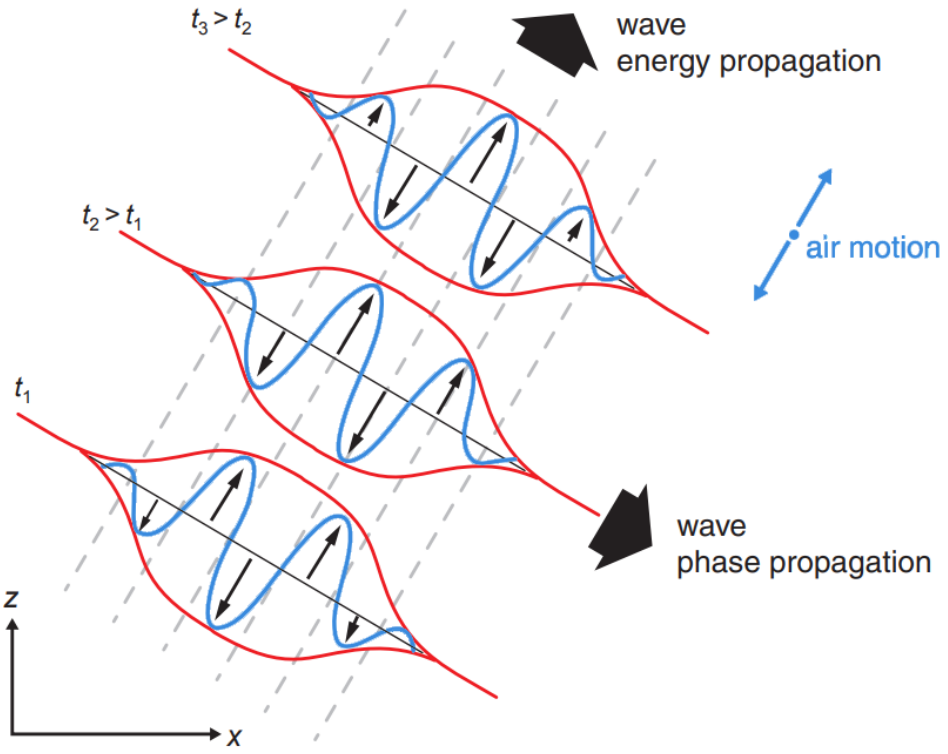

Figure 2.2. Energy propagation and phase propagation for an internal gravity wave (Markowski, & Richardson, 2010).

According to Fritts and Alexander (2003), the phase speed of the GWs is a scalar quantity, although the phase propagation follows the direction of wavenumber vector (k, l, m). This leads to an important property of the GWs that they have upward group velocity (energy propagation) but the GW phase propagates downward (Steiner & Kirchengast, 1999). As shown by Fig. 2.2, for eastward and upward energy propagation, the phase propagates eastward ($k > 0$) and downward ($m < 0$), which is perpendicular to the direction of group velocity.

Gravity waves are transverse waves that undergo dispersion, since they propagate perpendicular to the air parcel displacements (cf., Fig. 2.2). For dispersive waves such as the GWs, the dispersion relation connects the frequency of a wave component with its spectral characteristics as well as with the properties of the background atmosphere and a scale height H via:

$$\widehat{\omega}^2 = \frac{N^2(k^2 + l^2) + f^2\left(m^2 + \frac{1}{4H^2}\right)}{k^2 + l^2 + m^2 + \frac{1}{4H^2}}\ , \tag{2.6}$$

where H describes the vertical distance over which the pressure of the atmosphere drops by a factor of e (Here e is a numerical constant, namely the Euler's Number, which has a value of about 2.718). Following Fritts and Alexander (2003), simplifications of the dispersion relation can be made for different frequency bands of the GWs:

(1) For GWs in a high-frequency band $\widehat{\omega} \gg f$, the Coriolis effect can be ignored and the GW dispersion relation is simplified to:

$$\widehat{\omega}^2 = \frac{N^2 {k_h}^2}{{k_h}^2 + m^2}\ . \tag{2.7}$$

The high frequency waves have long vertical wavelength but relatively short horizontal wavelength, which are easy to be trapped in the lower atmosphere. The vertical wavelength of these high frequency waves strongly depends on the variation of the atmospheric density.

(2) Medium-frequency waves are defined with an intrinsic frequency of $N \gg \widehat{\omega} \gg f$. Such GWs have a simplified form of the dispersion relation:

$$\widehat{\omega}^2 = \frac{N^2 {k_h}^2}{m^2}\ . \tag{2.8}$$

In this frequency band, the effects of the background wind become significant in modifying the wave properties. Because the background wind directly affects the intrinsic frequency of the GWs, the intrinsic frequency is closely related to the vertical wavenumber (wavelength) of the GWs as stated by Eq. (2.8).

Although this simplified form is too general to describe the atmosphere under some extreme weather phenomena, it still brings many insights into studying the gravity wave properties with respect to the variations in the atmosphere (Fritts and Alexander, 2003).

(3) When the rotation of Earth cannot be neglected, the intrinsic frequency of the GWs is at a scale close to the Coriolis parameter since $\hat{\omega} \sim f$. The GWs are therefore low-frequency waves. An approximation of the dispersion relation becomes:

$$\hat{\omega}^2 = \frac{N^2 {k_h}^2}{m^2} + f^2. \tag{2.9}$$

This approximation is valid for the low-to-medium frequency waves, because f can be ignored when the Coriolis effect does not play a significant role (Fritts & Alexander, 2003).

For all frequency bands, the GW dispersion relation reveals that the vertical wavenumber m is inversely proportional to the intrinsic frequency $\hat{\omega}$. This relation indicates a positive correlation between the vertical wavelength λ_z and the intrinsic frequency $\hat{\omega}$ of the GWs. Due to the fast-developing nature of the ambient wind and the convective sources, the GW intrinsic frequency varies significantly with respect to the environmental stability and the background stratification (Fritts & Alexander, 2003). Hence, the GW propagation described by the wavenumber (wavelength) also changes accordingly following the GW dispersion relation.

Unfortunately, the GW dispersion introduces difficulties in distinguishing different wavelength/ frequency components in the spectral analysis, especially the GW vertical wavelength varies with respect to the changing intrinsic frequency during the GW propagation (Steiner & Kirchengast, 1999). Our work attempts to resolve this obstacle by identifying various wavelength components and visually presenting the GW wavelength variation, taking the advantages of the wavelet analysis method that we apply.

2.3 Wind filtering effect

Let us recall Eq. (2.5), which describes the variation of the GW intrinsic frequency with respect to the background wind direction. To be specific, the variation of the GW intrinsic frequency depends on the dot product $k_h \cdot \bar{u}_h$. When the GWs propagate in a similar horizontal direction as the background wind, i.e., when $k_h \cdot \bar{u}_h$ is positive, the GW intrinsic frequency decreases. When the GWs propagate in an opposite horizontal direction to the background wind, i.e., when $k_h \cdot \bar{u}_h$ is negative, the GW intrinsic frequency increases.

According to the GW dispersion relation, the variation in the intrinsic frequency also leads to a corresponding change in the GW vertical wavelength as they are positively correlated that is, when the GWs propagate along with the horizontal background wind, the vertical wavelength is shifted towards a shorter value due to the decreasing intrinsic frequency. In contrast, when the GWs propagate opposite to the horizontal background wind, the GWs are refracted to a longer vertical wavelength with an increasing intrinsic frequency (Cowling et al., 1971).

Such modifications in both frequency and wavelength are described as the *background wind filtering*, which is important for studying the weather systems with strong winds (Mukherjee et al., 2010). Background wind filtering is known to play a key role in filtering

the GW spectrum that is generated by hurricanes and typhoons (Kim et al., 2009). For instance, the GWs generated via the pure thermal forcing mechanism are expected to reveal an isotropic wave field[8], but an anisotropic field will be observed with an asymmetric GW propagation if the background wind filtering is present (Fritts & Alexander, 2003).

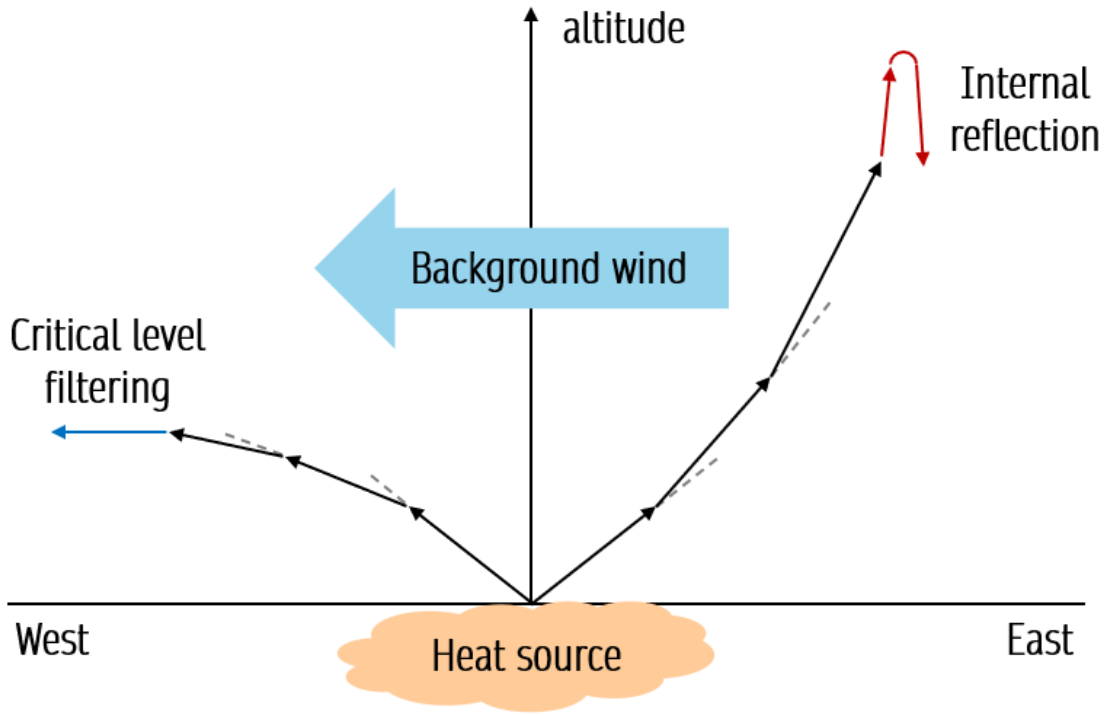

Figure 2.3. Effects of the background wind filtering on gravity waves. Eastward and westward propagating waves are simulated (black arrows) with varying vertical wavelength (varying arrow length).

Moreover, background wind filtering is a wave dissipation mechanism after reaching certain thresholds (Majdzadeh, 2017). As the vertical GW wavelength increases or decreases, critical wavelength values might be reached as extreme cases of the wind filtering effect, shown in Fig. 2.3. Assume that a heat source generates the GWs that propagate both horizontally and vertically with a vertical wavelength λ_z, where the horizontal background wind blows due west over this region.

[8] Isotropic wave field indicates that the propagation of the GWs is relatively symmetric in different directions.

When the GWs propagate eastward that is, against the horizontal background wind, the GW vertical wavelength increases as the GWs propagate upward (cf., Fig. 2.3; arrow length increases). An extreme case may occur when the vertical wavelength λ_z grows very large and the vertical wavenumber m becomes close to zero. Under such circumstances, the high-frequency (long-vertical wavelength) waves may experience a process called *internal reflection* (Sutherland, 1999).

Theoretically, internal reflection occurs at the *turning level* for the GWs, where the vertical group velocity changes sign (Fritts & Alexander, 2003). The GWs vanish above the level of internal reflection where λ_z grows to infinity, which sometimes results in the trapping of the high-frequency waves at lower altitudes.

When the GWs propagate westward, as in the assumption above that is, they propagate in the direction of the background wind, the GW vertical wavelength decreases (cf., Fig. 2.3; arrow length deceases). This may lead to another extreme case when the vertical wavelength λ_z shrinks to zero and wavenumber m goes to infinity, which is known as *critical level filtering*. The critical level filtering is widely observed for the hurricane-induced GWs using the numerical simulations, when the simulated GWs propagate in the same direction as the background wind (Kim & Chun, 2010; Choi et al., 2012; Xu et al., 2019).

For medium-frequency waves, the c*ritical level* is defined as the altitude at which the *intrinsic phase speed* of the GWs becomes zero. With the presence of the background wind, the (horizontal) intrinsic phase speed $\hat{c}_h$ is defined similar to the intrinsic frequency $\hat{\omega}$ and reads:

$$\hat{c}_h = c_h - |\bar{u}_{hs}|\,, \tag{2.10}$$

where c_h is the horizontal phase speed of the GWs and $\bar{u}_{hs}$ represents the horizontal wind in the direction of the GW propagation.

In other words, the GWs reach the critical level when $c_h = |\bar{u}_{hs}|$ is satisfied, or equivalently, when they propagate slower than the background wind in the horizontal direction. However, this is slightly different from the *true critical level* for the low-frequency waves, where the intrinsic frequency $\hat{\omega}$ approaches f as the vertical wavelength λ_z approaches zero, according to Eq. (2.9).

Similar to the level of internal reflection, the critical level for the GWs is also a theoretical limit that cannot be reached in reality. Nevertheless, the variation of the GW properties is very useful to describe the GW behaviours when they approach the theoretical threshold. Once the critical level is approached, the GWs get trapped at that height and cannot propagate further upward, eventually the GWs dissipate and deposit their energy to the background flow (Taylor et al., 1993; Sutherland, 1999; Xu et al., 2019).

The modifications of the GWs caused by the horizontal wind were frequently observed in recent studies (Kim et al., 2009; Kim & Chun, 2010; Wang et al., 2021). Background wind filtering is widely applied to explain the differences between the upper-level and the low-level GW propagation without actual proof of the GW varying process. Our work is at the forefront of the research in this area in that we explore the variation of the GW propagation and illustrate the shift of the GW vertical wavelength, verifying the wind-filtering theory as we will see in Chapter 4 onwards.

2.4 Previous work and motivation

Gravity waves (GWs) have been considered as one of the most important dynamic processes that transfer energy and momentum from the lower to upper atmosphere (Eichinger et al., 2020). Among all the GWs, the small-scale GWs specifically drive the momentum exchange in the UTLS region (Wright & Banyard, 2020). Some small-

amplitude GWs can even propagate into the mesosphere and the thermosphere, where they deposit their energy into the background atmosphere through the wave breaking or damping (Xu et al., 2019).

The deep convection and the overshooting convection are known to generate small-scale GWs in the eyewall region and in the rainbands of the hurricanes (Kim et al., 2009; Kim & Chun, 2010; Müller et al., 2018). These CGWs propagate radially outward, or equivalently, spirally upward from the convective source that further produce the subsidence[9] and warming in the surrounding environment (Lane & Reeder, 2000; Wu et al., 2022).

Many studies have aimed to acquire additional knowledge on the CGW structure and their propagation patterns. Steiner and Kirchengast (1999) showed that the small to medium scale GWs excited by the convective phenomena typically have a horizontal wavelength of 100-1000 km, a vertical wavelength of about 1-10 km and a time period of 10 minutes to an hour. The scales of the CGWs are relatively consistent in recent studies with some small disparities that are possibly due to the diverse measuring techniques and the dissimilar modelling resolution (Kim et al., 2005).

Dutta et al. (2009) suggested that the CGWs are generated via both diabatic forcing and nonlinear forcing through a complicated mechanism. Hence, the effects of the thermal forcing on the GW structure have become of great scientific interest (Nicholls et al., 2018). Beres et al. (2004) concluded that the GW amplitudes were overestimated in the previous studies by only assuming the presence of the diabatic forcing. As an improvement, they proposed a method to accurately specify the GW spectra, based on the knowledge of the latent heat distribution as well as the low-level wind profile (ibid, 2004).

[9] Subsidence is the downward motion of an air parcel as it cools and becomes denser.

In addition, the asymmetric distribution of the thermal forcing that localizes the convection is also shown to affect the GW structure (Gettelman et al., 2002; DeHart et al., 2014). Rogers et al. (2016) found that the azimuthal and radial distribution of the deep convection primarily dictate whether a hurricane would intensify, using Hurricane Edouard (2014) as a showcase. The intensification of a hurricane in turn affects the associated CGW spectra (Hoffmann et al., 2018; Wu et al., 2022). Likewise, in our analysis of the hurricane-induced GWs, we notice that the radial distribution of the convective forcing plays an essential role in modulating the GW vertical propagation, which will be presented in Chapter 8.

Aside from the thermal forcing, the background wind and the vertical wind shear have profound effects on the vertically propagating GWs as well. The horizontal wind acts as a directional filter to modify the GWs through the background wind filtering, or as an attenuation filter to dissipate the GWs through the critical level filtering (Taylor et al., 1993; Mukherjee et al., 2010). Alternatively, the vertical wind shear produces asymmetries in the vertical background flow that also modify the GW spectra (Beres et al., 2002; DeHart et al., 2014). More discussion of the wind-filtering effects is delivered through the hurricane case studies which we will see in the following chapters.

The energy density is another important parameter to study the GWs, since the GWs lose their momentum and energy when they break in the upper atmosphere where the air is rarefied (Song & Chun, 2004). Zhao et al. (2022) carried out a numerical study of the GW potential energy density vertical distribution using Lidar measurements, from which they recommended that the GWs dissipate notably in the lower mesosphere but exhibit conservative growth in the upper mesosphere. In fact, we also observe an energy loss during the GW upward propagation (cf., Chapter 8), although we are not able to verify whether the loss of energy is due to the breaking or dissipation of waves.

As discussed above, recent studies have notably expanded our understanding of the GWs which led to an improvement in the GW parametrization However, there remain areas where further research is required to accurately describe the GW variation and their effects on the atmosphere. For example, the GWs are hard to detect in the observations due to the lack of high vertical resolution temperature and density profiles, not to mention the analysis of the GW variations. Hindley et al. (2015) noticed that the key parameters used to simulate the GWs are poorly constrained, which results in the discrepancies between the various modelled results of the hurricane-induced gravity waves (Chen et al., 2012; Kim et al., 2014; Strelnikova et al., 2021).

Furthermore, the asymmetry in the horizontal and vertical propagation of the GWs with respect to the source of generation is not fully understood (Nolan, 2020; Wu et al., 2022). The coupling between the GWs and their convective sources in the lower atmosphere also remain unclear (Xu et al., 2019). These missing links are key to explain the mutual interaction between the GWs and their convective sources such as the hurricanes.

All the reasons above highlight the need of high spatial resolution measurements for the GW perturbations as well as a deeper understanding of the CGW generation mechanisms. We therefore aim to study the small-scale GWs induced by hurricanes with focus on the behaviours of different wave-generating mechanisms, in order to investigate the coupling between the GWs and the convective environment. We attempt to achieve this goal by analyzing the spectral properties of the hurricane-induced GWs as well as the variations of such properties with respect to the hurricane intensity.

Specifically, we use the high vertical resolution GPS-RO measurements that are essential in resolving the small-scale GWs and their vertical variations in the UTLS region, which cannot be provided by coarse vertical resolution measurements, such as the infrared (IR) and the microwave (MW) sounders (Foelsche et al., 2008).

In this thesis, we succeed to simulate the convective regimes of the hurricanes and their variations with respect to the hurricane intensity. We also seek to connect the hurricane-induced GWs with their corresponding wave generation mechanisms. Hence, our work provides the hypothesis to deduce or predict the hurricane intensity by simply identifying the typical spectral properties for certain GWs.

By understanding the coupling between the hurricanes and their associated GWs, we can better interpret the energy and momentum exchange in the UTLS region for strong convective systems (Nolan, 2007; Wright & Banyard, 2020). This knowledge is beneficial for improving the hurricane cyclogenesis models and will significantly help the small-scale GW parametrization in the global circulation models (Choi et al., 2012; Xu et al., 2019).

Chapter 3

Extraction and Analysis of Wave-induced Perturbations

To study the small-scale vertical variations of the GWs in the atmosphere, we use the temperature retrievals from the Global Positioning System – Radio Occultation (GPS-RO) technique. A detailed introduction of the GPS-RO technique will be given in this chapter as well as its data retrieval process.

The study of the hurricane-induced GWs is carried out through the analysis of the wave-induced perturbations, which are formatted as individual vertical profiles. In this chapter, we present the methodology that we follow to extract the temperature perturbations from the RO temperature retrievals and the wind perturbations from the ERA5 reanalysis dataset. We also discuss the least squares spectral analysis and wavelet analysis methods that we apply on the extracted temperature perturbations to report the important GW characteristics.

3.1 Introduction to GPS - Radio Occultations

The GPS-RO is a space-based observing platform that measures the Earth's limb, using the GPS (and now the GNSS) satellites that emit dual-frequency radio signals (about 1.2 GHz and 1.5 GHz) and the low Earth orbiting satellites (LEO) that capture radio signals during the occultation event (Vergados et al., 2013). As the radio signals travel through the Earth's atmosphere, they bend due to the changing refractivity caused by the changing

atmospheric air density (Healy, 2017). The concept of GPS-RO is illustrated in Fig. 3.1.

However, the GPS receivers onboard LEO satellites do not directly measure the amount of the signal bending. *Phase delays* at two GPS frequencies are the basic measurements of the RO technique (Foelsche et al., 2008). With the recorded phase delays of the receiving radio signals, a term called the *straight-line path delay* is first subtracted. The straight-line path delay is defined as the phase delay that would have been measured with the absence of the Earth's atmosphere, where the radio signals travel with a straight-line path (Healy, 2017). Clearly, the GPS-RO requires the determination of precise orbits for both the GPS and LEO satellites to derive the straight-line distance between the two.

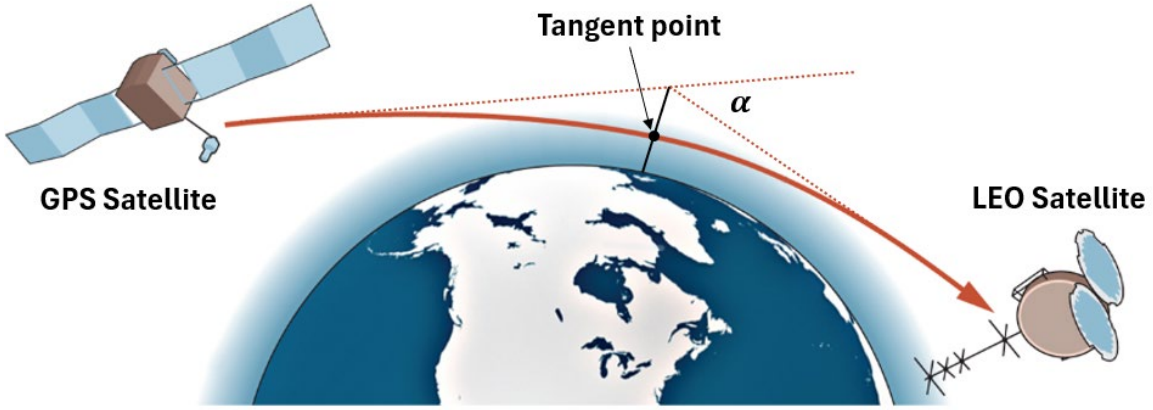

Figure 3.1. Diagram of GPS-RO technique where GPS signals are bent over the horizon (Hand, 2015). Illustrations of the tangent point and the bending angle α are also shown.

After subtracting the straight-line path delay, the remaining term is called the *excess phase delay* (Vergados et al., 2014). The kinematic Doppler effect is then removed with respect to the positions and velocities of the satellites. The frequency-dependent ionospheric effect is also removed using a linear combination of the RO measurements at two GPS frequencies. The leftover phase delay is then considered to be caused by the refractivity in the neutral atmosphere[10] (Foelsche et al., 2008).

[10] Neutral atmosphere refers to the nonionized component of the atmosphere below the ionosphere.

The amount of the radio signal bending, namely the *bending angle* α, can be derived from the leftover phase delay. The bending angle is usually about 1-2 degree(s) near the Earth's surface when the signal path traverses the low atmospheric layers (near the planetary boundary layer), which then falls exponentially as altitude increases (Healy, 2007). In a spherically symmetric atmosphere, the bending angle is related to the refractivity index n via the Abel transform (COSMIC Project Office, 2005). Given the scope of this study, we do not provide more details for the derivation of the refractivity index.

Based on Snell's law of refraction (Chartier, 2005), the refractive index n of the atmosphere is related to the atmospheric pressure p, temperature T and water vapour pressure e (Not to confuse it with the numerical constant e, here e is used to keep consistency with the literature). The refractivity of the atmosphere N_e is given by (Smith & Weintraub, 1953):

$$N_e = (n-1) \cdot 10^6 = 77.6 \frac{p}{T} + 3.73 \cdot 10^5 \frac{e}{T^2} . \quad (3.1)$$

When the water vapour is negligible that is, the '*dry condition*' is assumed and the second term on the right-hand side (RHS) of Eq. (3.1) becomes zero (Foelsche et al., 2008). Under dry condition, the refractive index n is directly proportional to the ratio of pressure and temperature, which is the air density as stated by the ideal gas law (Hewitt & Jackson, 2003). After retrieving the air density, pressure p can be derived through the hydrostatic integration, and temperature T can also be calculated using the ideal gas law (Healy, 2017).

When the water vapour cannot be neglected, for example in the lower troposphere, additional information on the atmospheric humidity is needed to derive the water vapour and the corresponding temperature (Foelsche et al., 2008; Vergados et al., 2014).

In short, as the LEO satellite moves relative to the GPS satellite on the other side of the Earth (cf., Fig. 3.2), a time series of the phase delay is obtained during the occultation event that lasts about 1-2 minute(s), which can be converted to a vertical profile of bending angles (Healy, 2017). Following the retrieval process, high vertical resolution profiles of the thermodynamic variables can be produced.

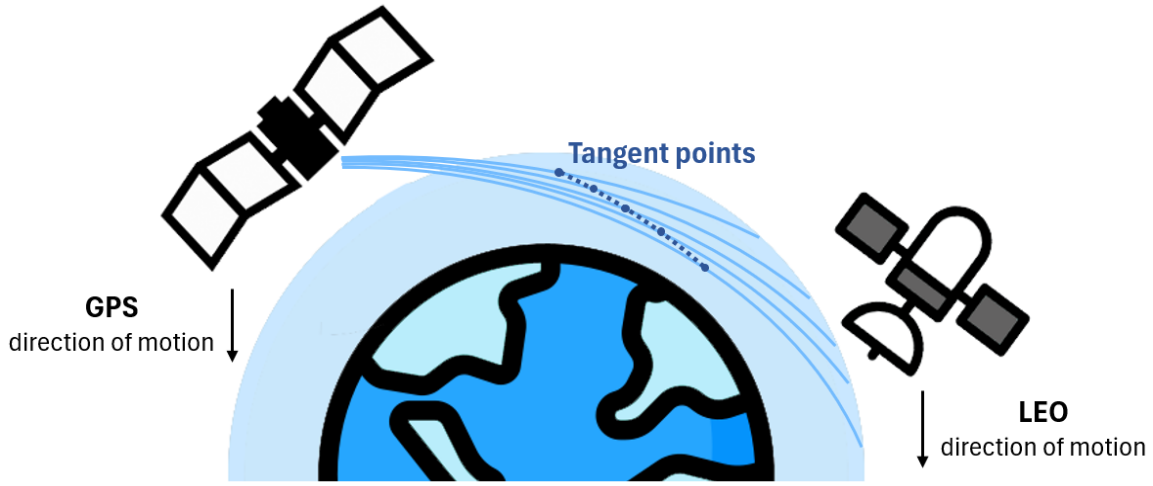

Figure 3.2. Diagram of GPS-RO with tangent points along the signal path (not to scale). The retrieved 'vertical' profile is illustrated with the blue dashed line that connects the tangent points.

As illustrated in Fig. 3.1 and Fig. 3.2, the *tangent (perigee) point* of the GPS-RO defines the closest approach of the signal path to the Earth, which usually drifts about 200km horizontally during an occultation event (Healy, 2007). The information at the tangent point describes the mean state of the atmosphere that is averaged over a horizontal distance along the signal path, with a peak weight at the tangent point (Vergados et al., 2014).

For a retrieved profile of the thermodynamic variables, a reference tangent point location is assigned for the corresponding occultation event, despite the fact that the true tangent points exhibit a horizontally-drifted trajectory. This reference location is referred to as the *mean tangent point* or the *occultation tangent point*, which is defined with respect to the straight-line path between the GPS satellite and the LEO satellite when it is tangent to the

Earth's surface (Innerkofler, 2023). To avoid confusion, we refer to the mean tangent point of an RO profile as the *occultation tangent point*.

The GPS-RO profiles have the advantages of high vertical resolution (<1km), high accuracy of temperature retrieval (<1K), all-weather capability and the global coverage (Steiner & Kirchengast, 1999). The available altitude of the RO profiles is usually below 40km altitude, since the ionospheric effects possibly exceed the phase delays above 40km altitude (Tsuda et al., 2011). The highest quality of the RO temperature retrievals is reported at 8-35 km altitude, with an estimated temperature retrieval accuracy of about 0.2-0.5K (Hajj et al., 2004; Foelsche et al., 2008).

Vergados et al. (2014) utilized the cloud-penetrating (all-weather) capability of the RO technique to estimate the intensity of hurricanes using the temperature retrievals from the GPS-RO. These high-resolution retrievals provide useful thermodynamic parameters in the eyewall region that exhibit the hurricane characteristics. Likewise, Hindley et al. (2015) used the dry temperature retrievals from the RO technique to explain the properties of GWs in a 'hot-spot' region where intense gravity wave momentum fluxes are observed.

Hence, the GPS-RO technique is suitable for monitoring atmospheric changes especially in the UTLS region, which provides a detailed view of the vertical temperature variations in the lower atmosphere (Khaykin et al., 2017). In this thesis, we use the RO temperature retrievals as the primary source for analyzing the hurricane-induced GWs.

3.2 Wave-induced temperature perturbations

In this study, we use the level 2 data from the Constellation Observing System for Meteorology Ionosphere and Climate (COSMIC) mission, which provides the retrieved atmospheric profiles that are derived from the binary instrument data. COSMIC mission

has a distinctive feature that tracks the atmospheric occultations in an open-loop (OL) mode[11], which effectively reduces the RO inversion biases and is valuable for detecting the moisture variations in the lower troposphere (Ao et al., 2009; Kishore et al., 2011).

Specifically, we use the temperature retrievals with moisture information included from COSMIC 1 mission, namely the *wetprf* profiles. These temperature retrievals are formatted with a uniform vertical spacing of 0.1km that are available from the surface to 39.9km altitude. The coordinates of the occultation tangent points for the retrievals are used to locate each individual profile relative to the hurricane eye, while the eye information and the best track of the hurricane's path are provided by the National Hurricane Center (NHC).

Following Ehard et al. (2015), the gravity wave-induced temperature perturbation $T'(z)$ can be obtained by subtracting a background temperature profile $T_0(z)$ from an individual temperature profile $T(z)$ as:

$$T'(z) = T(z) - T_0(z)\,, \tag{3.2}$$

where the temperature profiles are functions of altitude z only. Since RO temperature retrievals are provided in the format of a data series as function of altitude, we do not consider the time-dependent variations of the GWs within the scope of this study.

The *individual temperature profile* $T(z)$ is selected as the temperature retrieval that is located in the eyewall region or in the rainband region of the hurricanes, which exhibits the hurricane-related characteristics in the region of interest. To study the hurricane activities in the eyewall region, $T(z)$ is selected with a radial distance of 25-110km from the hurricane eye, with a time gap of less than 3 hours from the passage of the hurricane (cf., Fig. 3.3). Given an average eyewall diameter of 20-50km, the selected individual

[11] The open-loop tracking is independent of the feedback process where the reference signal is assumed based on the precise knowledge of the satellite orbits and the receiver clock drift.

eyewall profile is considered to fall in the vicinity of the eyewall region and reveals the eyewall characteristics (Vergados et al., 2014).

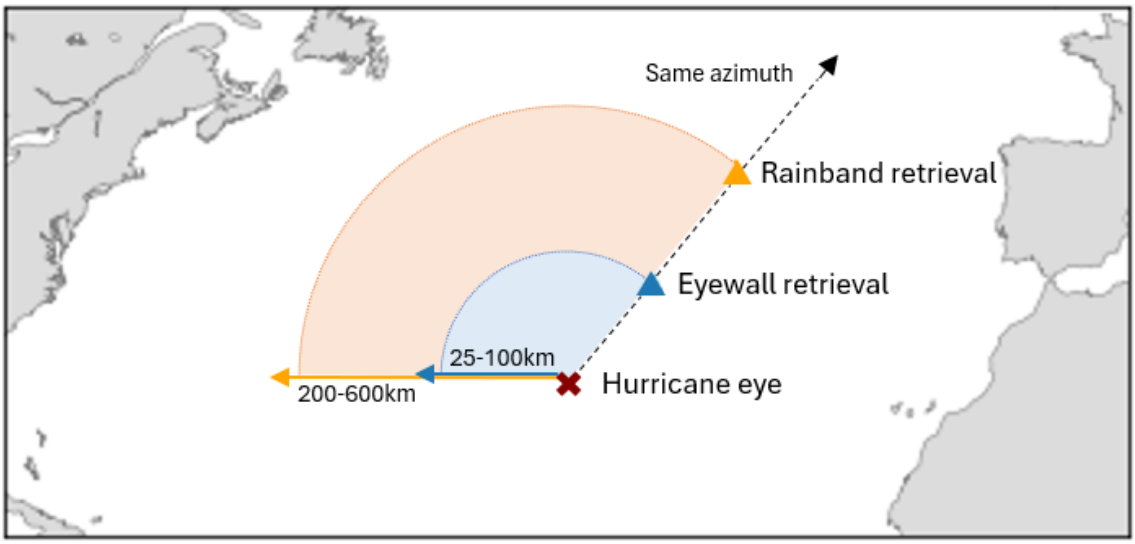

Figure 3.3. Diagram of the temperature retrieval selection[12] for the eyewall (blue triangle) and the rainband region (orange triangle).

For each selected eyewall profile, we also select a *rainband temperature profile* on the same azimuth with a larger radial distance from the eye (200-600km) and the nearest recorded time, as shown in Fig. 3.3. We consider the eyewall and rainband temperature profiles on the same azimuth reflecting the nearly same-time thermodynamic states in the atmosphere, but showing different thermal forcing as the radial distances differ.

The *background temperature profile* $T_0(z)$ in Eq. (3.2) aims to cover any large-scale atmospheric effects, such as the radiative heating and the planetary tides, except for the GWs. After removing the background atmospheric effects $T_0(z)$ from the hurricane related characteristics $T(z)$, the residual perturbation $T'(z)$ is then assumed to be purely induced by the GWs (Ehard et al., 2015). Obviously, the precise determination of the background profile is essential to exclude the GW-induced perturbations to the greatest extent.

[12] This is only an illustration and is not subject to the real horizontal scale or location.

A common way to determine the background profile is by using the moving average of the temperature profiles over a time window (Ehard et al., 2015; Müller et al., 2018). Lu et al. (2015) constructed a monthly mean background profile while Rauthe et al. (2008) used a nightly mean background profile to calculate the altitude-dependent temperature fluctuations. The time window width for computing the moving average should be larger than the timescales of the wave-induced variations. Therefore, the phenomena with timescales larger than the time window would contribute to the background profile through the averaging.

To construct our background temperature profile, we select an undisturbed period before the hurricane occurrence as the time window for averaging, which is about 3-4 days. During the undisturbed period, all temperature retrievals that are located within a 600km radius from the hurricane eye are selected, aiming to cover any local effects of the temperature variations in the atmosphere. The background profile $T_0(z)$ is then obtained by averaging all the selected profiles, which represents the mean state of the undisturbed atmosphere when no hurricane is present.

We have examined a longer time window of about 4-8 days to compute the moving average. We have also considered constructing the background profile through a weighted-mean method, where the weight of each profile inversely correlates with the radial distance from the eye. Nevertheless, we find that by applying either the long averaging window or the weighted-mean method, the background temperature profile remains almost unchanged. The difference in the background profiles that are constructed using different methods is up to 0.1K, which we consider as negligible.

The validity of using 600km as the spatial limit for temperature profile selection has also been tested. According to our analysis, the correlation coefficient between any two vertical

temperature profiles is higher than 0.99 within a distance of 3500km, which reaches a value of 0.995 when the distance becomes less than 600km. We therefore assume that the vertical atmospheric temperature variations are independent of the spatial locations within a 600km distance from the location of observation. This assumption possibly fails if the investigated region exceeds a larger horizontal coverage, i.e., a distance more than 3500km.

However, we want to point out that the vertical RO profiles follow a 3D curved path (cf., Fig. 3.2), which bends from the surface aloft during an occultation event due to the horizontal drift of the true tangent points. As a result, the GWs are likely to penetrate the retrieved path since they propagate both horizontally and vertically, i.e., they possibly propagate in and out of the curved signal path. Hence, we consider the GWs exhibited by the vertical temperature profiles (or perturbations) as a statistical ensemble, following the assumption of Rauthe et al. (2008).

In addition, we consider the GWs extracted from the 3-4 day averaging window are induced by the convective systems (hurricanes) only and do not include the Planetary Kelvin waves[13] or the Rossby waves[14]. These two types of waves have similar vertical wavelength scales compared to the CGWs, which are not easy to distinguish in the spectral analysis results. However, they have much longer periods of about 5-20 days, which are longer than the averaging window and should contribute to the background temperature profile (Steiner & Kirchengast, 1999).

[13] Atmospheric Kelvin waves are non-dispersive waves that balance the Coriolis force against a topographic boundary such as a coastline.

[14] Atmospheric Rossby waves are inertial waves that occur in the rotating fluids as a result of the potential vorticity conservation.

After obtaining the GW-induced temperature perturbation $T'(z)$ that is generated through convection, the spectral analysis and wavelet analysis can be applied. Strelnikova et al. (2021) applied a high-pass filter on the temperature perturbation $T'(z)$ that was extracted from lidar measurements. Specifically, they used the fifth-order Butterworth filter with a cut-off wavelength of 15km and a cut-off period of 8h. The purpose of this high-pass filtering was to keep only the short wavelength and short periods waves (Strelnikova et al., 2021).

In our analysis however, we do not apply any filtering in either the space or time domain so that we can observe all the GWs that are induced by the hurricanes. Besides, a high-pass filter can generate undesirable effects in the spectral results. For example, the power of some waves possibly increases for those that have a wavelength close to the cut-off wavelength. Since we keep both the long-wavelength and the short-wavelength components, the identification of different bands of waves becomes essential in this research.

3.3 Wave-induced vertical wind perturbations

In addition to the temperature perturbations, the GWs can also be studied through the wave-induced perturbations of vertical wind velocity. We use the wind data from the European Center for Medium-Range Weather Forecasts (ECMWF) system, which provides hourly data from 1950 to present and covers an altitude range from 0.1km to 32.4km (or in pressure levels as 1000hPa to 1hPa). Specifically, we use the fifth generation of ECMWF reanalysis dataset (ERA5) that has 37 vertical pressure levels and a horizontal spacing of 0.25° x 0.25° (Aragão, & Porcù, 2022). The fine horizontal resolution of the ERA5 dataset is able to offset the spare horizontal resolution of the RO retrievals.

According to Aragão, & Porcù (2022), the ERA5 dataset interpolates the atmospheric data onto different vertical pressure levels over the globe, by using the combination of the modelled results and the observations based on physics laws. ERA5 has a notably higher spatial and temporal resolution as well as higher data quality compared to its previous versions. These advantages lead to an improved performance of ERA5 in describing the atmosphere, especially in representing the gravity wave drag[15] through the variations of the horizontal wind and the air density (Hersbach et al., 2020).

For our research purposes, we use the eastward ($\bar{u} > 0$) and the northward ($\bar{v} > 0$) horizontal wind components from the ERA5 dataset to compute the horizontal wind velocity $\bar{u}_h$ at different altitude levels. Following Choi et al. (2009), the horizontal wind direction can be calculated as an angle φ that measures counterclockwise from the east:

$$\varphi = \arctan(\bar{v}/\bar{u})\,. \tag{3.3}$$

To keep consistency with the definition of azimuth, we convert the angle φ to the azimuthal angle α that measures clockwise relative to the north[16]. Hence, we refer to the azimuthal direction to describe both the horizontal wind direction and the RO profile location relative to the hurricane eye.

In addition, we also use the *vertical air speed* w from the ERA5 dataset that indicates the upward ($w < 0$) or the downward ($w > 0$) motion of the air[17] which is given in Pascal per second (Pa/s). The vertical air speed perturbation is very useful in describing the GW propagation pattern (Pahlavan et al., 2022). For example, Chen et al. (2012)

[15] Gravity wave drag is a zonal body force generated from the dissipation of the GWs.

[16] The determination of angle φ follows the trigonometric definition while its conversion to azimuth α follows the geodetic definition.

[17] Direction of air motion is defined in accordance with the ERA5 dataset and the sign of vertical wavenumber (Upward propagating waves have negative vertical wavenumbers).

demonstrated the spatial structure of the stratospheric GWs induced by Typhoon Matsa (2005), using the vertical wind velocity perturbation w' that illustrates a typical curve-like wave front. Similarly, we extract the vertical air speed perturbation w' at different altitude levels to reflect the horizontal propagation of the GWs in the $x-y$ plane (longitude-latitude) following:

$$w'(lon, lat, z, t) = w(lon, lat, z, t) - w_0(lon, lat, z). \quad (3.4)$$

In this thesis, we conduct wind perturbation analysis at three altitude levels that can roughly represent the upper troposphere (10km), the tropopause (15km) and the lower stratosphere (25km). For each altitude z, we calculate a *mean vertical air speed* $w_0(lon, lat, z)$ by averaging 24 hourly measurements within one day, which aims to represent the averaged vertical air motion at this altitude.

We use a shorter averaging period of 24 hours for wind data, since the wind structure changes much more rapidly than the variation of the atmospheric temperature. Furthermore, the wind propagation during the passage of a hurricane is far different compared to an undisturbed day. As a result, we use the vertical air speed data with the presence of a hurricane to calculate the mean vertical air speed, rather than from an undisturbed period as we did to construct the background temperature profile.

For each altitude of interest, the vertical air speed perturbation $w'(lon, lat, z, t)$ can be obtained by subtracting the 1-day averaged, mean vertical air speed $w_0\ (lon, lat, z)$ from the hourly data $w\ (lon, lat, z, t)$. The extracted perturbation w' is assumed to reflect the hurricane-induced GWs only. For simplicity, we will use the term *vertical wind perturbation* instead of the vertical air speed perturbation.

Although we closely follow Chen et al. (2012) to extract the vertical wind perturbations that are induced by the hurricanes, we choose to construct the mean vertical air speed w_0

using daily averages, while Chen et al. (2012) produced the mean state w_0 over the time period of Matsa's tropical storm stage. Besides, our mean vertical air speed is individually conducted for each altitude considering that the vertical wind perturbations vary with heights, since the hurricane-induced GWs are assumed to propagate primarily in the vertical rather than in the horizontal direction (Wu et al., 2022).

Furthermore, our work provides the potential to deduce the 3D propagation pattern of the GWs. With the analysis of the vertical wind perturbations at different altitudes, we are able to simulate the horizontal GW propagation at each altitude and compare those among various heights. The time evolution of the GW propagation is also possible to predict, as the ERA5 dataset provides the vertical air speed as an hourly variation. This knowledge can possibly lead to a significant development in the parametrization of the CGWs.

3.4 Least squares spectral analysis and wavelet analyses

To study the spectral characteristics of the GWs induced by hurricanes, we apply a weighted spectral analysis of the temperature perturbation profiles following the least-squares approach.

In spectral analysis, a *time series* is a non-deterministic function of an independent variable of time (Jenkins & Watts, 1968). Sometimes it can also be a random function of space, which we refer to as a *data series*. The statistical properties of a *stationary* time (data) series, such as the mean and the variance, do not change with time (space); while a *non-stationary* time (data) series has at least one statistical property that is time- (space-) dependent (Ghaderpour & Pagiatakis, 2017).

The *least-squares spectral analysis* (LSSA) is an alternative method to the classical Fourier spectral analysis, which can analyze both stationary and the non-stationary time

or data series. The least-squares approach allows the analysis of a time (data) series that is unequally spaced, unequally weighted and /or with gaps and shifts (Pagiatakis, 1999; Ghaderpour et al., 2018).

Pagiatakis (1999) provided a detailed description of the LSSA method. The LSSA fits sinusoids to the data series within the spectral band of interest and estimates the spectrum based on the least-squares fitted coefficients (see Appendix A). Trends and the datum shifts (offsets) present in the data series can be parametrized as well. The LSSA also determines a threshold value at the 95% or 99% confidence level above which the least-squares spectral peaks are statistically significant (Pagiatakis, 1999). From the output results of LSSA, we are able to report amplitude and phase information for each significant spectral component. This is a major improvement of this work compared to the previous spectral analysis results of the GWs (Kuester et al., 2008; Kim et al., 2014; Wang et al., 2021).

The *least-squares wavelet analysis* (LSWA) method is based on the LSSA method expanded to the time-frequency or the space-wavenumber domain, depending on the type of the input series. The LSWA is capable of analyzing unequally spaced and unequally weighted series with trends and offsets just as the LSSA, by decomposing the input series into small segments with a designed window size. In addition, it is also capable of computing a spectrogram through the least-squares approach, which describes the variation of the spectral peaks over time or space (Ghaderpour et al., 2018). Similar to the LSSA, we are also able to plot the statistical threshold for the spectrogram that is a stochastic surface above which the spectral peaks are significant at the 95% or 99% confidence level.

As mentioned, the main outputs from LSSA and LSWA are the spectrum and the spectrogram, respectively. The spectrum describes the power distribution of the

frequencies or wavenumbers that compose the total input signal. The spectrogram further illustrates the changes of the signal amplitude (or power) in the time-frequency (or space-wavenumber) domain. The power (square of the signal amplitude) of each spectral peak is usually expressed in *percentage variance*, which represents the contribution of the sinusoids of a specific frequency or wavenumber in the input signal (Ghaderpour & Pagiatakis, 2017). The power distribution can also be converted into the *power spectral density* (PSD) following Pagiatakis (1999):

$$PSD = 10log_{10}\left(\frac{s}{1-s}\right), \tag{3.5}$$

where s is the least-squares spectrum of the input signal in percentage variance and the PSD is expressed in decibels (dB).

Our work uses python software JUST (Ghaderpour, 2021) that applies the LSSA method and the MATLAB software LSWAVE (Ghaderpour & Pagiatakis, 2019) that implements the LSWA method. According to our research purposes, the spectrogram of our input data series records the vertical propagation of the GWs and presents the GW vertical wavelength variation with respect to altitude. This is an innovation of this work as for the first time, we are able to visually illustrate the changes of the GW vertical wavelength with respect to the varying background wind.

Prior to the spectral analysis process, we first apply a data window on the temperature perturbation profile $T'(z)$ following the approach of Hindley et al. (2015). The data window attenuates (tapers) the perturbation below 5km and above 30km, with a 2km linear taper at both ends. The purpose of the windowing is to focus on the UTLS region where the RO retrievals have the highest accuracy, since the temperature retrievals are contaminated at

the surface and in the upper stratosphere due to the signal multi-path[18] and the super refraction[19] (Foelsche et al., 2008).

The windowed temperature perturbation profile is then used as the input series for the spectral analysis. The input series is analyzed in the altitude-wavenumber domain, which is converted into the altitude-wavelength domain for convenience. The *sampling interval* of the input series, namely the vertical spacing of the temperature perturbation profiles, is 0.1km. With this sampling interval, we are able to search for GWs with a vertical wavenumber of up to 5km^{-1}. This wide spectral bandwidth cannot be provided by other observing techniques, given the high vertical resolution of RO temperature retrievals (Choi et al., 2009; Vergados et al., 2014).

We then supress (remove) the linear trend of the input series through LSSA and focus on a wavenumber range of 0.01-0.6 km^{-1} (corresponds to a vertical wavelength range of 1.6-100km). This range covers the wavenumber band of almost all hurricane-induced GWs according to the existing literature, which also provides an optimal spectral resolution.

As we discussed previously, the input temperature series to LSSA and LSWA is an equally weighted, equally spaced data series over space (altitude). The weight of the input series equals the inverse of the temperature perturbation variance, where the variance $\sigma^2(T'(z))$ is calculated as:

$$\sigma^2(T'(z)) = \sigma^2(T(z)) + \sigma^2(T_0(z)) + 2 \cdot \sigma(T(z)) \cdot \sigma(T_0(z)) \cdot \rho_{T,T_0}. \quad (3.6)$$

The individual temperature profile $T(z)$ reflects the atmosphere during the hurricane, while the background temperature profile $T_0(z)$ represents the normal or the undisturbed state

[18] Singal multi-path refers to the phenomenon that the radio signals travel to the receiving antenna through two or more paths.

[19] Super refraction indicates that the atmospheric refractivity gradient is well below the standard (the standard refractivity gradient reports a value of -79 to 0 N/km).

of the atmosphere. Hence, we consider the variables T and T_0 statistically independent at each altitude z. Accordingly, the covariance term in Eq. (3.6) is ignored.

The variance of the individual temperature profile $T(z)$ equals the square of the RO temperature retrieval accuracy ΔT, which we consider as constant of 0.3K following Hindley et al. (2015):

$$\sigma^2(T(z)) = \Delta T^2 . \tag{3.7}$$

Similarly, the variance of the background temperature profile reads:

$$\sigma^2(T_0(z)) = \frac{\Delta T^2}{N_{un}} , \tag{3.8}$$

where N_{un} is the number of the undisturbed temperature profiles that are averaged to construct the background profile $T_0(z)$. Hence, Eq. (3.6) becomes:

$$\sigma^2(T'(z)) = \Delta T^2 + \frac{\Delta T^2}{N_{un}}. \tag{3.9}$$

By formulating the variance $\sigma^2(T'(z))$ and the weight of the input series, we are able to calculate the variance of the amplitude and phase for each of the significant spectral peaks. The calculation of amplitude and phase variance is uniquely offered by the LSSA and LSWA, which significantly supports the validity of the spectral results.

Chapter 4

Gravity Waves Generated by Hurricane Dean (2007)

In this chapter, we carry out a detailed analysis to study the GW characteristics in the eyewall region of Hurricane Dean, following the methodology presented in Chapter 3.

Hurricane Dean is a classic Cape Verde cyclone in the Atlantic Ocean. It originated from a tropical wave on Aug. 11, 2007, crossed the west coast of Africa and was associated with a closed surface low pressure center and a strong easterly shear. The tropical storm then connected to the deep convection and moved westward, with a gradually decreasing easterly shear. It actually became a hurricane on Aug. 16, 2007, with the formation of a partial eyewall and a clear structure of the eye (Franklin, 2008).

错误!未定义书签。**Figure 4.1.** Best track of Hurricane Dean during Aug. 13-23, 2007. Locations of the temperature retrievals on Aug. 18 in the eyewall region (blue triangle) and in the rainband region (orange triangle) are shown.

Dean intensified quickly as it entered the Caribbean Sea and became a Category 5 hurricane on Aug. 21 over the Saffir-Simpson Hurricane Wind Scale. It weakened rapidly after its landfall and eventually became a depression that dissipated on Aug. 23. Dean is the first land-falling Category 5 hurricane in the central Atlantic Ocean since 1992, which was responsible for 32 deaths (ibid., 2008).

Figure 4.1 illustrates the best track of Hurricane Dean during Aug. 13-23, 2007 over the Atlantic Ocean. The locations (occultation tangent points) of the selected temperature retrievals in the eyewall region and the rainband region are marked with the blue and yellow triangles, respectively. The discussion of the thermodynamics and the GWs in the rainband region is presented in Chapters 8 and 9.

4.1 Eyewall temperature perturbations and thermodynamics

Based on our thresholds, only one temperature retrieval in the eyewall matches both the temporal and the spatial criterion. This retrieval was recorded at 0:11 UTC on Aug. 18, 2007, with a radial distance of 87km from the eye location[20]. Figure 4.2 illustrates the temperature profiles as well as the background temperature profile specifically constructed for Dean.

The background temperature profile $T_0(z)$ within the region of Hurricane Dean exhibits a temperature minimum at about 16-17km altitude (Fig. 4.2a), indicating the altitude of the tropopause when the atmosphere is not disturbed by the hurricane. Different from the background profile, the individual temperature profile $T(z)$ inside the eyewall exhibits two local temperature minima around this altitude with a temperature inversion between (Fig. 4.2a; shown in the black dashed frame), which displays as a double tropopause.

[20] Eye location was recorded by National Hurricane Center at 0:00 UTC on Aug. 18, 2007.

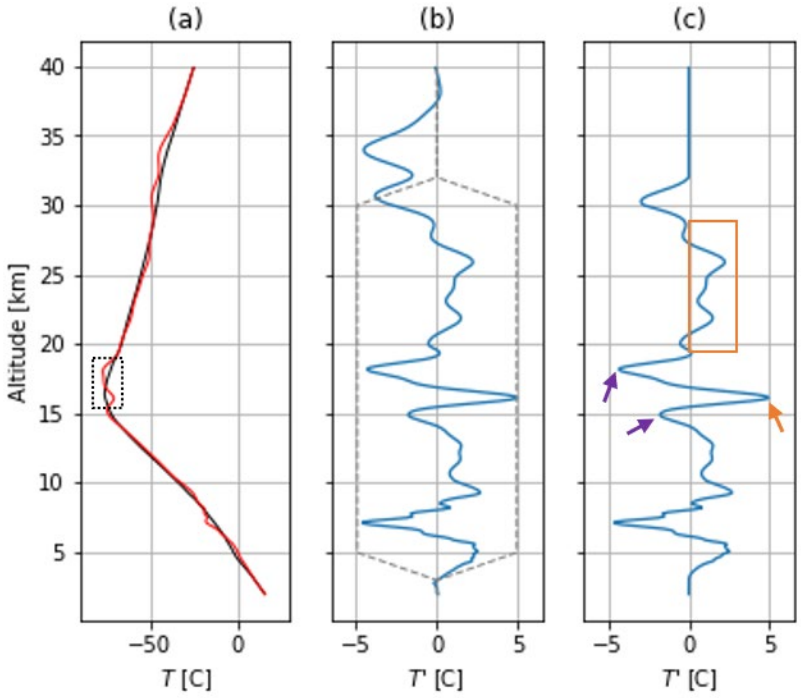

Figure 4.2. Temperature profiles from the RO retrieval at 0:11 UTC on Aug. 18, 2007 inside the eyewall region: (a) the background temperature profile $T_0(z)$ (black) and the retrieved temperature profile $T(z)$ inside eyewall (red), (b) the temperature perturbation profile $T'(z)$ (blue) and a tapered lag window (grey dashed) and (c) the windowed temperature perturbation profile $T'(z)$.

Vergados et al. (2014) observed a similar feature inside the eyewall for a few different hurricanes, such as Hurricane Vamco (2009, Category 4) and Hurricane Sepat (2007, Category 5), also using the vertical temperature profiles from the GPS-RO retrievals. Our analysis follows their criterion of locating the eyewall region and also uses the RO retrievals for the hurricanes with about the same intensity, which strongly verifies the existence of the double tropopause feature in the eyewall.

An enlarged view of the eyewall temperature perturbations is provided by the extracted temperature perturbation $T'(z)$ in Fig. 4.2b, while the windowed perturbation in Fig. 4.2c further focuses on the features presented in the UTLS region (5-30km altitude). First of all, there is a significant temperature anomaly of about -5°C at 7km altitude (cf., Fig 4.2c), which demonstrates the entrainment of cold air into a warm environment due to the boundary layer convergence.

In addition, as we observe in Fig. 4.2c, the double-tropopause feature displays as a temperature inversion located between the two temperature minima. Specifically, the local temperature minima produce temperature anomalies of about -2°C at 15km altitude and about -5°C at 18-19km altitude (marked with purple arrows), while the temperature inversion at 16km has a magnitude of 5°C (orange arrow). This temperature inversion results from the strong updrafts in the eyewall, suggesting the existence of deep convection (Vergados et al., 2014).

According to Yano (2021), deep convection lifts the warm, moist air parcels upward with a release of latent heat that provides a positive buoyancy through their ascent. As the air parcel rises, it expands adiabatically due to the decreasing pressure and experiences a temperature decrease. The decrease in temperature results in the condensation of the water vapour, where the release of latent heat again produces a positive buoyancy and the air parcel further rises. Eventually, the air parcel temperature drops to a value below or equal to the surrounding temperature. At that level, the air parcel reaches its equilibrium and oscillates around that level (Yano, 2021).

Based on the temperature perturbation presented in Fig. 4.2c, when the ascending warm air parcels in the eyewall reach an altitude of 15-16km, they possibly reach the equilibrium and oscillate around 16km, or sink back. Compared to the undisturbed period (shown as $T_0(z)$), this equilibrium level is slightly higher in altitude, since the warm air parcels carry larger momentum due to the latent heat release and the boundary layer convergence. As a result, we observe a strong temperature inversion above the temperature minimum at 15km altitude.

Moreover, if the air parcels ascend fast enough, they retain their momentum and are even able to overcome this equilibrium. When the air parcels overshoot upward, they enter a

colder environment as shown by the temperature minimum at 18-19km. This environment offers the conditions for the air parcels to further ascend and enter the lower stratosphere.

We believe that a small portion of the ascending air overcomes the equilibrium and rises freely from 15-16km altitude in the eyewall, which in turn generates the small temperature inversions at 19km and above, as framed by the orange rectangle (Fig. 4.2c). This observation of the stratospheric perturbations verifies the overshooting convection mechanism, which is considered to excite the small-scale vertically propagating GWs in the lower stratosphere (Stull, 1976).

We therefore consider that the double-tropopause structure provides favourable conditions for the overshooting convection. We want to point out that the eyewall region of a hurricane does not necessarily exhibit the double-tropopause feature and the feature itself does not guarantee the occurrence of the overshooting convection. However, it is highly possible that the intense hurricanes reveal such characteristics due to the strength of the deep convection and the amount of the latent heat release.

4.2 Spectral analysis of the GW characteristics and variations

The spectral result of the wave-induced temperature perturbation in the eyewall is then analyzed in accordance with the background wind conditions. Figure 4.3a presents a vertical profile of the horizontal wind speed in the vicinity of the eyewall at 0:00 UTC on Aug. 18, 2007, when the eyewall temperature retrieval was recorded.

In Fig. 4.3a, we observe a local maximum of the horizontal wind speed at 14-15km altitude, which is associated with the strong outflow at the flat top of Dean. This result explains the negative temperature perturbation at 15km altitude shown in Fig. 4.2c, which also suggests that the air parcels carry large angular momentum at this altitude.

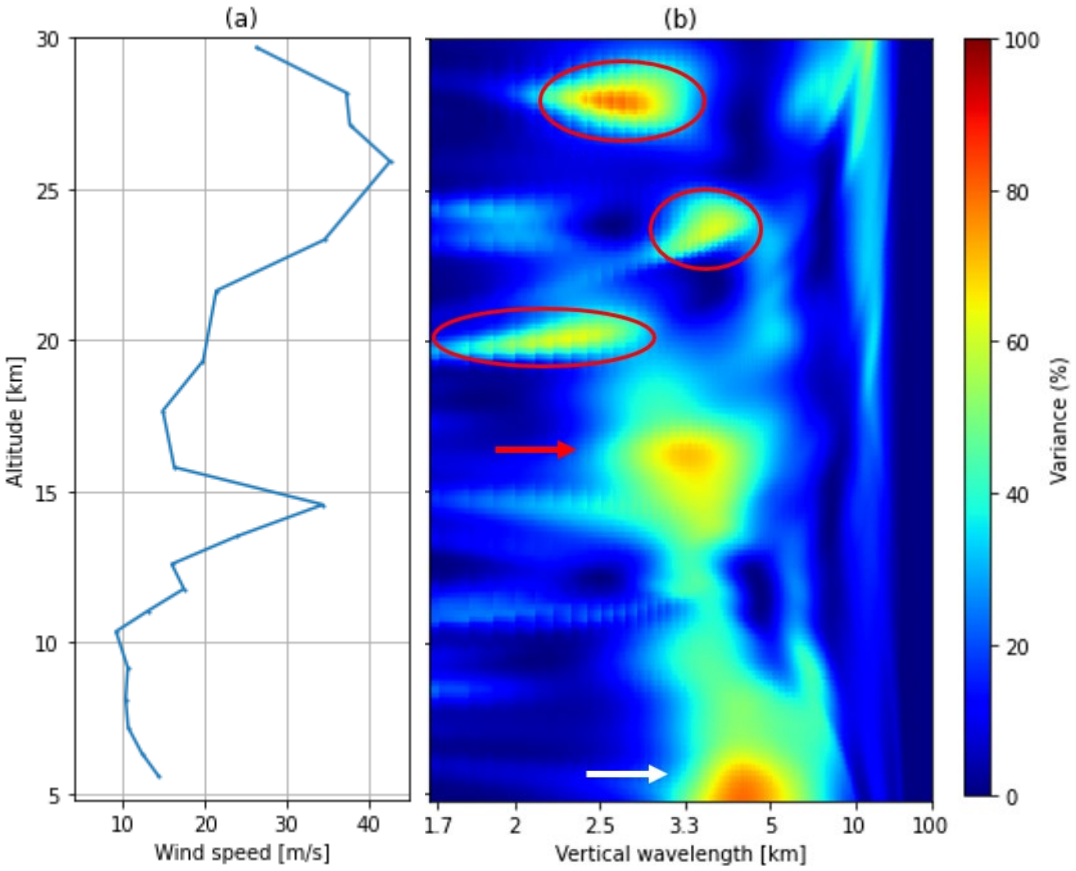

Figure 4.3. (a) Vertical profile of the horizontal background wind speed from ERA5 dataset at 0:00 UTC on Aug. 18, 2007 inside the eyewall region and (b) the normalized least squares spectrogram of the windowed temperature perturbation $T'(z)$ inside the eyewall.

Figure 4.3b shows the least squares altitude-wavelength spectrogram of the windowed temperature perturbation $T'(z)$. In Fig. 4.3b, we observe a wave near the Earth surface level with a vertical wavelength of 3-7km as denotated by the white arrow, which vanishes just below 20km altitude. Given its long vertical wavelength, we believe this wave component is generated via the pure thermal forcing mechanism.

In addition, the power of this wave is the highest at the Earth surface, which gradually decreases and reaches its minimum at about 12km altitude. At 12km altitude, only the component with $\lambda_z \approx$ 3-4km survives. This wave then grows in power during its upward propagation above 12km and the vertical wavelength attains a wider range of 3-7km again.

The vertical wavelength of this wave agrees with the CGW vertical scale that was reported by the previous studies of about 4-8km (Shi et al., 2021; Wang et al., 2021). However, the wavelength variation during the GW vertical propagation has not been discussed before. Hence, we aim to connect such GW variations with the wave generation mechanisms that were introduced in Chapter 2.

The eyewall temperature retrieval bends from the surface aloft in the southwest direction. We consider that the GWs revealed by this retrieval propagate in the same horizontal direction (SW) and vertically upward. The horizontal background wind over this region blows westward in the upper troposphere and above (not shown). As it turns out, the GWs revealed by this temperature retrieval propagate in a similar horizontal direction as the horizontal background wind.

The pure thermal forcing mechanism generates the long vertical wavelength, high power component at the surface. According to the GW dispersion relation (Eq. (2.8)), this component is also a high-frequency wave, namely the primary wave. Since the primary wave propagates along with the background wind, it experiences a Doppler-shift towards a shorter vertical wavelength as a result of the background wind filtering. The decrease in the vertical wavelength is most significant at 14-15km for this primary wave, where the background wind is the strongest with a value exceeding 30m/s.

At about 14-15km, overshooting convection starts to excite the vertically propagating GWs as demonstrated by the temperature inversion in Fig. 4.2c. Therefore, the power of the primary wave increases again due to the GW generation via the overshooting convection, as marked by the red arrow in Fig. 4.3b. The increase in power at 14-15km altitude in fact reflects the superposition of the GWs with multiple sources (Krisch et al., 2020).

There are also a few GW components with a short vertical wavelength above 20km altitude, namely the secondary waves that are circled with red lines (cf., Fig. 4.3b). We believe these components are possibly generated by the overshooting convection as well, which correspond to the small-magnitude stratospheric temperature perturbations at 20-30km altitude in the temperature perturbation profile (cf., Fig. 4.2c).

In short, we consider that the GWs observed in the UTLS region during the occurrence of Hurricane Dean are generated by both the pure thermal forcing mechanism and the overshooting convection. The pure thermal forcing dominates near the Earth surface level and generates a primary wave that experiences the background wind filtering. Based on our results, the overshooting convection dominates above the tropopause and produces some secondary waves. Although the background wind filtering is commonly observed in the hurricane-induced GWs (Kim & Chun, 2010; Wang et al., 2021), the GWs generated via the overshooting convection have not been previously revealed.

4.3 Vertical wind perturbations and the GW propagations

To further study the propagation of the GWs generated by Hurricane Dean, we extract the vertical wind perturbations at 0:00 and 2:00 UTC on Aug. 18, 2007. These perturbations are extracted at certain altitudes within the disturbed region of Dean, with a time interval (0:00-2:00 UTC) that covers the recorded time of the eyewall temperature retrieval (0:11 UTC), aiming to reflect the GW characteristics at a larger horizontal scale.

Figure 4.4 presents the vertical wind perturbations at three altitude levels. In the upper troposphere (Fig. 4.4e-f), the GWs generated by Dean display several tails that spread spirally outward in the anticlockwise direction (indicated by the black arrows), with a maximum power located north of the eye.

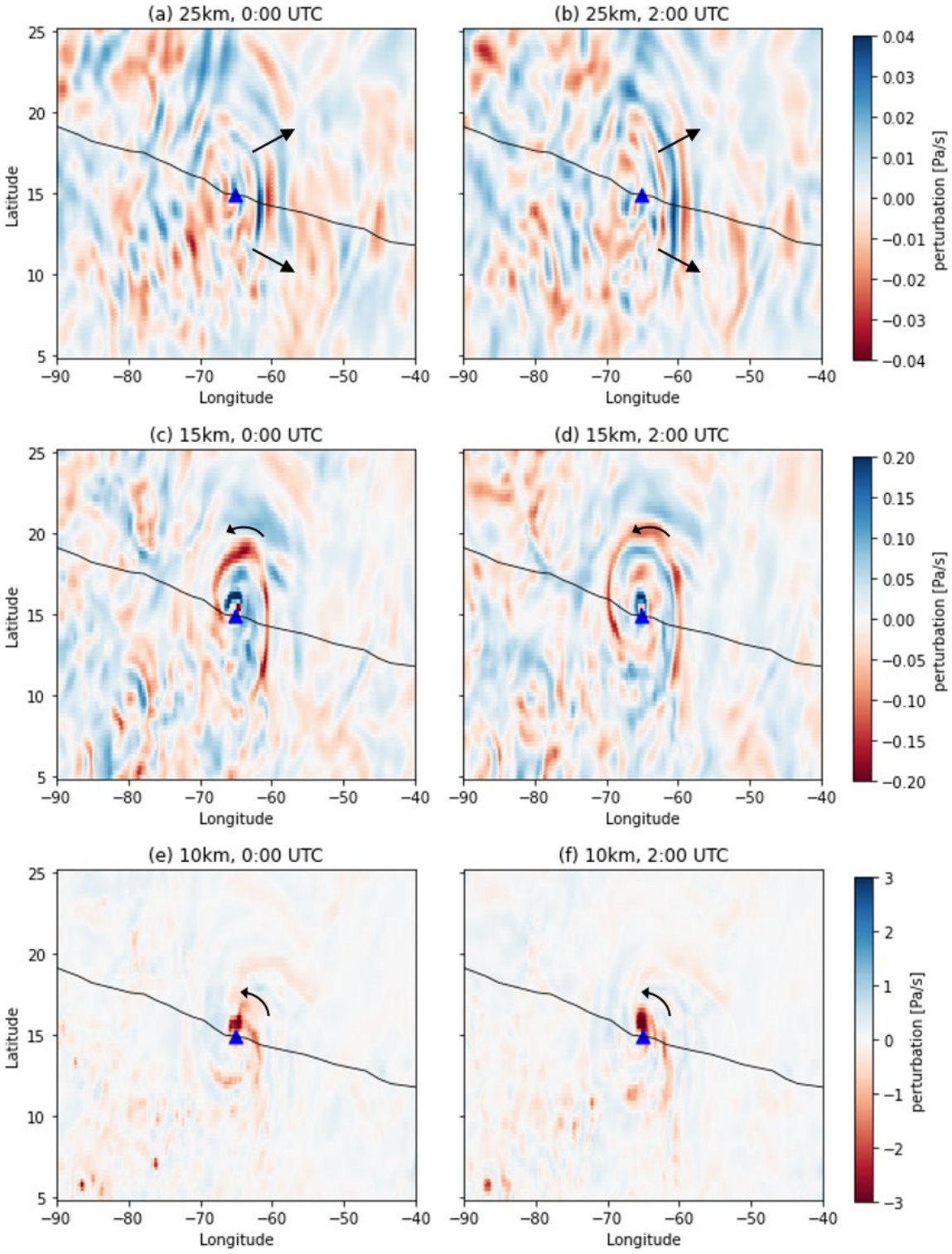

Figure 4.4. Vertical wind perturbation w' with the best track of Hurricane Dean (black): (a)-(b) at 25km altitude, (c)-(d) at 15km altitude and (e)-(f) at 10km altitude. The blue triangle denotes the recorded eye location at 0:00 UTC and the black arrows indicate the propagation direction of GWs. Left and right columns are captured at 0:00 and 2:00 UTC on Aug. 18, respectively.

The maximum power of the perturbations at this altitude (10km in the upper troposphere) has a negative value that indicates an upward air motion. Among the spreading tails, the tails on the east seem to prevail. The GW spiral propagation from the hurricane center in an anticlockwise direction verifies the similar findings of Wu et al. (2022) for the GWs induced by the Hurricane Joaquin (2015).

As the GWs propagate upward to the tropopause, this spiral structure becomes more distinct and spreads further from the eye as shown in Fig. 4.4c-d. The maximum power of the spiral is still located north of the eye, but the magnitude goes from negative to positive when transitioning from 10km to 15 km altitude. This change demonstrates that the majority of the air parcels ascend at 10km altitude and descend at 15km altitude around the location of the GWs maximum power.

In the lower stratosphere (Fig. 4.4a-b), the GWs reveal a concentric ring structure that displays as a stripped pattern, where the stripes propagate mainly in the east-west direction. Xu et al. (2019) also observed an asymmetric GW structure for Hurricane Matthew (2016) using measurements from Aqua satellites, where the eastward propagating waves prevail in the lower atmosphere.

Our perturbation analysis leads to a similar conclusion that is, the eastward propagating GWs dominate in the lower stratosphere (25km), while the westward propagating GWs seem to break into small pieces (cf., Fig 4.4a-b). This result further agrees with Xu et al. (2019), as they suggest that the concentric ring structure revealed by the primary waves possibly becomes a partial ring structure during the GW upward propagation.

The east-west asymmetry of the GW propagation is noteworthy and a possible reason is that the westward-propagating waves are modified by the west-blowing wind (easterly wind). The background wind reduces the vertical wavelength of the westward-propagating

waves and traps some waves through the critical level filtering, given the large horizontal wind speed of Dean. Therefore, we only observe small pieces of the westward-propagating waves at 25km altitude. Alternatively, the obstacle effect possibly generates GWs that are opposite to the background wind, i.e., the eastward-propagating waves. As a result, we find the eastward waves dominate at 25km altitude, which strongly justifies the similar results from Pahlavan et al. (2022), who also studied the GW propagation using the vertical wind perturbation extracted from the ERA5 dataset.

In general, the GWs generated by Dean display an isotropic field in the upper troposphere and behaves as an anisotropic field in the lower stratosphere, with a domination of the eastward-propagating waves. Kim and Chun (2010) noticed a similar phenomenon, where the GWs generated by Typhoon Saomai (2006) propagated mainly eastward in the stratosphere, due to the existence of the easterly wind shear that is known to modify the isotropic wave field (Kim et al., 2009; Nolan, 2020).

Aside from the GW propagation direction, we find that the magnitude of the vertical wind perturbation w' drops significantly from 10km to 25km altitude. The magnitude of w' can be considered as a proxy for the GW intensity, while the maximum magnitude at each altitude indicates the strongest upward or downward motion of air parcels. Based on Fig. 4.4, the maximum value of the vertical wind perturbation for Dean drops from 3Pa/s to 0.2Pa/s from 10km to 15km altitude, and then drops to 0.04Pa/s at 25km altitude. This significant decrease indicates that the GW intensity in the lower stratosphere is only about 1.3% of that in the upper troposphere. Therefore, the GWs experience a notable intensity attenuation during their upward propagation.

As stated by Stull (1976), the energy carried by the vertically propagating GWs can be lost through the turbulent layer in the upper troposphere, which may explain the significant

attenuation of the GW intensity. Furthermore, when strong temperature inversions are present around the tropopause, which is likely to appear for strong hurricanes, such as Dean, the loss of GW energy is small (Stull, 1976; Vergados et al., 2014). Hence, we expect the GWs generated by an intense hurricane experience a smaller intensity decrease compared to that from a weak hurricane.

Chapter 5

Gravity Waves Generated by Hurricane Julia (2010)

In this chapter, we present an analysis of the GW characteristics in the eyewall region of Hurricane Julia. Julia originated from a tropical wave that emerged from the west coast of Africa on Sept. 11, 2010 over the eastern Atlantic Ocean. It rapidly produced a tropical depression on Sept. 12 with a maintaining deep convection. Julia then moved west-northwestward, it slowly intensified and became a hurricane on Sept. 14.

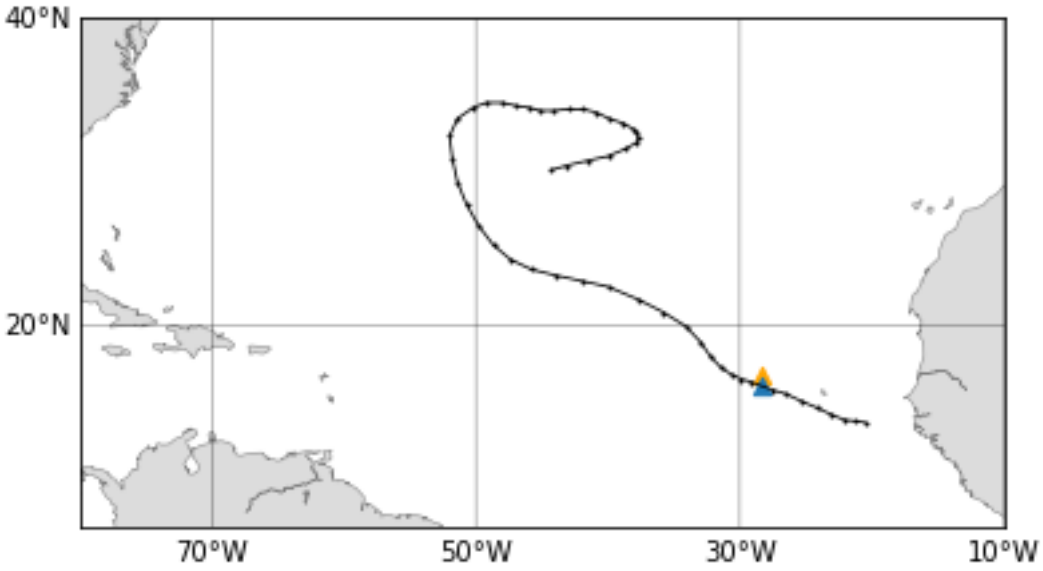

Figure 5.1. Best track of Hurricane Julia during Sept.12-25, 2010. Locations of the temperature retrievals on Sept. 14 in the eyewall region (blue triangle) and in the rainband region (orange triangle) are shown.

From Sept. 17, the low-pressure center of Julia started to get exposed due to the upper-level outflow of Hurricane Igor, which was located west to the Julia during that time and was much stronger than Julia. Julia then began to slowly decay and eventually dissipated

into an open trough on Sept. 24. Hurricane Julia is characterized as a Category 4 hurricane (Beven II & Landsea, 2010).

Figure 5.1 illustrates the best track of Julia over the Atlantic Ocean during Sept. 12-25, 2010. The locations of the selected temperature retrievals in the eyewall and the rainband region are also shown. One temperature retrieval is found inside the eyewall region that was recorded at 16:45 UTC on Sept. 14, 2010, when Julia became a hurricane. The retrieved temperature profile is located 84km away from the recorded eye location[21]. The discussion for the rainband region is presented in Chapters 8 and 9.

5.1 Eyewall temperature perturbations and thermodynamics

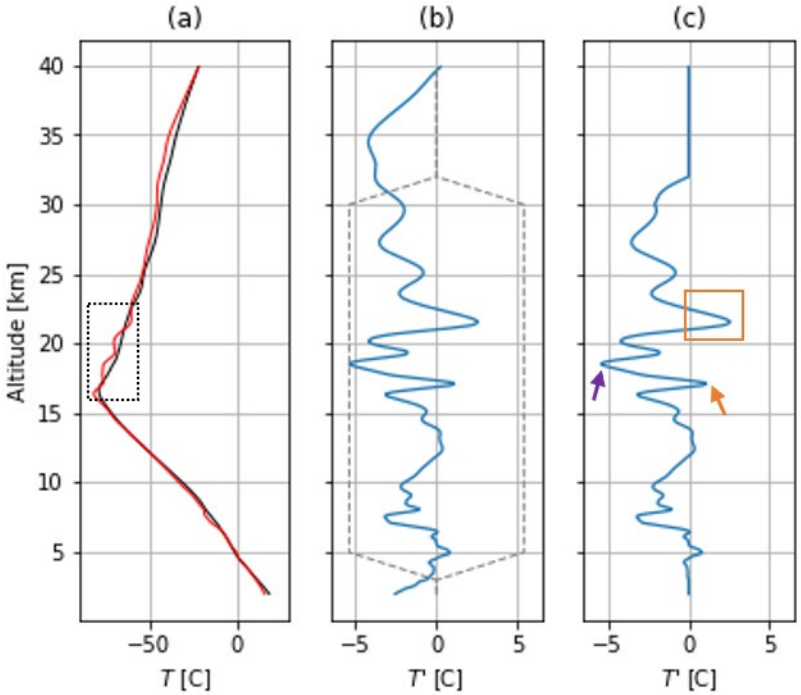

Figure 5.2. Temperature profiles from the RO retrieval at 16:45 UTC on Sept. 14, 2010 inside the eyewall region: (a) background temperature profile $T_0(z)$ (black) and retrieved temperature profile $T(z)$ inside eyewall (red), (b) temperature perturbation profile $T'(z)$ (blue) and a tapered lag window (grey dashed) and (c) the windowed temperature perturbation profile $T'(z)$.

[21] Eye location was recorded by National Hurricane Center at 18:00 UTC on Sept. 14, 2010.

Figure 5.2 presents the RO temperature profiles with a background temperature profile constructed for Hurricane Julia. The minimum value of the background temperature profile $T_0(z)$ occurs at about 16km altitude (Fig. 5.2a), demonstrating the normal tropopause level when the atmosphere is undisturbed. Compared to the background profile, the individual temperature profile $T(z)$ inside the eyewall reveals strong fluctuations above the tropopause as shown in the black dashed frame (Fig. 5.2a), which does not present a distinct double-tropopause feature as Hurricane Dean. These fluctuations are mainly due to the strong deep convection in the troposphere given the intensity of Julia (Vergados et al., 2014).

The windowed temperature perturbation $T'(z)$ again provides an enlarged view of the temperature fluctuations that are observed in Fig. 5.2a. The extracted perturbation $T'(z)$ illustrates the large-magnitude fluctuations at 15-20km altitude, with a maximum magnitude of 5°C around 19km altitude (cf., Fig. 5.2c), as indicated by the purple arrow.

We describe these fluctuations (15-20km altitude) as a triple-tropopause feature that is observed for the first time. The triple-tropopause is considered as an intense version of the double-tropopause feature, which contains two temperature inversions instead of one. However, only the temperature inversion at 17km altitude shows a positive perturbation value (orange arrow).

The triple-tropopause feature is located above the normal tropopause level, demonstrating that the strong temperature inversions cap the atmospheric boundary layer. This is a favorable condition for GW generation through overshooting convection, since the warm air parcels during their ascent enter a colder environment that further allows them to shoot upward into the overlying stable layer and excite GWs (Stull, 1976).

In fact, the positive temperature perturbation above 20km (orange square) in Fig. 5.2c implies that there are warm air parcels lying above these inversions, confirming that the air parcels make their way into the lower stratosphere through the upward overshooting. For all we know, this is the first time that the observational evidence is provided to support the existence of the overshooting convection within the eyewall region of an intense hurricane.

Moreover, this positive temperature perturbation also verifies the 'hot tower' structure described by Hoffmann et al. (2018), where the high clouds from the deep moist convection penetrate the tropopause and become a potential source of the stratospheric GWs. Given the large magnitude of this perturbation (cf., Fig 5.2c; circled by orange square), we conclude that the 'hot tower' structure of Julia is strong and corresponds to an intense overshooting convection. Therefore, we think that the GWs generated by the overshooting convection should be the most distinct in the spectral results for Julia.

5.2 Spectral analysis of the GW characteristics and variations

Figure 5.3a presents the horizontal wind speed profile in the eyewall region of Julia that was recorded at 17:00 UTC on Sept. 14, 2010, from the ERA5 dataset. We observe a local maximum of the horizontal wind speed between 15-20km altitude (cf., Fig. 5.3a), where the triple-tropopause feature occurs. This local maximum wind speed of Julia appears at a higher altitude with a smaller value (>20m/s) compared to that of Dean (>30m/s). Nevertheless, the horizontal wind speed of Julia still implies that the fast-rotating air carries large momentum, which also suggests that the overshooting air parcels from Julia possibly enter the region above 20km altitude where the overshooting top exists.

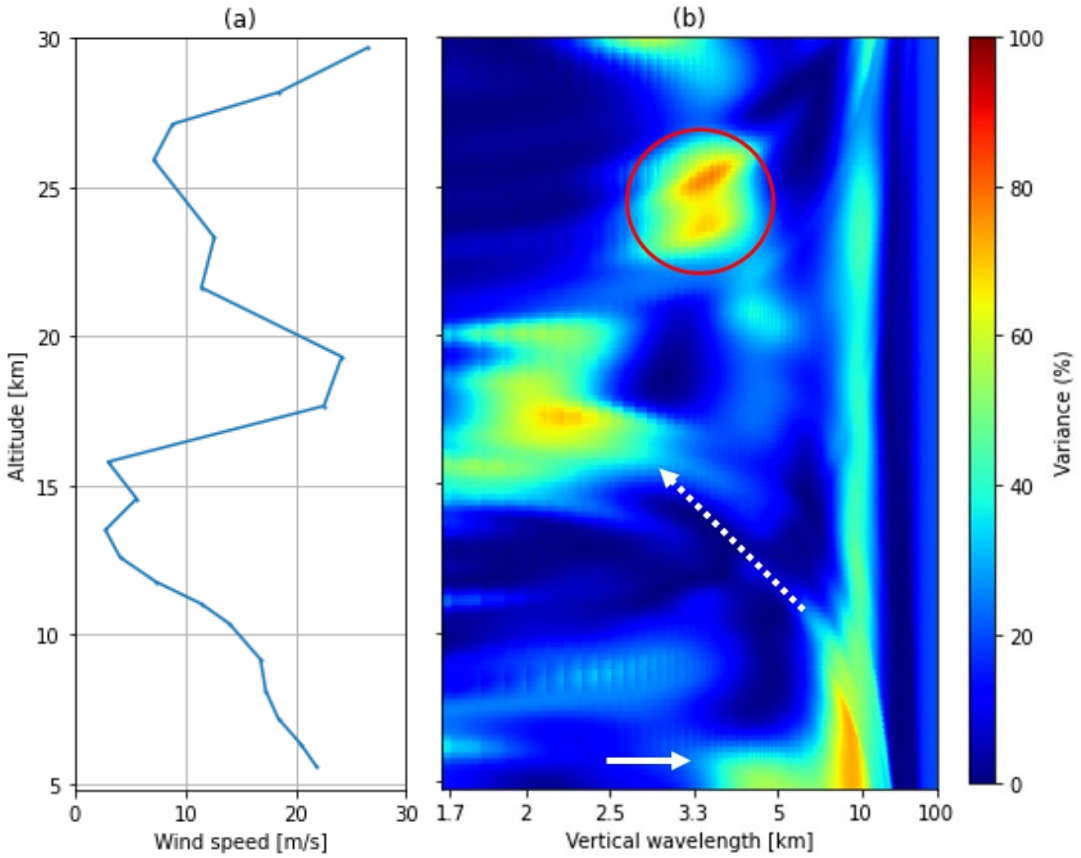

Figure 5.3. (a) Vertical profile of the horizontal background wind speed from ERA5 dataset at 17:00 UTC on Sept. 14, 2010 in the eyewall region and (b) the normalized least squares spectrogram of the windowed temperature perturbation $T'(z)$ inside the eyewall.

In addition to the eyewall wind speed, Figure 5.3b shows the spectrogram of the windowed temperature perturbation $T'(z)$ in the eyewall region. We observe a long-wavelength wave ($\lambda_z \approx$ 5-17km) at the surface in Fig. 5.3b that is likely generated by the pure thermal forcing mechanism as marked by the white arrow. This primary wave experiences a significant decrease in the vertical wavelength through its upward propagation (denoted by the white dashed arrow) and is trapped below 20km altitude, which is due to the background wind filtering as well as the critical level filtering (Mukherjee et al., 2010).

This primary wave is assumed to propagate horizontally southwestward and vertically upward following the assumption in Chapter 3, since the eyewall temperature retrieval bends from surface aloft in a southwest direction. The horizontal background wind also

blows westward in this region (not shown). As a result of the background wind filtering effect, the GW vertical wavelength is reduced with respect to the decreasing intrinsic frequency, as shown in Fig. 5.3b. This result is revolutionary, since the decrease in the GW vertical wavelength due to the background wind fileting has never been visually displayed and illustrated before.

Furthermore, the horizontal wind speed in the eyewall exceeds 20m/s at 18-19km altitude (cf., Fig. 5.3a), which is strong enough to shift the intrinsic frequency of the primary wave towards zero. Subsequently, the GW vertical wavelength drops to 1.7-2.5km and the wave seems trapped at this altitude due to the critical level wind filtering (Taylor et al., 1993). The trapping of the primary waves below the tropopause is noteworthy in the eyewall region of Julia, which partially contributes to the domination of the secondary waves in the lower stratosphere region.

In Fig. 5.3b, we also observe a wave with a vertical wavelength of 3.3-5km in the lower stratosphere at about 25km altitude (circled in red). This secondary wave is considered to be generated by the overshooting convection, because this wave is distinctly delineated and clearly of different wavelength from the tropospheric waves that are trapped below 20km. The obstacle effect is not considered as the generating source, since the vertical wavelength is within a small range meaning that the background wind does not play a significant role in the generation of this secondary wave.

Hence, we confirm that the overshooting convection exists during the occurrence of Julia on Sept. 14, 2010, which indeed generates the GWs that are distinct from other primary waves in the spectral results as our expectation. This justification is significant as it is the first time that we directly observe the trapping of the primary waves as well as the generation of the secondary waves via the overshooting convection, using the wavelet spectrogram.

5.3 Vertical wind perturbations and the GW propagations

Given the fact that the eyewall temperature retrieval was recorded close to 17:00 UTC, we extract the vertical wind perturbations at 17:00 and 19:00 UTC on Sept. 14, 2010 for Julia, shown as Fig. 5.4. It is worth pointing out that Hurricane Igor was located west to Julia on Sept. 14, therefore the GWs generated by Igor may interfere with the GWs induced by Julia.

Similar to Dean, we observe a domination of the eastward-propagating waves at all three altitude levels for Julia (cf., Fig. 5.4). With the presence of the west-blowing background wind, the eastward-propagating waves are refracted to longer vertical wavelength, while the westward-propagating waves are shifted to shorter vertical wavelength and eventually experience the critical level wind-filtering due to the strong horizontal wind.

As a result, the westward waves become more evanescent as the altitude increases, but the eastward waves seem to be amplified in the lower stratosphere due to the rarefied air density (Fig. 5.4a-b). This finding agrees with previous studies, where the domination of the eastward waves is commonly observed during the hurricane passage and the background wind filtering is considered to be the main reason (Kim et al., 2005; Kim et al., 2009; Mukherjee et al., 2010).

Aside from the background wind filtering, the GWs generated via the obstacle effect are also responsible for the domination of the eastward-propagating waves. Especially at 15km altitude (Fig. 5.4c-d), the majority of the GWs propagate eastward that is opposite to the horizontal background wind, which are likely generated via the obstacle effect.

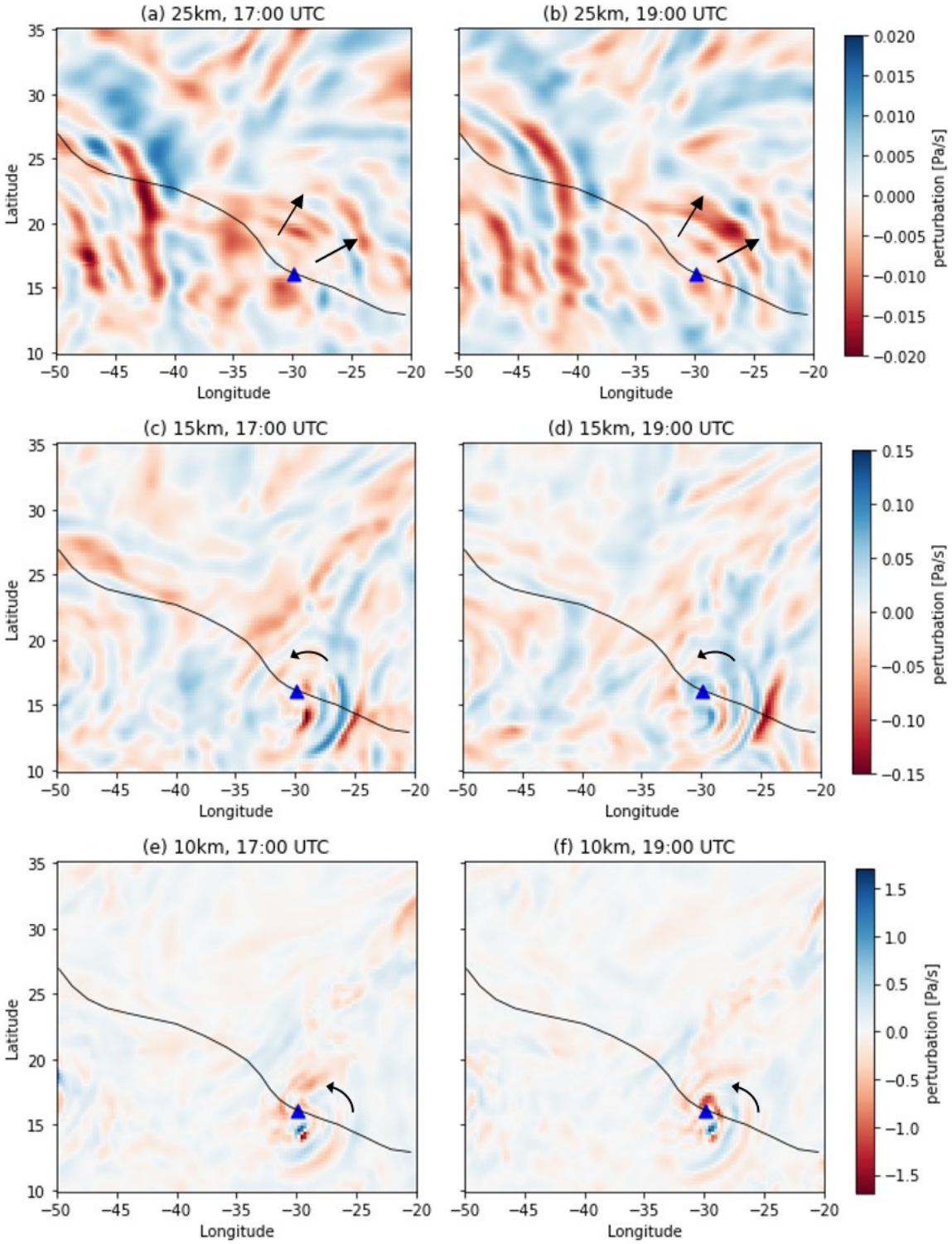

Figure 5.4. Vertical wind perturbation w' with the best track of Hurricane Julia (black): (a)-(b) at 25km altitude, (c)-(d) at 15km altitude and (e)-(f) at 10km altitude. The blue triangle denotes the recorded eye location at 18:00 UTC and the black arrows indicate the propagation direction of GWs. Left and right columns are captured at 17:00 and 19:00 UTC on Sept. 14, respectively.

Hence, we believe that the prevailing of the eastward-propagating waves observed in Julia is a result of both the background wind filtering and the obstacle effect. We also suggest that the obstacle effect dominates in the upper troposphere than the pure thermal forcing mechanism to generate the GWs, because the secondary waves seem to prevail in the UTLS region rather than the primary waves. This conclusion provides a new perspective to understand the asymmetric GW propagation, as we consider the asymmetric structure is due to multiple wave-related mechanisms rather than one.

Lastly, in terms of the vertical wind perturbation magnitude, the maximum magnitude of w' drops from 1.7Pa/s to 0.15Pa/s as the GWs propagate from the upper troposphere (10km) to 15km altitude, then drops to 0.02Pa/s at 25km. The maximum magnitude decrease reflects the maximum GW intensity in the lower stratosphere is only about 1.1% of that is in the upper troposphere.

Compared to Dean, the attenuation of the GW intensity in Julia is slightly higher during the GW upward propagation. This finding agrees with our expectation, because Julia reveals a slightly weaker temperature inversion compared to Dean and the loss of the GW energy is therefore higher, corresponding to a stronger attenuation of the GW intensity (Stull, 1976).

Chapter 6

Gravity Waves Generated by Hurricane Bill (2009)

This chapter presents a detailed analysis of the GWs that are induced by Hurricane Bill. Bill was determined as a category 4 hurricane which traversed the Atlantic Ocean. Bill developed from a tropical wave on Aug. 12, 2009, associated with a broad area of low pressure. A few rainbands developed on Aug. 14 with a reinforced deep convection that in turn formed a tropical depression on Aug. 15.

The tropical depression strengthened steadily under the weak vertical wind shear and became a hurricane on Aug. 17. After it turned northward, Bill slowly weakened due to the increasing wind shear. On Aug. 24, Bill eventually weakened to a tropical storm and quickly transited into an extratropical cyclone on the same day. On Aug. 26, Bill was absorbed by a larger extratropical cyclone (Avila, 2009).

The best track of Hurricane Bill over the Atlantic basin during Aug. 15-26, 2009 is shown in Fig. 6.1. We found one temperature retrieval in the eyewall region that is 105km away from the recorded eye location[22]. This eyewall temperature retrieval was recorded at 13:35 UTC on Aug. 17, 2009, when Bill had just become a hurricane. The location of the temperature retrieval in the rainband region is also shown in Fig. 6.1 and the analysis is presented in Chapters 8 and 9.

[22] Eye location was recorded by National Hurricane Center at 12:00 UTC on Aug. 17, 2009.

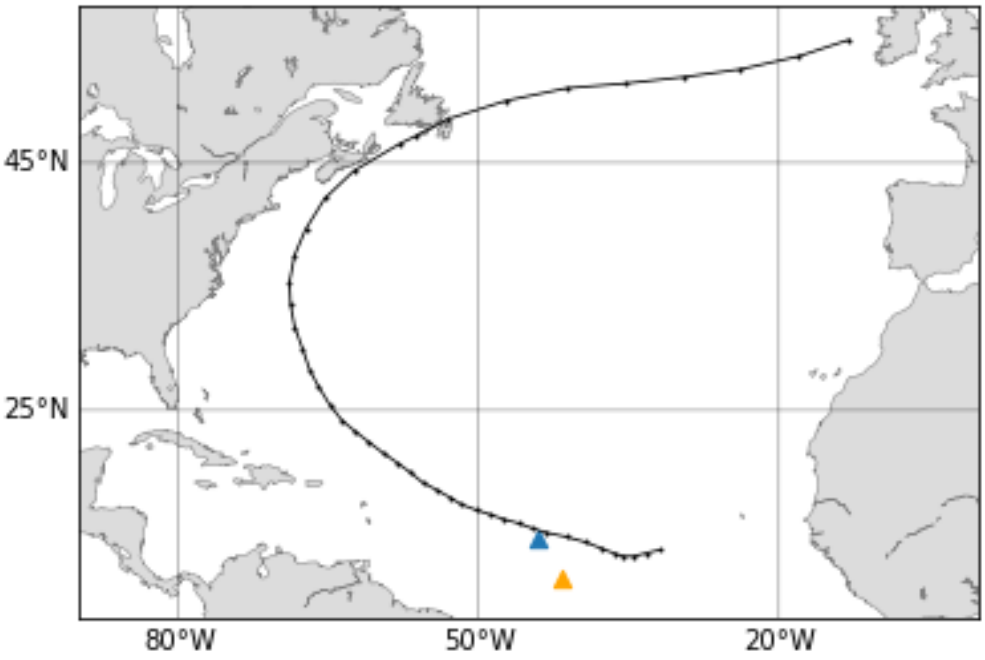

Figure 6.1. Best track of Hurricane Bill during Aug. 15-26, 2009. Locations of the temperature retrievals on Aug. 17 in the eyewall region (blue triangle) and in the rainband region (orange triangle) are shown.

Although Bill and Julia were both classified as category 4 over the Saffir-Simpson Hurricane scale, the sustained wind speed of Bill reported on Aug. 17 at 12:00 UTC (the time of our analysis) was slightly smaller compared to that of Julia. Therefore, we consider that the eyewall temperature retrieval for analyzing Bill reveals a less intense hurricane compared to Julia[23].

6.1 Eyewall temperature perturbations and thermodynamics

Figure 6.2 illustrates the temperature profiles from the RO retrieval located in the eyewall region, with a background temperature profile constructed specifically for Bill. The normal tropopause level of the analyzed region is about 16km altitude, indicated by the

[23] The sustained wind speed is one of the parameters to reflect the hurricane thermodynamics at the time of recording, which we use to roughly rank the hurricane intensity if more than one hurricane falls into the same category over the Saffir-Simpson Hurricane scale.

temperature minimum of $T_0(z)$ in Fig. 6.2a. Similar to what we have observed for Hurricane Dean (2007), the individual temperature profile $T(z)$ in the eyewall region of Bill also reveals the double-tropopause feature, circled by the black dashed frame.

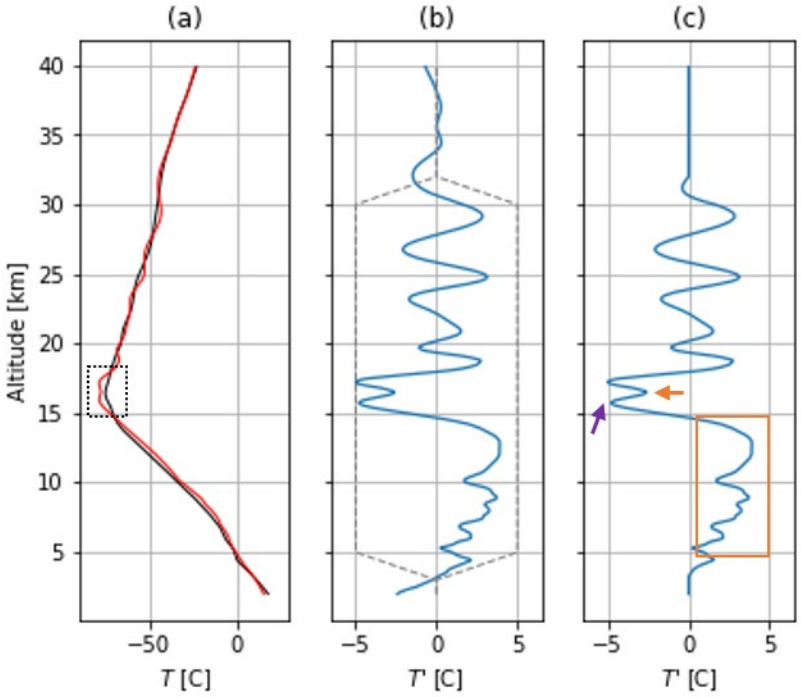

Figure 6.2. Temperature profiles from the RO retrieval at 13:35 UTC on Aug. 17, 2009 inside the eyewall region: (a) the background temperature profile $T_0(z)$ (black) and the retrieved temperature profile $T(z)$ inside eyewall (red), (b) the temperature perturbation profile $T'(z)$ (blue) and a tapered lag window (grey dashed) and (c) the windowed temperature perturbation profile $T'(z)$.

As shown in Fig. 6.2c, the local temperature minimums that compose the double-tropopause feature have a magnitude of about -5°C (purple arrow). However, the temperature inversion found between the two local minimums (marked by the orange arrow) is much smaller in Bill compared to the inversions in Dean. The small magnitude of the temperature inversion demonstrates that there are less warm air parcels overshooting above their equilibrium levels and hence the 'hot tower' structure is weak (Hoffmann et al., 2018).

The small temperature inversion is possibly due to the weaker convection in Bill (Category 4) compared to Dean (Category 5). A less vigorous convection generates weak surface instabilities and less amount of ascending air parcels. Therefore, the ascending air parcels in the eyewall of Bill are considered to have less buoyancy and vertical momentum, which are not sufficient to lift the air parcels upward to the lower stratosphere. Consequently, the overshooting convection is weak in Bill and only a small portion of the stratospheric GWs is excited via the overshooting convection.

In addition, the magnitudes of the temperature perturbations of Bill in the troposphere are positive (cf., Fig. 6.2c; shown in the orange frame), which is different from the previous cases. The positive tropospheric perturbations imply that the warm air parcels are lifted to a level below the normal tropopause where they stop rising any further. This result agrees with our assumption that there are less air parcels overshooting upward above their equilibrium levels into the lower stratosphere.

Furthermore, the eyewall temperature perturbation of Bill does not exhibit a negative anomaly at about 7-8km, as Dean and Julia did. The absence of such a negative anomaly indicates that the inflow in the boundary layer of Bill is weak compared to the previous hurricane cases. This finding further suggests that less air parcels ascend in the eyewall due to the small buoyancy, which leads to a weak overshooting convection.

On the other hand, the temperature perturbations between 20km and 30km altitude are more notable in Bill (cf., Fig. 6.2c). These perturbations have large and uniform magnitudes compared to those in Dean and Julia, which behave as a sinusoid. Given the fact that the overshooting convection is weak in exciting the GWs in the lower stratosphere, we believe that another wave-generating mechanism dominates in producing these strong stratospheric disturbances rather than the pure thermal forcing mechanism or the overshooting convection.

For instance, the obstacle effect or the mechanical oscillator mechanism possibly dominate in the lower stratosphere, which we need to verify through the spectral analysis results and the wave-induced wind perturbations. The GWs generated by the mechanical oscillator effect are not easy to identify, since the key parameter to distinguish such waves is their intrinsic frequency, which is not available based on the RO temperature measurements and the ERA5 dataset.

6.2 Spectral analysis of the GW characteristics and variations

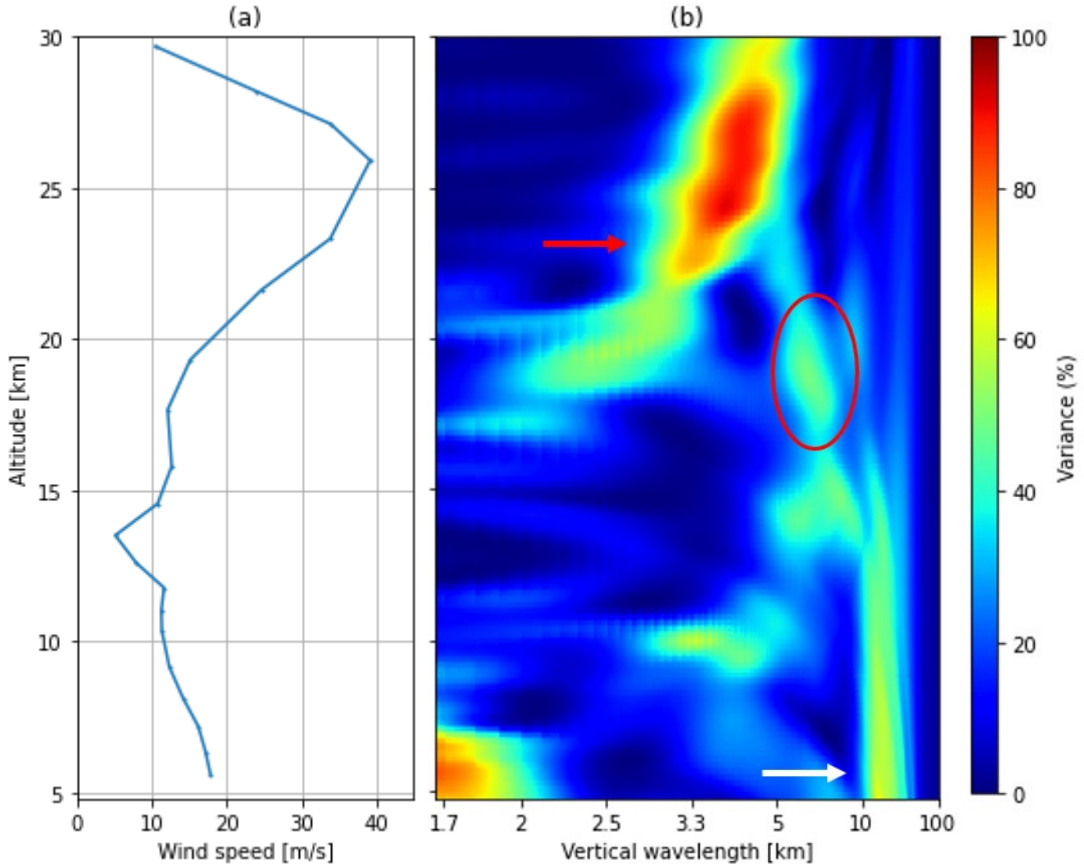

Figure 6.3. (a) Vertical profile of horizontal background wind speed from ERA5 dataset at 14:00 UTC on Aug. 17, 2009 in the eyewall region and (b) the normalized least squares spectrogram of the windowed temperature perturbation $T'(z)$ inside the eyewall.

The horizontal background wind speed and the wavelet spectrogram of the windowed temperature perturbation in the eyewall region of Bill are shown in Fig. 6.3. The maximum

wind speed in the eyewall occurs above 25km altitude and there is no local maximum in the UTLS region (cf., Fig. 6.3a). The horizontal wind speed is smaller than 20m/s below 20km altitude, suggesting that the background wind filtering is weak in the eyewall region and the GWs should not be modified much in the troposphere.

In Fig. 6.3b, the primary wave observed at surface level with a vertical wavelength of 11-20km verifies the wind speed result (denotated with the white arrow). This primary wave does not experience any shifts of vertical wavelength and propagates straight upward to 15km altitude, where the equilibrium level of the air parcels is assumed. This result justifies that the background wind filtering is almost absent in the troposphere. Above 15km altitude, the wave components with $\lambda_z \approx$ 5-10km are observed (Fig. 6.3b; circled by red), which is possibly a result of the weak overshooting convection as discussed earlier.

Interestingly, Bill reveals a stratospheric wave with a significantly increasing vertical wavelength as it propagates upward from 19-20km altitude, as marked by the red arrow (cf., Fig. 6.3b). The vertical wavelength increase is due to the presence of the strong stratospheric wind that blows in an opposite direction to the GW (Cowling et al., 1971; Kim et al., 2009).

The eyewall temperature retrieval of Bill bends in the northeast direction from the surface aloft. We therefore assume that the GWs exhibited by this retrieval propagate horizontally northeastward and vertically upward, which is in the opposite direction to the horizontal background wind (easterly wind). Due to the background wind filtering, the vertical wavelength of the stratospheric GW is refracted longer and the GW intrinsic frequency also increases (Fritts & Alexander, 2003).

Besides, the stratospheric GW grows not only in its vertical wavelength but also in its power as shown in Fig. 6.3b. The large power of the stratospheric GW agrees with our

observation of the strong temperature fluctuations in the lower stratosphere as shown in Fig. 6.2c. The increase in both the GW power and the GW vertical wavelength suggests that the majority of the stratospheric waves propagate opposite to the background wind. Thus, we believe that the obstacle effect dominates in generating the GWs above 19-20km altitude, which primarily produce the eastward-propagating waves.

6.3 Vertical wind perturbations and the GW propagations

The vertical wind perturbations of Bill are illustrated in Fig. 6.4. These perturbations are captured at 13:00 and 15:00 UTC on Aug. 17 over the hurricane-disturbed region, which covers the recorded time of the eyewall temperature retrieval (14:00 UTC).

In the upper troposphere of the hurricane-disturbed region (Fig. 6.4e-f), a blurry spiral pattern is observed that spreads radially outward in the anticlockwise direction, with a large power located west to the eye. However, we do not observe a well-developed GW concentric ring structure around the hurricane center as shown in the previous two hurricanes.

At the tropopause level (Fig. 6.4c-d), the spiral structure is still not distinct and the maximum power drifts to the east. The drift of the maximum power indicates that the obstacle effect possibly starts to dominate from the tropopause level. The GWs seem to be trapped within a small radial distance from the eye, because the GWs appear to be interfered further from the hurricane. We are not very certain about the exact causes for this interference.

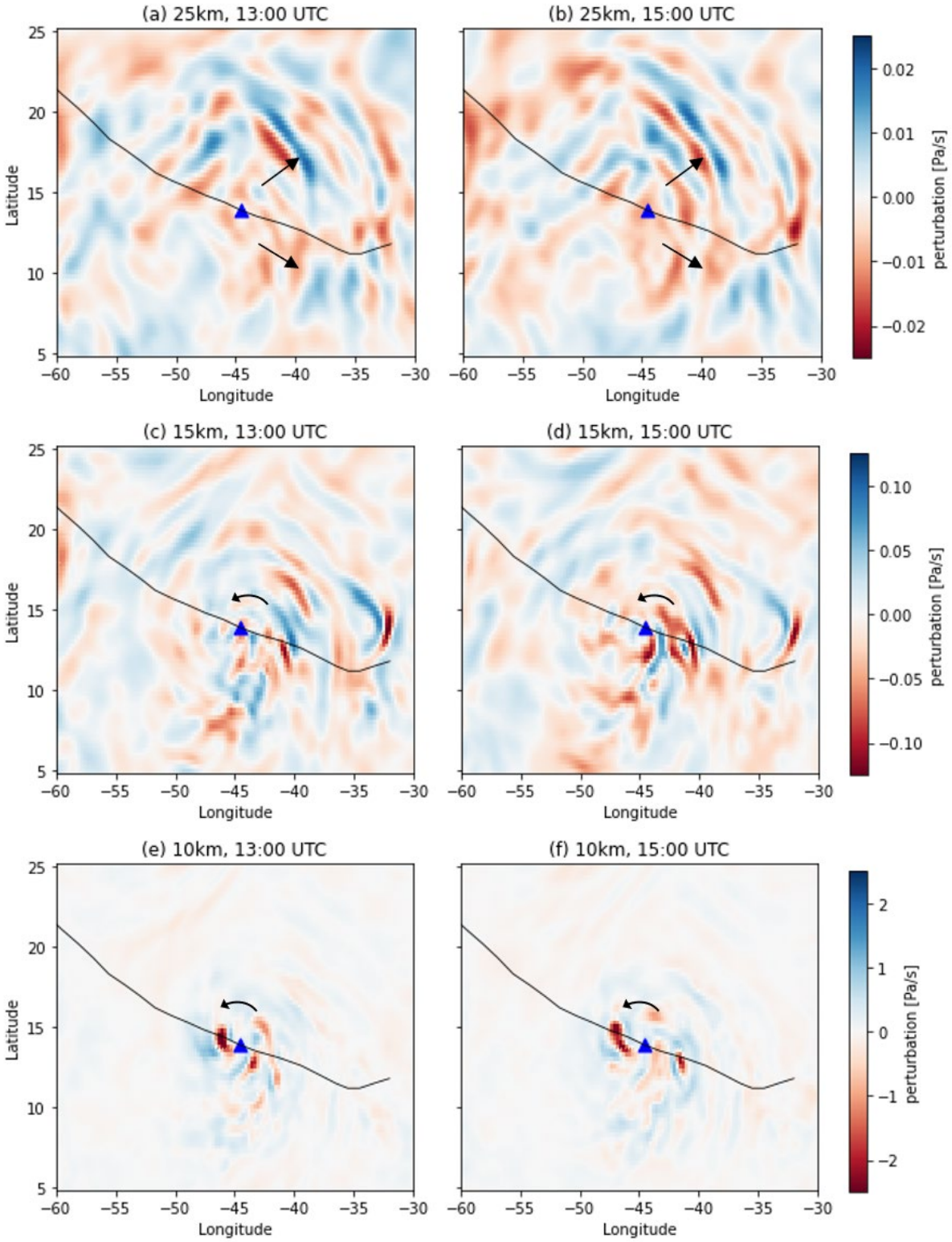

Figure 6.4. Vertical wind perturbation w' with the best track of Hurricane Bill (black): (a)-(b) at 25km altitude, (c)-(d) at 15km altitude and (e)-(f) at 10km altitude. The blue triangle denotes the recorded eye location at 12:00 UTC and the black arrows indicate the propagation direction of GWs. Left and right columns are captured at 13:00 and 15:00 UTC on Aug. 17, respectively.

The GW perturbations become more distinct in the lower stratosphere (Fig. 6.4 a-b) where only the eastward-propagating waves are observed. This anisotropic wave field supports our assumption that the obstacle effect dominates in the lower stratosphere and generates the majority of the secondary waves, which causes a strong asymmetry in the wave field. The direction of the hurricane motion (west-northwestward) possibly also contributes to the west-east asymmetry in the wave field, since Kim et al. (2009) also observed a maximum GW power in the typhoon moving direction that results in an asymmetric field.

Besides, based on the analytic results shown in Fig. 6.4, the maximum magnitude of the vertical wind perturbation drops from 2.5Pa/s to 0.025Pa/s, through the GW upward propagation from the upper troposphere to the lower stratosphere. The GWs experience an intensity attenuation of about 99% based on our results, which is considered relevant to the energy loss through the turbulent layer as stated by Stull (1976). This intensity attenuation is stronger than either of the two previous hurricanes (Dean and Julia), possibly due to the weak temperature inversion displayed above the tropopause of Bill.

Chapter 7

Gravity Waves Generated by Hurricane Bertha (2008)

This chapter presents a detailed analysis of the GWs that are induced by Hurricane Bertha. Bertha originated from a tropical wave on July 1, 2008, which gradually developed with the existence of the weak vertical wind shear and the warm sea surface temperature. It became a tropical depression on July 3 and turned into a tropical storm on the same day. As Bertha moved westward, it became the first hurricane of the 2008 season on July 7 and soon turned into a major hurricane after a rapid intensification (Rhome, 2008).

Figure 7.1. Best track of Hurricane Bertha during July 3-21, 2008. Locations of the temperature retrievals on July 8 in the eyewall region (blue triangle) and in the rainband region (orange triangle) are shown.

According to Rhome (2008), Bertha weakened for a short time period on July 8 under the effects of the strong vertical wind shear, which intensified again on July 9. From July 10, Bertha formed its second outer eyewall and the inner eyewall dissipated. The eyewall replacement led to a gradual weakening and Bertha became an extratropical cyclone on July 20, which eventually merged with a mid-latitude low pressure area on July 21. Bertha was determined as a category 3 hurricane and was the longest-lived Atlantic hurricane in July on record.

Figure 7.1 illustrates the best track of Bertha over the Atlantic Ocean from July 3-21, 2008. One temperature retrieval is found in the eyewall region that matches both the temporal and the spatial criteria. This retrieval was recorded at 14:19 UTC on July 8, 2008, which was only 36km away from the recorded eye location[24]. The analysis of the rainband region temperature retrieval (orange triangle) will be presented in Chapters 8 and 9.

7.1 Eyewall temperature perturbations and thermodynamics

Temperature profiles from the eyewall retrieval are shown in Fig. 7.2. Interestingly, the background temperature profile $T_0(z)$ of Bertha has already shown a weak double-tropopause feature as enclosed by the black dashed square (cf., Fig. 7.2a). The two local temperature minima of the double-tropopause occur at about 14km and 17km altitude. This feature indicates that the atmosphere is convectively active during the undisturbed period and produces favorable conditions for a hurricane to develop.

In Fig. 7.2c, the temperature perturbations in the eyewall region of Bertha also illustrate the double-tropopause feature, marked by the purple arrow. The temperature inversion found between the temperature minima is even smaller than that of Hurricane Bill. Besides,

[24] Eye location was recorded by National Hurricane Center at 12:00 UTC on July 8, 2008.

the temperature perturbations of Bertha in the troposphere are positive in magnitude, with a small anomaly located at about 7km altitude that corresponds to an intrusion of cold air.

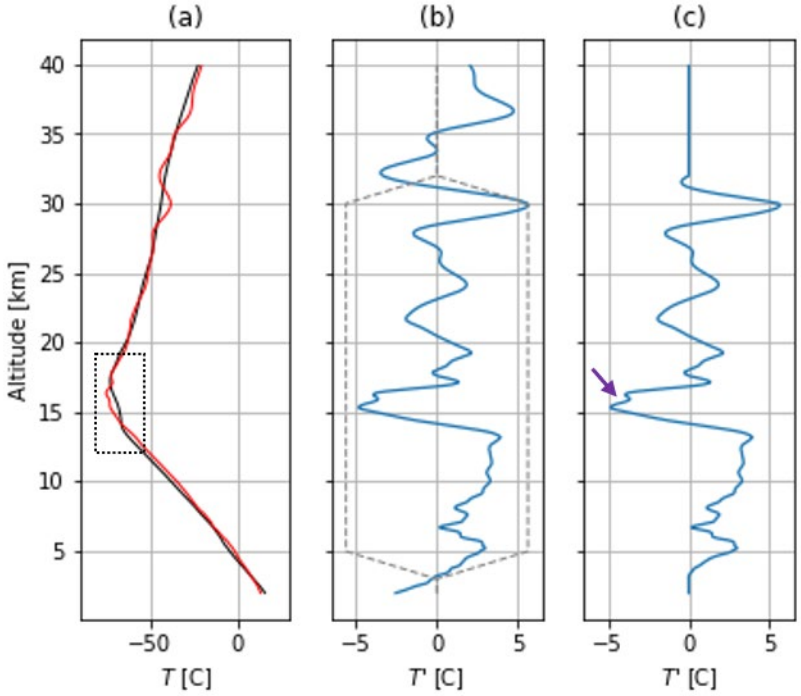

Figure 7.2. Temperature profiles from the RO retrieval at 14:19 UTC on July 8, 2008 inside the eyewall region: (a) the background temperature profile $T_0(z)$ (black) and the retrieved temperature profile $T(z)$ inside the eyewall (red), (b) the temperature perturbation profile $T'(z)$ (blue) and a tapered lag window (grey dashed) and (c) the windowed temperature perturbation profile $T'(z)$.

Since the temperature perturbations of Bertha exhibit similar characteristics to those of Bill, we believe that the boundary layer convergence in Bertha is not intense, and the deep convection is less vigorous. Hence, the updraft in the eyewall region of Bertha is weak in forming the 'hot tower' structure, which does not penetrate the tropopause like previous hurricanes (Hoffmann et al., 2018). The overshooting convection is therefore very weak as less ascending air parcels achieve the lower stratosphere.

Besides, the temperature fluctuations between 17km and 30km altitude in Fig. 7.2c are also relatively uniform in magnitude with a sinusoidal shape, displaying a similar structure as Bill. Considering the fact that the overshooting convection is very weak or even does not exist in Bertha, the stratospheric waves are likely generated via other mechanisms.

7.2 Spectral analysis of the GW characteristics and variations

Fig. 7.3a presents the horizontal background wind speed in the eyewall region and Fig. 7.3b shows the spectrogram of the windowed temperature perturbation $T'(z)$ inside the eyewall of Bertha. We observe two primary waves at the surface level in Fig. 7.3b. The first one has a vertical wavelength of about 3.3-7km (circled by red), while the second one reports a vertical wavelength of about 11km (marked by the white arrow).

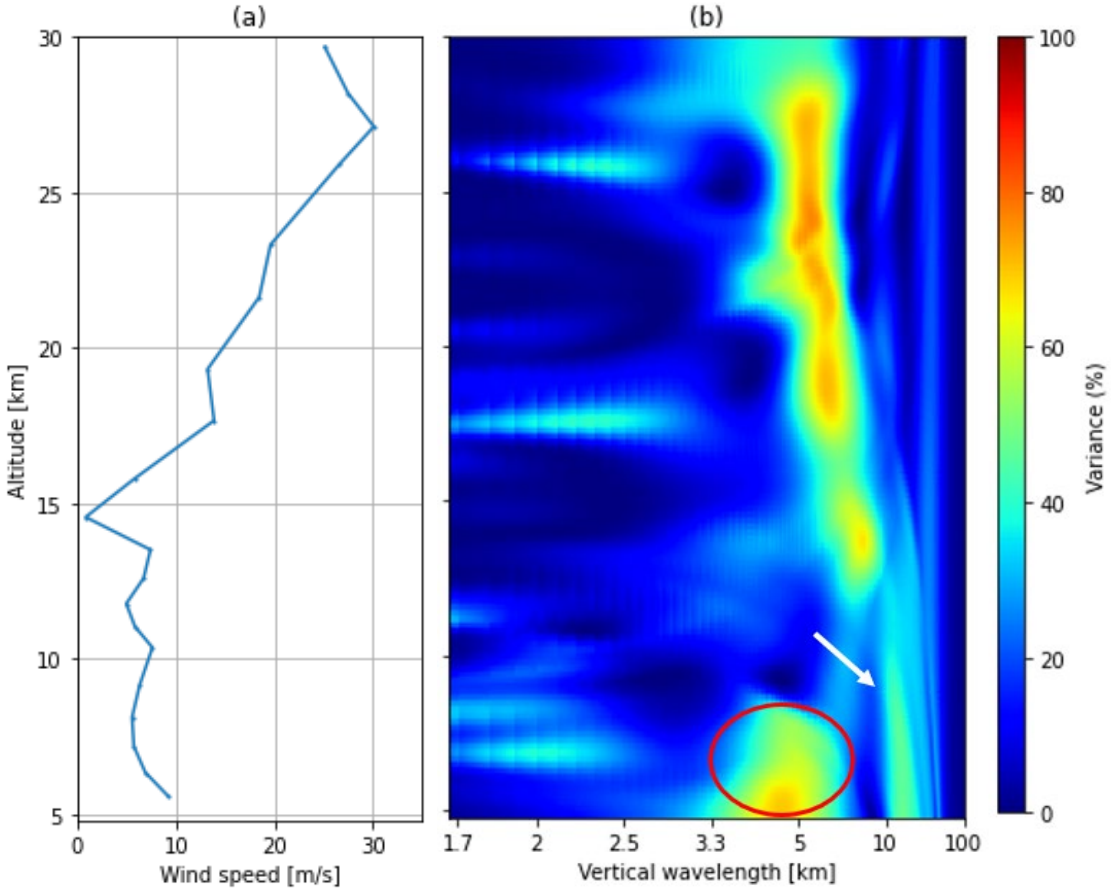

Figure 7.3. (a) Vertical profile of horizontal background wind speed from ERA5 dataset at 14:00 UTC on July 8, 2008 in the eyewall region and (b) the normalized least squares spectrogram of the windowed temperature perturbation $T'(z)$ inside the eyewall.

We think that both primary waves are generated through the pure thermal forcing mechanism. First of all, the deep convection in Bertha might not be as vigorous as in the previous hurricane, as a result the GWs possibly have a shorter vertical wavelength due

to the small heating depth of the thermal forcing (Beres et al., 2002; Fritts & Alexander, 2003). The primary wave circled by red ($\lambda_z \approx$ 3.3-7km) in Fig. 7.3b verifies this assumption. In addition, this wave only propagates to about 8-9km altitude and seems to be trapped there, or is absorbed by the other primary wave ($\lambda_z \approx$ 11km).

In contrast, the second primary wave ($\lambda_z \approx$ 11km) displays a vertical wavelength that is larger than the previously reported CGW vertical scale (Shi et al., 2021; Wang et al., 2021). However, it agrees with Wu et al. (2022) where their simulations show the peak vertical wavelength of the hurricane-induced GWs is about 10-14km.

This primary wave (cf., Fig. 7.3b; marked by the white arrow) propagates upward from the surface without being trapped and even enters the stratosphere. During its upward propagation, this wave experiences a slight decrease in the vertical wavelength and the decrease becomes more significant as altitude increases.

Again, this is a result of the background wind filtering. The GWs exhibited by this RO retrieval propagate southwestward in a similar direction to the background wind, which blows westward. The horizontal background wind speed does not exceed 20m/s below 20km altitude and is the weakest among all the hurricanes that we have studied. Consequently, no trapping of the primary wave is observed in the troposphere region based on Fig. 7.3b, since the critical level filtering is very unlikely to happen.

The modification of the vertically propagating waves is not significant compared to the previous cases, due to the small background wind speed. However, the background wind speed in the eyewall increases with altitude (cf., Fig. 7.3a), which leads to an increasing reduction of the vertical wavelength for the westward propagating GWs. Correspondingly, the GW intrinsic frequency gradually decreases as reflected by the long-wavelength primary wave ($\lambda_z \approx$ 11km), although the power of this primary wave remains unchanged.

Based on the spectrogram (Fig. 7.3b), we do not observe any distinct secondary waves that are generated via the overshooting convection. The absence of the secondary waves agrees with our assumption that the overshooting convection possibly do not exist in Bertha. Furthermore, we think that the stratospheric GWs are in fact the primary waves generated at surface which propagate upward into the stratosphere without being trapped.

7.3 Vertical wind perturbations and the GW propagations

To study the GW propagation of Bertha, Fig. 7.4 illustrates the vertical wind perturbations at three altitude levels over the hurricane-disturbed region. These wind perturbations are captured at 21:00h and 23:00h UTC on July 9, which are close to the recorded time of the eyewall temperature retrieval.

The GWs observed in the upper troposphere (cf., Fig. 7.4e-f) exhibit a partial spiral structure, similar to the previous hurricanes. The partial spiral spreads primarily in the northwest direction with a maximum power located at the center that has a negative perturbation value, indicating the existence of a strong updraft.

Interestingly, there is another strong perturbation located southeast to the spiral with a positive magnitude (Fig. 7.4e-f), indicating the location of a strong downdraft. The closely located updraft and downdraft demonstrate a northwest-southeast GW asymmetry that actually falls in the direction of hurricane motion. Our finding agrees with Kim et al. (2009) where they also found a GW asymmetry in the moving direction of Typhoon Ewiniar (2006).

At the tropopause level (Fig. 7.4c-d), the spiral structure is still visible with a negative perturbation in all directions, indicating that the air ascends only and the strong downdraft disappears. Besides, the outermost band of the spiral seems to propagate further away from the hurricane center as the GWs propagate upward from 10km to 15km altitude.

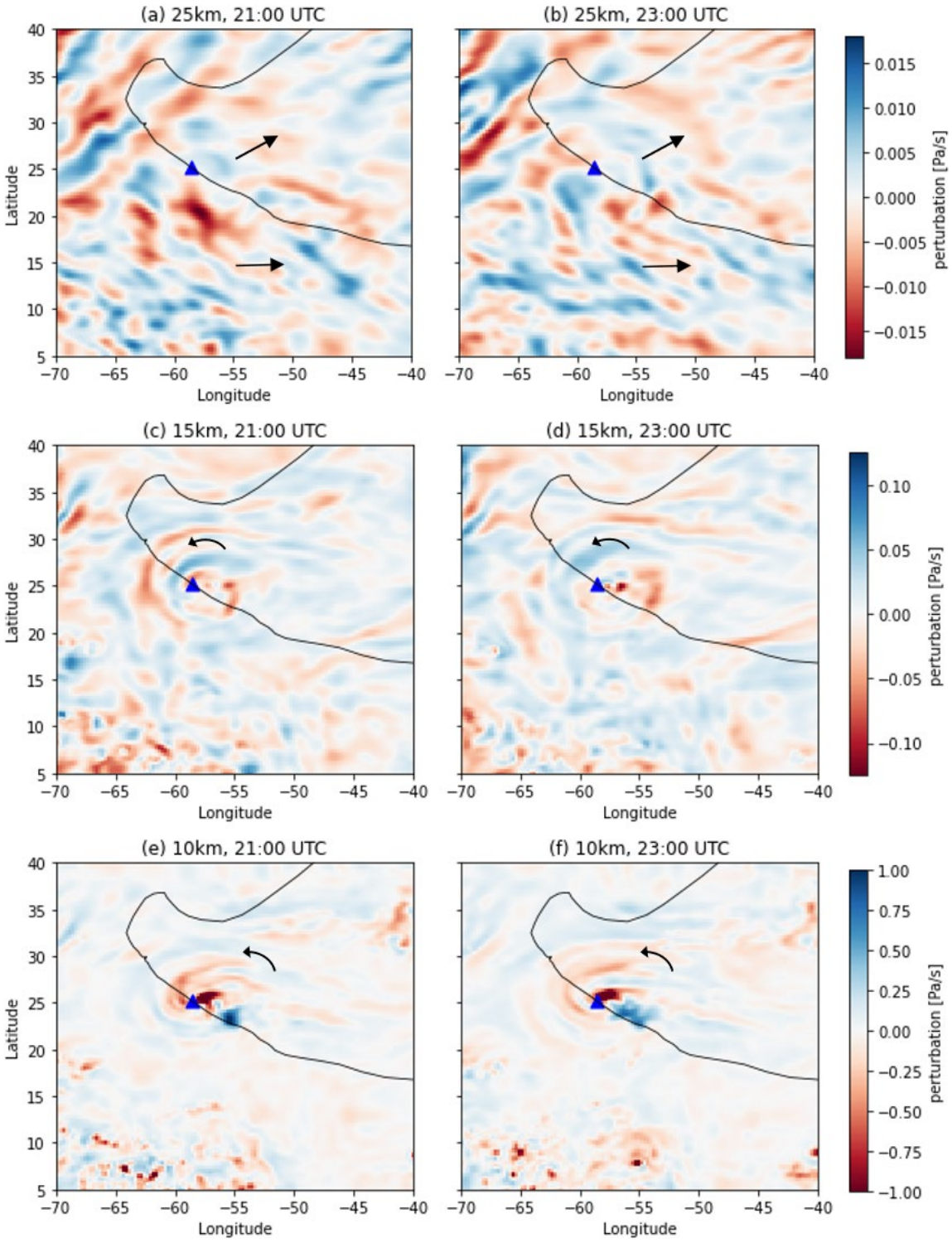

Figure 7.4. Vertical wind perturbation w' with the best track of Hurricane Bertha (black): (a)-(b) at 25km altitude, (c)-(d) at 15km altitude and (e)-(f) at 10km altitude. The blue triangle denotes the recorded eye location at 0:00h UTC on July 10 and the black arrows indicate the propagation direction of the GWs. Left and right columns are captured at 21:00h and 23:00h UTC on July 9, respectively.

In the lower stratosphere (Fig. 7.4a-b), the GWs generated by Bertha do not exhibit the concentric, striped structure or the radially spreading bands. Instead, the stratospheric GWs seem to propagate randomly at 25km altitude. This is possibly due to the weak overshooting convection inside the eyewall region, as we observed from the temperature perturbations. Consequently, there are few secondary waves (or almost none) being generated in the lower stratosphere.

In addition, the obstacle effect is also weak over the hurricane-disturbed region, since the background wind speed is the smallest in Bertha among all the hurricanes that we have studied (cf., Fig. 7.3a). Therefore, the GWs at 25km altitude are confirmed to be the primary waves that are generated in the upper troposphere, which propagate upward into the lower stratosphere and experience a decrease of the vertical wavelength.

Lastly, the maximum magnitude of the vertical wind perturbations drops from 1Pa/s to 0.018Pa/s from the upper troposphere to the lower stratosphere. This significant reduction demonstrates that the maximum GW intensity in the lower stratosphere is about 1.8% of that in the upper troposphere. Equivalently, the GW intensity attenuation is about 98.2% as the GWs cross the tropopause, which is the smallest among all the hurricanes we studied. This result is contrary to our expectation, since Bertha has the weakest temperature inversion and the intensity attenuation is expected to be the strongest among all the hurricanes (Stull, 1976).

Chapter 8

Comparison of Hurricane Thermodynamics and Gravity Wave Behaviours

In addition to the GW analyses of four hurricanes as individual case studies, we are also interested in studying the similarities and the variations of these GWs with respect to the hurricane intensity. In this chapter, we compare the thermodynamics in the UTLS region for different hurricanes and in different regions, aiming to show the variations of the GW behaviours when the hurricane intensity and the convection strength vary.

8.1 Hurricane intensity and eyewall temperature perturbations

The four hurricanes studied in the previous chapters are of different intensities, as characterized according to the Saffir-Simpson Hurricane Wind Scale. The hurricane intensity is a reflection of both the wind speed scale and the associated convection scale. As the convection and the background wind strengthen or weaken, the spectral properties of the hurricane-induced GWs vary with respect to the wave generation mechanisms and the GW dispersion relation.

One of our objectives in this thesis is to determine the variations of the GW properties as a function of the hurricane intensity. Accordingly, we carry out a comparison between the GWs that are induced by the four hurricanes of different intensities, which in decreasing order of intensity are Hurricane Dean (Category 5), Julia (Category 4), Bill (Category 4) and Bertha (Category 3). Bill is considered slightly weaker than Julia due to its small

sustained wind speed, as discussed in Chapter 6.

We want to point out that the GW variations observed among the different hurricanes of decreasing intensity are not equivalent to the variability of the GWs as the same hurricane weakens. Previous studies have examined the GW variation during the weakening (or intensification) of individual hurricanes (Kuester et al., 2008; Rogers et al., 2016; Wu et al., 2022), including their evolutions from a major hurricane stage to a tropical depression stage. Instead, our analysis is based on the comparison of the major hurricane stage for hurricanes with decreasing intensities. However, we think that our results can be used to roughly understand the weakening of a single hurricane and compare with the existing literature, as the deep convection and the sustained wind speed weaken in a similar way.

To study the GW variation between hurricanes of different intensities, we first compare the wave-induced temperature perturbations for selected hurricanes. Figure 8.1 presents the individual temperature profiles $T(z)$ selected inside the eyewall region of each hurricane, with their corresponding background temperature profiles $T_0(z)$. The background profiles for different hurricanes are almost identical, exhibiting a normal or undisturbed tropopause at about 16-17km altitude, as illustrated by the orange dashed line (Fig. 8.1). This result agrees well with the averaged altitude of tropopause in the tropics (Hoinka, 1999).

However, the background profiles of Bill and Bertha reveal a weak double-tropopause as discussed in Chapter 6 and 7 (cf., Fig. 8.1c-d). We consider the existence of this double-tropopause feature in the background profiles as an indication that the atmosphere is possibly already active in convection before the occurrence of the hurricane, which creates a favorable condition for the deep convection to initiate.

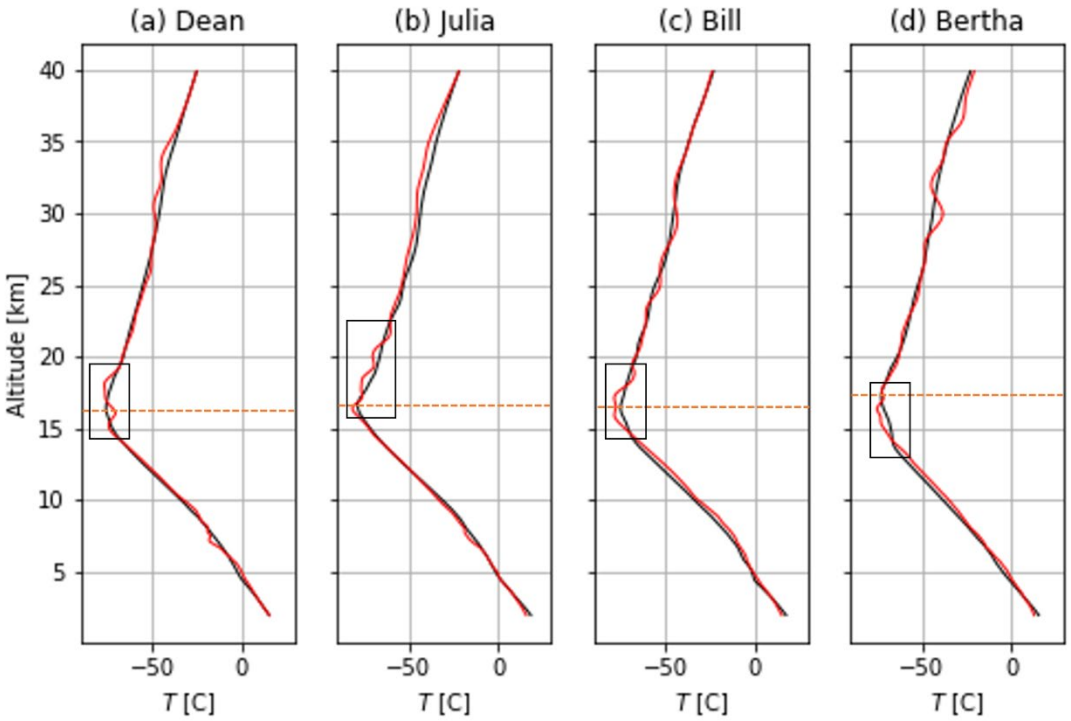

Figure 8.1. The background temperature profiles (black) and the individual temperature profiles (red) in the eyewall region of different hurricanes: (a) Dean, (b) Julia, (c) Bill and (d) Bertha. The normal tropopause level (orange dashed) for each hurricane is illustrated as well.

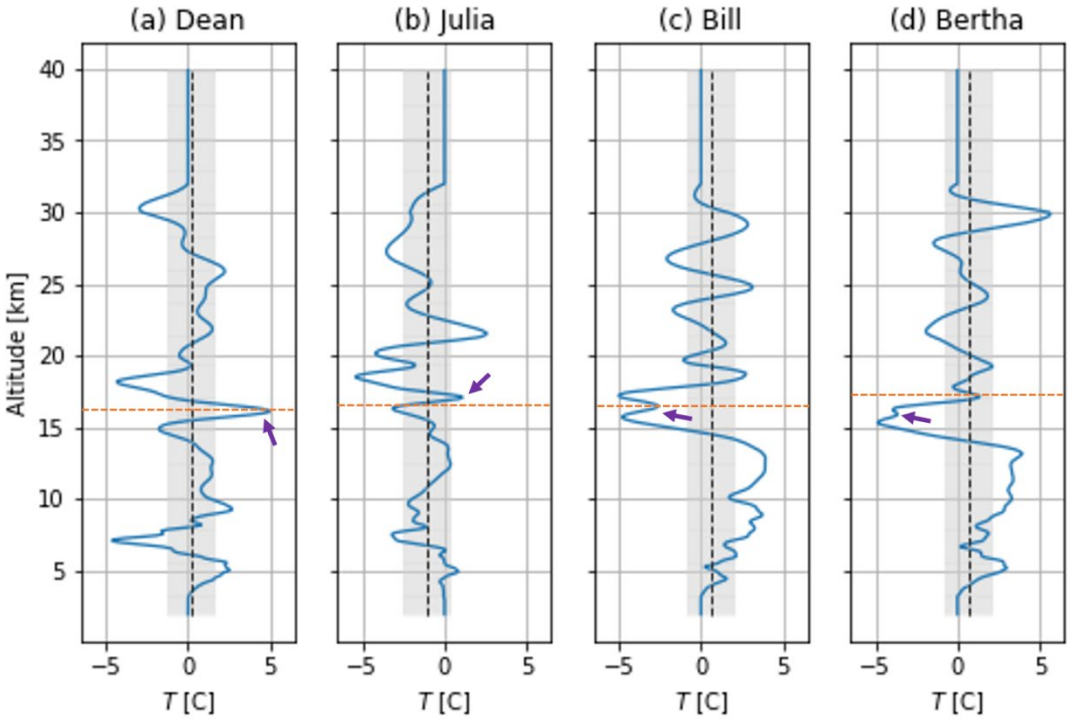

Figure 8.2. The temperature perturbation profiles (blue) in the eyewall region of different hurricanes: (a) Dean, (b) Julia, (c) Bill and (d) Bertha. The mean (black dashed), standard deviation (gray shaded) and the normal tropopause level (orange dashed) are also shown for each perturbation.

In addition, we notice strong temperature fluctuations around the tropopause level for all hurricanes (Fig. 8.1; shown inside the black frame). Figure 8.2 provides an enlarged view of these fluctuations, where temperature local minima and temperature inversions are observed. Compared to the normal tropopause level (Fig. 8.2; orange dashed), all the temperature inversions seem to occur about or above the tropopause (Fig. 8.2; indicated by purple arrows), except for Bertha. Furthermore, the inversion magnitude appears to decrease as hurricane intensity drops (Fig. 8.2; from left to right following the descending order of hurricane intensity).

Overshooting convection is suggested to occur when the strong temperature inversion caps the atmospheric boundary layer (Stull, 1976). Hence, the decrease of the inversion magnitude leads to a diminishing likelihood of the occurrence of overshooting convection, since there are less air parcels penetrating the tropopause (Hoffmann et al., 2018). This finding agrees with our conclusions stated in the previous chapter, as the overshooting convection was determined to be weak or absent for weak hurricanes like Bertha.

On the contrary, Julia reveals many fluctuations (ripples) above the tropopause with a temperature inversion that distinctly caps the boundary layer (Fig. 8.2b). This vertical structure guarantees the occurrence of the overshooting convection. As a result, we believe we have the best chances to observe the GWs generated by the overshooting convection in the eyewall region of Julia.

Aside from the temperature inversions, the negative temperature anomaly (around 7-8km altitude) appears to be the strongest in Dean, which gradually weakens as the hurricane intensity drops (Fig. 8.2b). This anomaly indicates that the boundary layer convergence, or the air inflow in the boundary layer is the strongest in Dean, suggesting a large buoyancy that can lift the warm air parcels upward and fuel the deep convection through the release of latent heat (Yano, 2021).

Hence, the weakening temperature anomaly indicates that the buoyancy at surface reduces as the hurricane intensity drops, leading to a less vigorous convective boundary layer as well as a less vigorous deep convection. In our opinion, this weakening trend is reasonable as it agrees with the descending order of the hurricane intensity and also verifies the physics that was used to explain the hurricane thermodynamics.

Alternatively, the temperature perturbations in the lower stratosphere seem to grow in magnitude as the hurricane intensity drops (cf., Fig. 8.2). For example, the stratospheric temperature perturbation of Dean appears to be the smallest, mostly falling within one standard deviation (Fig. 8.2a). For Bertha, the stratospheric perturbation becomes very notable and exceeds the standard deviation of the perturbation, especially at 30km altitude.

The intensifying stratospheric perturbation is possibly due to the variation of the dominating waves in the stratosphere. For Dean and Julia, the secondary waves dominate in the lower stratosphere; while for Bill and Bertha, we believe that the primary waves propagate upward into the stratosphere without being trapped (concluded in the previous chapters). Besides, the small-scale CGWs are likely to break or dissipate below the stratopause and deposit their energy to the background flow, which also creates significant disturbances in the atmospheric temperature (Xu et al., 2019).

It is interesting to find out that as the hurricane intensity drops, the temperature anomaly in the troposphere weakens while the stratospheric temperature perturbations intensify. The opposite variation in the convective layer below the tropopause and in the stable layer above the tropopause is a fresh finding, suggesting that the tropopause behaves as a critical layer and significant changes of the thermodynamics occur at this altitude.

8.2 Hurricane thermodynamics in the eyewall and rainband region

We have discussed the variations of the eyewall thermodynamics as the hurricane intensity drops. For a particular hurricane, the thermodynamics in the atmosphere, especially the convection, also varies with respect to the radial and azimuthal location relative to the hurricane center (Rogers et al., 2016). To further understand such variations, we carry out a comparison of the wave-induced temperature perturbations in the eyewall and the rainband region of each hurricane.

Table 8.1. A summary of the information for the RO temperature retrievals selected in the eyewall region and the rainband region for different hurricanes.

Name	Recorded time of the RO retrieval		Radial distance (km)	Azimuthal location
Dean	Eyewall	0:11 UTC, Aug. 18, 2007	87	Northeast
	Rainband region	0:27 UTC, Aug. 18, 2007	428	
Julia	Eyewall	16:45 UTC, Sept. 14, 2010	84	North
	Rainband region	5:26 UTC, Sept. 14, 2010	249	
Bill	Eyewall	13:35 UTC, Aug. 17, 2009	105	Southeast
	Rainband region	3:04 UTC, Aug. 17, 2009	522	
Bertha	Eyewall	14:19 UTC, July 8, 2008	36	Northeast
	Rainband region	23:05 UTC, July 8, 2008	596	

As introduced in Chapter 1, we refer to the outer region of a hurricane that comprises the convective rainbands as the rainband region. For each hurricane of our interest, we select a temperature retrieval in the rainband region on the same azimuth as the eyewall retrieval with a larger radial distance, as summarized in Table 1. The recorded time of each temperature retrieval and its radial distance from the eye are also reported.

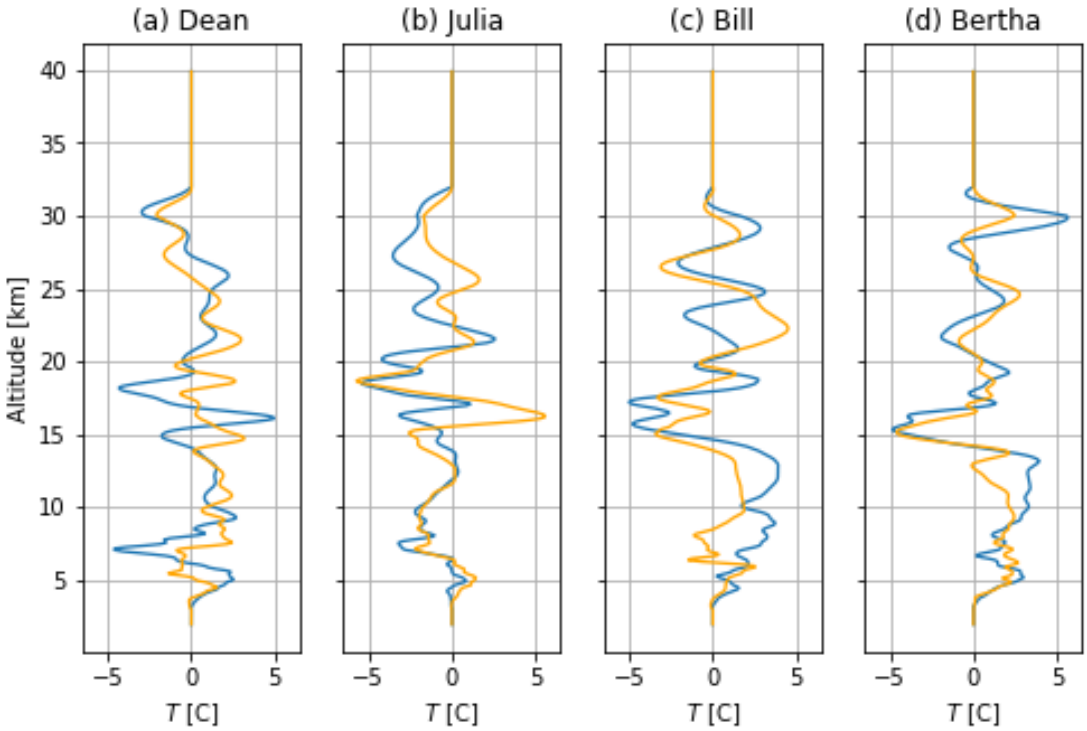

Figure 8.3. Comparisons of the windowed temperature perturbations induced in the eyewall (blue) and in the rainband region (orange) of different hurricanes: (a) Dean, (b) Julia, (c) Bill and (d) Bertha.

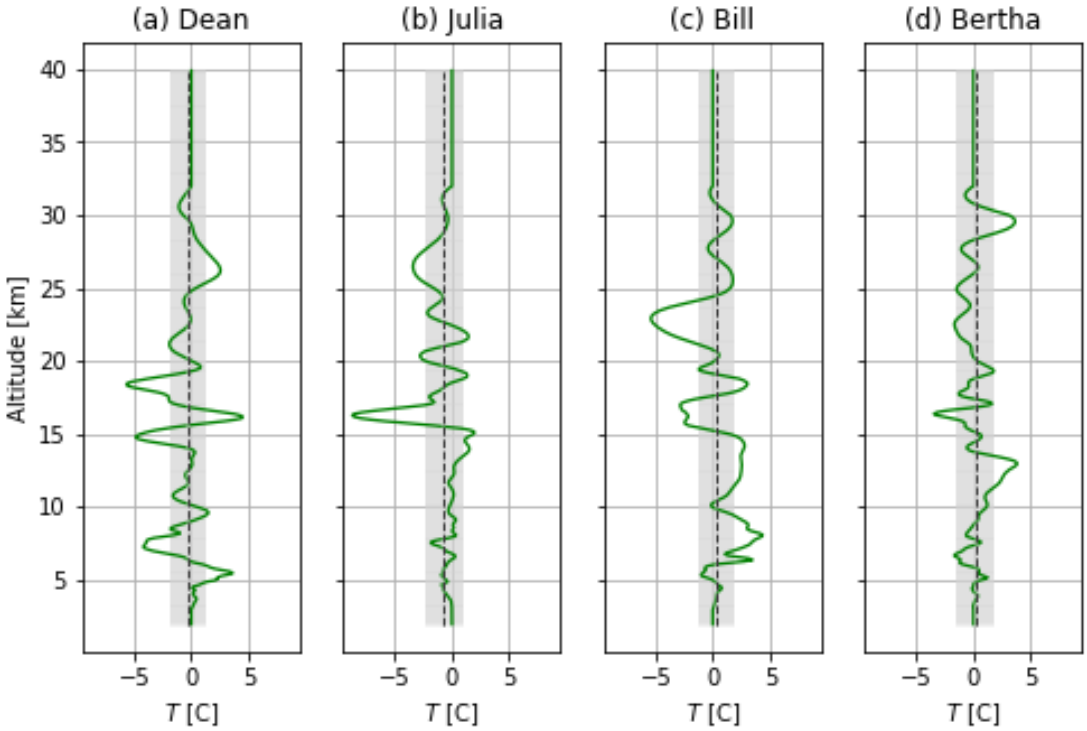

Figure 8.4. Differences of the windowed temperature perturbations (green) between eyewall and the rainband region of different hurricanes: (a) Dean, (b) Julia, (c) Bill and (d) Bertha. The mean (black dashed) and standard deviation (gray shaded) of each perturbation profile are also shown.

Figure 8.3 presents the comparisons of the wave-induced temperature perturbations that are extracted from the eyewall and the rainband region for each hurricane, in a descending order of hurricane intensity. Figure 8.4 further illustrates the difference between the temperature perturbations of each hurricane, with the calculation of its mean and the standard deviation.

For each hurricane, we find that the perturbation inside the rainband region reveal a very similar shape as in the eyewall, while discrepancies at various altitudes also exist (cf., Fig. 8.3). Specifically, we notice that the perturbations of Bertha are very similar (cf., Fig. 8.4d), since the perturbation difference mostly falls within one standard deviation; while the perturbations of Dean exhibit the most differences (cf., Fig. 8.4a), as the perturbation difference exceeds a magnitude of 5℃.

Hence, we believe that generally, the difference between the wave-induced temperature perturbations in the eyewall and the rainband region gradually reduce as the hurricane intensity drops, which has not been described in any previous studies. The decreasing difference is reasonable and agrees with our expectation, since the convection strength in the eyewall gradually reduces as the hurricane intensity drops, which becomes comparable to the convection in the rainband region.

In addition, Fig. 8.4 shows that the perturbation difference at the tropopause (15-20km) also weakens as the hurricane intensity decreases. It is noteworthy to point out that the perturbation difference of Julia even reaches a magnitude of -9℃ at the tropopause (cf., Fig. 8.4b). The variation at the tropopause is significant as it indicates the major difference between the eyewall and the rainband thermodynamics occurs at this altitude. This trend confirms our assumption that the tropopause behaves as a critical layer and further suggests that the tropopause behaviours vary with respect to the hurricane intensity.

Alternatively, Fig. 8.3 also reveals that the tropospheric temperature perturbations in the rainband region (orange profiles) is generally smaller in magnitude compared to those in the eyewall (blue profiles), which becomes very distinct for Bill and Bertha (cf., Fig 8.3c-d). This is likely a result of the less vigorous deep convection in the rainband region due to a larger radial distance from the eye, similar to the findings of Rogers et al. (2016).

Based on the analysis above, we make the conjecture that for a single hurricane, the thermodynamic states in the eyewall and the rainband region exhibit similar behaviour on the same azimuth, but reveals a decrease in the convection strength as the radial distance from the eye increases. It is outside the scope of this thesis to examine and discuss the time-variations of the thermodynamics in the atmosphere.

8.3 Gravity waves in the eyewall and rainband region

In addition to the variation of the thermodynamics in different regions of a hurricane, we also seek to determine the similarities and differences of the GW spectral properties in the eyewall and the rainband region. Figure 8.5 presents the least-squares spectra of the temperature perturbations extracted from the analyzed regions for each hurricane.

Similar to the temperature perturbations, the rainband region spectra (Fig. 8.5; orange spectra) exhibit very similar behaviour in terms of the vertical wavenumber and the wave power, as those in the eyewall (Fig. 8.5; blue spectra). Discrepancies between the spectra of each hurricane also exist, which weakens as the hurricane intensity drops. Specifically, the spectra of Dean reveal the largest difference between the eyewall and the rainband, as the dominating waves have different powers (Fig. 8.5a); while the spectra of Bertha are almost identical (Fig. 8.5g).

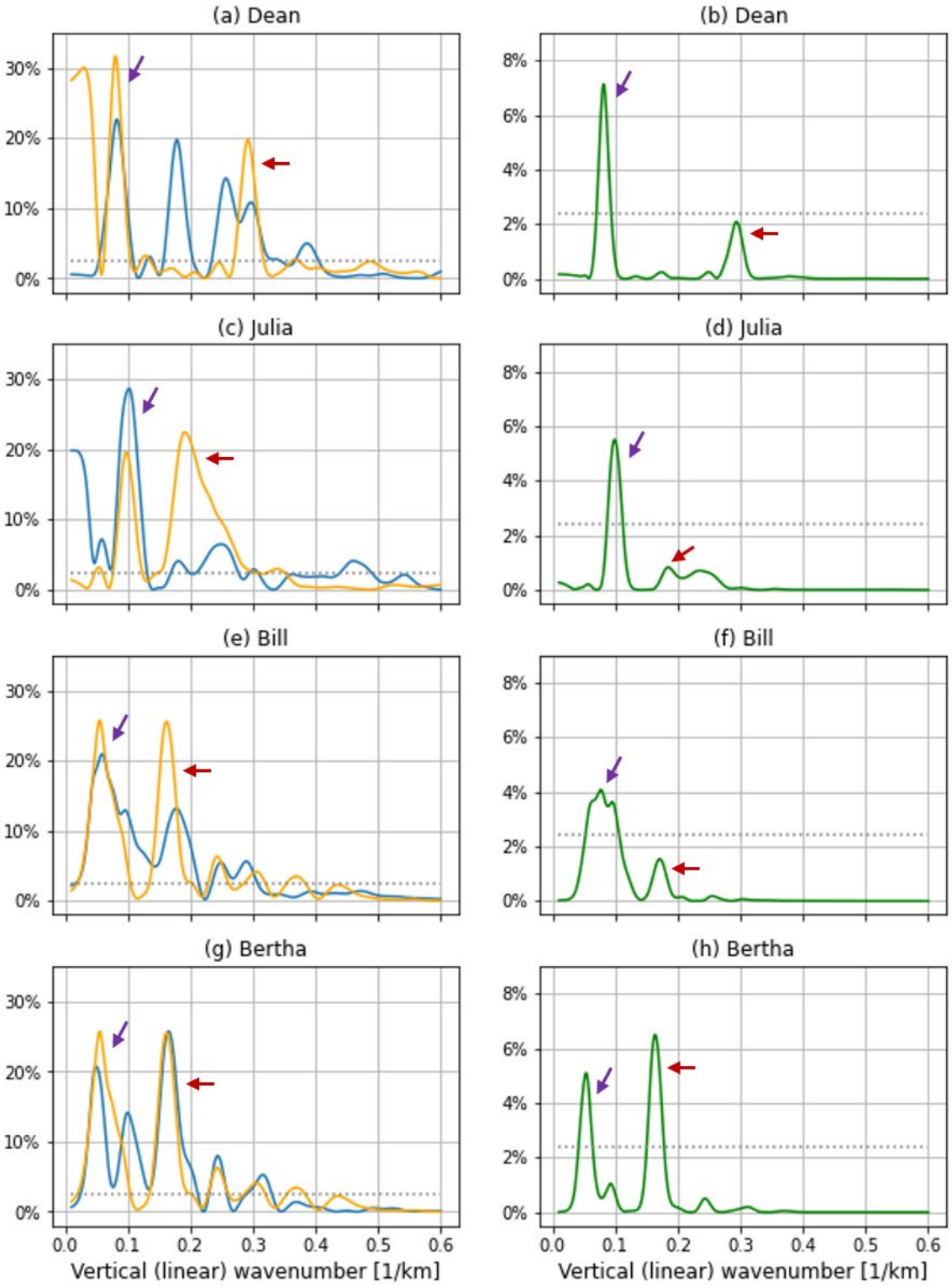

Figure 8.5. Comparisons of the least squares spectra for the windowed temperature perturbations in the eyewall (blue) and the rainband region (orange), as well as their spectra product (green) for different hurricanes: (a)-(b) Dean, (c)-(d) Julia, (e)-(f) Bill and (g)-(h) Bertha. The threshold of significance for each spectrum (gray dashed) at the 99% confidence level is also shown.

For all hurricanes, a small-wavenumber wave is observed in both the eyewall and the rainband region with a (linear) vertical wavenumber smaller than 0.1km^{-1} (Fig. 8.5; indicated by the purple arrows in the left column). These waves correspond to the primary waves that were observed in the spectrograms for each hurricane, which is considered to be induced by the pure thermal forcing mechanism. Besides, the power of this primary wave is slightly different in the eyewall and the rainband region for each hurricane, but usually achieves a percentage variance of 20% and above.

The spectra product in Fig. 8.5 further confirms that the primary wave corresponds to the pure thermal forcing generation, as it displays as a common peak in the spectra product (Fig. 8.5; indicated by the purple arrows in the right column), indicating that this wave exists in different regions with an identical wavenumber.

Apart from this primary wave, the spectra from the rainband region also present a significant peak with a relatively large wavenumber (Fig. 8.5; indicated by the red arrows in the left column), which also matches with a wave in the eyewall that shows as the common peak in the spectra product (Fig. 8.5; indicated by the red arrows in the right column). This secondary wave reveals a much larger power in the rainband region compared to the eyewall, which is sometimes the largest among all the waves in the rainband region.

This secondary wave has a wavenumber range about 0.1-0.3km^{-1} among different hurricanes, corresponding to a vertical wavelength of about 3.3-10km. The wave power of this secondary wave also reaches a value of 20%, which gradually increases as the hurricane intensity increases (Fig. 8.5; from bottom to top). We believe these secondary waves correspond to the dominating waves in the lower stratosphere in the convective region, as we will illustrate in the next chapter.

The dominance of these secondary waves in the rainband region is expected, since the stratospheric temperature perturbations are more notable as the hurricane intensity drops (cf., Fig. 8.2). Hence, we suggest that in the rainband region, the secondary waves are favored with an increasing power, while the primary waves remain almost unchanged compared to the eyewall. However, as mentioned earlier in Chapter 7 (e.g., Hurricane Bertha), when a hurricane is not intense, the primary waves that are not trapped below the tropopause also enter the lower stratosphere and contribute to the domination of the eastward-propagating waves.

8.4 Gravity wave intensity and wind perturbations

According to the wave-induced wind perturbations for each hurricane, the magnitude of the vertical wind perturbations decreases drastically from 10km to 25km altitude, which suggests that the GW intensity drops significantly from the upper troposphere to the lower stratosphere. Therefore, we are also interested in studying the variation of the GW intensity with respect to the hurricane intensity.

Table 8.2. A summary of the maximum magnitude of the vertical wind perturbations $w'(z)$ for different hurricanes. Maximum values are reported at 10km, 15km and 25km altitude in Pa/s.

Name	Recorded time of vertical air speed data from ERA5	Maximum magnitude of w' (Pa/s)			Intensity attenuation (%)
		10km	15km	25km	
Dean	0:00 UTC, Aug 18, 2007	3.0	0.20	0.04	98.7%
Julia	17:00 UTC, Sep 14, 2010	1.7	0.15	0.02	98.8%
Bill	13:00 UTC, Aug 17, 2009	2.5	0.13	0.03	98.8%
Bertha	21:00 UTC, Jul 9, 2008	1.0	0.13	0.01	99.0%

Table 2 reports the maximum magnitude of the vertical wind perturbation $w'(z)$ at three altitude levels (10km, 15km and 25km) for four hurricanes, with an estimation of the GW intensity attenuation from the upper troposphere to the lower stratosphere in percent. We aim to compare the strength of the GWs and the strength loss during the GW upward propagation when the hurricanes are of different intensities.

Based on the reported values in Table 1, at each altitude level, the maximum magnitude of $w'(z)$ is of the same scale for different hurricanes, justifying the rationale of this comparison that is, the GW intensity of different hurricanes is comparable. Furthermore, we notice that the maximum wind perturbation at each altitude generally decreases as hurricane intensity drops, except for Bill that does not fit the trend[25]. The decreasing perturbation magnitude demonstrates that the GW intensity seems to correlate positively to the hurricane intensity.

As far as we know, the decrease in the vertical wind perturbation with decreasing hurricane intensity has not been brought up by any previous studies. We think that as the hurricane intensity drops, the buoyancy at the surface reduces as we observe from the wave-induce temperature perturbations (cf., Fig. 8.2), resulting in the less intense updrafts in the hurricane-disturbed region. Accordingly, the upward propagation of the GWs also weaken, numerically shown as the decreasing magnitude of the vertical wind perturbations.

On the contrary, the intensity attenuation appears to increase as the hurricane intensity drops, except for Julia and Bill that report an equal attenuation of intensity. We believe that the decrease in the GW intensity is relevant to the energy loss experienced by the GWs during their vertical propagations. As stated by Stull (1976), the drastic drop in the wind perturbation magnitude is a reflection of the GW energy loss in the turbulent layer as

[25] We consider Bill as an anomaly since we assumed Bill is slightly weaker than Julia based on the sustained wind speed.

the GWs propagate upward across the tropopause. The upward energy propagation is disturbed either being trapped by the temperature inversion, or is reflected back and being absorbed by the turbulent layer. The energy loss becomes significant if the temperature inversion is weak and the turbulent layer is vigorous (Stull, 1976).

We observed that the temperature inversion at the tropopause altitude becomes weaker as the hurricane intensity drops (cf., Fig. 8.1), suggesting that the GW energy loss becomes more significant according to Stull (1976). This increasing energy loss corresponds to an increasing intensity attenuation of the GWs as reported in Table 2, although the increase is very small and can be considered as almost constant (about 99.0%).

Therefore, we confirm that during the upward propagation of the GWs, the GW intensity attenuation positively correlates to the GW energy loss, while the exact correlation needs to be determined by further studies. This finding numerically verifies the theoretical simulation brought up by Stull (1976), although we expect a more significant variation of the GW energy loss (or intensity attenuation) as the hurricane intensity varies.

Moreover, based on the previous discussions, the attenuation of the temperature inversion also suggests that the overshooting convection is not likely to occur. Hence, we propose for the first time that the GW intensity attenuation though their upward propagation is small when the overshooting convection is intense and the temperature inversion is strong (e.g., for strong hurricanes).

Chapter 9

Comparison of Gravity Wave Variability and Wave Generation Mechanisms

We have discussed the GW characteristics for different hurricanes and in different regions of a hurricane, in terms of hurricane thermodynamics as well as the GW spectral properties. In this chapter, we present a similar comparison but using the spectrograms, in order to illustrate the GW variability during their upward propagation according to the wave generation and dissipation mechanisms.

9.1 Gravity wave variability in the eyewall region

In the individual hurricane case studies, several wave generation and wave dissipation mechanisms were suggested for the GW vertical variations. Primary waves and secondary waves were identified with respect to the dominating mechanisms at different altitude levels, which exhibited various characteristics in different hurricanes. Here, we are interested in studying the variability of these dominating mechanisms and their effects on the GWs as the hurricane intensity varies.

To visually illustrate the vertical variations of the GWs that are induced by the different hurricanes during their upward propagations, Fig. 9.1 presents the spectrograms of the wave-induced temperature perturbations that are extracted from the eyewall region of each hurricane, with an estimated tropopause level.

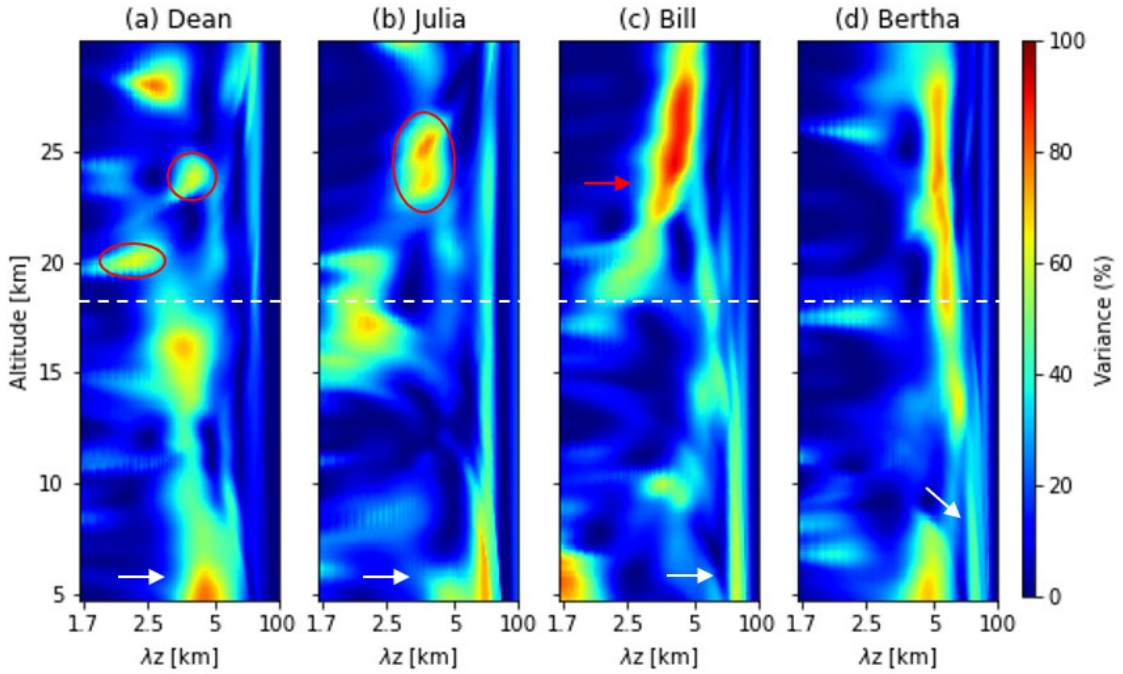

Figure 9.1. Normalized least squares wavelet spectrograms of the windowed temperature perturbation $T'(z)$ inside the eyewall of different hurricanes: (a) Dean, (b) Julia, (c) Bill and (d) Bertha. The estimated tropopause level (white dashed) is also shown.

According to Gettelman et al. (2002), the tropopause in the tropical region is in fact a transition zone that usually extends from the main convective outflow (about 12km altitude) to the cloud top (about 17km altitude). Considering the large latent heat release that deepens the convective boundary layer during the hurricanes, we determine the maximum tropopause altitude as 18-19km altitude under the presence of deep convection (cf., Fig. 9.1; illustrated as the white dashed line), which is slightly higher than the normal tropopause altitude of 16-17km, as illustrated in Fig. 8.1.

For all hurricanes, we observe the long-wavelength, high-frequency primary waves at the surface level (Fig. 9.1; denoted by the white arrows) that are generated by the pure thermal forcing mechanisms (Fritts & Alexander, 2003). The primary waves exhibit a large vertical wavelength range of $\lambda_z \approx$ 3-20km for different hurricanes. Specifically, the primary wave of Dean reveals a relatively short wavelength (Fig. 9.1a; $\lambda_z \approx$ 3-7km), while the primary wave of Bill shows the longest wavelength (Fig. 9.1c; $\lambda_z \approx$ 11-20km).

Aside from the primary waves, we notice a few secondary waves in Dean and Julia above 20km altitude that are distinct from the primary waves in the troposphere (Fig. 9.1a-b; circled by red). The secondary waves in the lower stratosphere seem to prevail in Julia compared to Dean. Overshooting convection is considered to be the source of these small-scale secondary waves, when the 'hot-tower' structure penetrates the tropopause for strong hurricanes (Stull, 1976; Hoffmann et al., 2018).

Subject to the horizontal propagation direction of the GWs as well as the direction of the horizontal background wind, the upward propagating waves possibly experience the background wind filtering (Mukherjee et al., 2010). For Dean and Julia, we observe a decrease in the GW vertical wavelength for the primary waves (Fig. 9.1a-b), since these waves propagate in a similar horizontal direction as the background wind. The decrease in the GW vertical wavelength is the strongest in Julia, indicating that critical level filtering occurs which traps the primary wave at about 19km altitude (Cowling et al., 1971).

In contrast, the stratospheric GWs of Bill experience an increase in the vertical wavelength with a growing power (Fig. 9.1c; denoted by the red arrow), since the GWs propagate in opposite direction to the westward horizontal background wind. We believe that the obstacle effect that is usually dominant above the tropopause also contributes to the stratospheric waves that grow in power, as the obstacle effect generates the eastward-propagating waves when the westward wind is present (Dutta et al., 2009).

The primary waves of Bertha do not reveal any significant shifts of wavelength (Fig. 9.1d), since the trapping of the primary waves is very weak in Bertha due to the small background wind speed. Similar to Bill, the obstacle effect is suggested to be responsible for the increasing power for the GWs, given a background wind speed increases with altitude.

Based on the discussion above, we think that the pure thermal forcing generates the GWs in an almost identical way in all hurricanes, which is the major wave-generating mechanism at the surface level. Besides, we believe that the likelihood of the overshooting convection occurrence reduces as the hurricane intensity drops, since the small-scale secondary waves are only observed in Dean and Julia.

In Fig. 9.1, we also notice that the primary waves in the troposphere reveal large power in hurricanes with large intensity (e.g., Dean and Julia), which seems to decrease as the hurricane intensity drops. On the other hand, the stratospheric waves above the estimated tropopause display large power in hurricanes with small intensity (e.g., Bill and Bertha). We believe these GW variations are due to the different dominating mechanisms.

The background wind filtering and the critical level filtering effects attenuate as the hurricane intensity drops that is, the trapping of the primary waves becomes weak, allowing the primary waves to propagate upward and enter the lower stratosphere without being shifted towards short vertical wavelength or low intrinsic frequency. Secondly, the obstacle effect is suggested to prevail in the upper troposphere and above for hurricanes with small intensity, which contributes to the dominance of the secondary waves as we observe in the vertical wind perturbation results.

Hence, we believe that in intense hurricanes, the generation and the trapping of the primary waves leads to a large wave power in the troposphere, as a result of both the pure thermal forcing mechanism and the wind filtering effects. As the hurricane intensity decreases, the primary waves are not trapped below the tropopause and the secondary waves generated by the obstacle effect start to dominate, therefore displaying a large power in the stratosphere.

We think that the comparison of the GW vertical propagations in the eyewall of different hurricanes is a unique contribution to the studies of the hurricane-induced GWs. We provide not only the visual illustration of the GW wavelength variation, but also the wave variation as a function of the hurricane intensity, which have not been accomplished before.

9.2 Gravity wave variability in the rainband region

In addition to the GW variability in the eyewall region as the hurricane intensity varies, we also investigate the GW variability in the rainband region where both the deep convection and the horizontal background wind weaken. To illustrate the variation of the GW characteristics, we present the spectrograms of the temperature perturbations that are extracted from the rainband region for all hurricanes in Fig. 9.2.

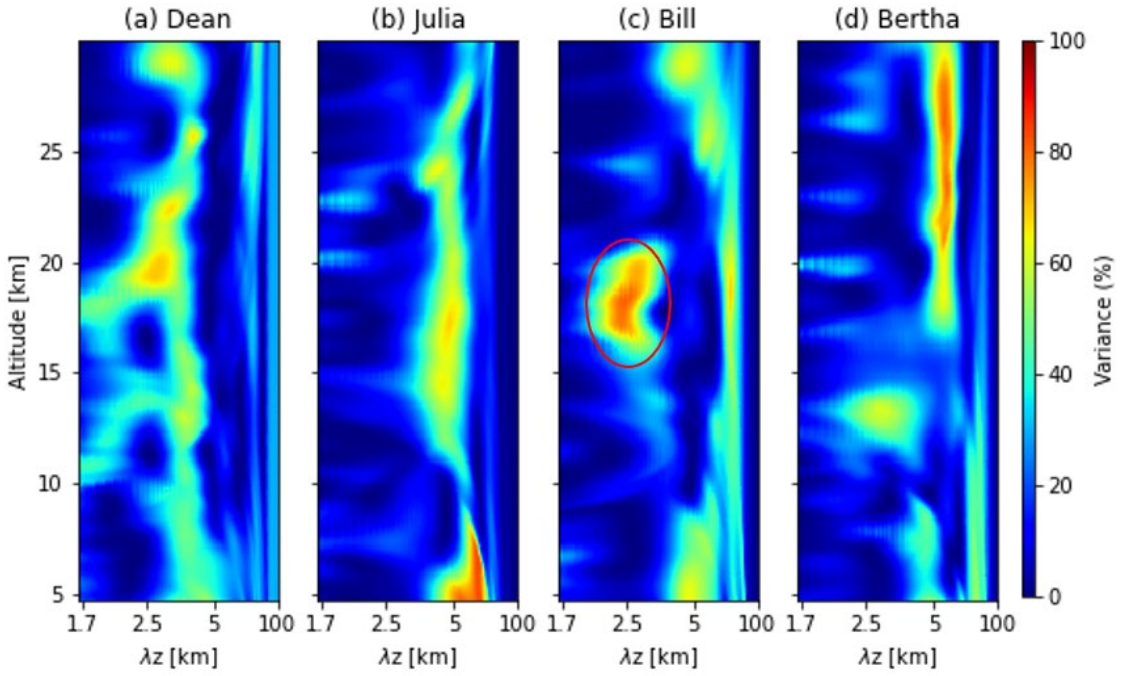

Figure 9.2. Normalized least squares wavelet spectrograms of the windowed temperature perturbation $T'(z)$ in the rainband region of different hurricanes: (a) Dean, (b) Julia, (c) Bill and (d) Bertha. The estimated tropopause level (white dashed) is also shown.

A consistent vertical propagation structure of the GWs is observed, where the primary waves generated by the pure thermal forcing at the surface propagate straight upward and enter the stratosphere (cf., Fig. 9.2). Although some small gaps and slight variations are present along the vertical GW propagation, most of the GWs present a continuous upward path without any significant shifts in the vertical wavelength.

The consistent structure in Fig. 9.2 demonstrates that the GWs in the rainband region are not modified much by the background wind. Compared to the eyewall region, the horizontal wind is much weaker in the rainbands and the background wind filtering effect weakens accordingly. As a result, the GW vertical wavelength remains almost constant during the GW upward propagation in the rainbands.

Nevertheless, each hurricane exhibits different transitions of the GW propagation from the eyewall to the rainband region by examining the difference between Fig. 9.1 and Fig. 9.2. Specifically, Dean and Julia reveal a strong trapping of the primary waves in the eyewall due to the wind-filtering effect (Fig. 9.1a-b), which is not present in the rainband region (Fig. 9.2a-b). The small-scale secondary waves generated by the overshooting convection in the eyewall of Dean and Julia do not appear in the rainband region either.

Similarly, Bill presents strong stratospheric waves inside the eyewall region (Fig. 9.1c) with an increasing vertical wavelength due to the background wind filtering. However, in the convective region, a primary wave with a vertical wavelength of $\lambda_z \approx$ 20km is present at all altitudes (Fig. 9.2c). In addition, Bill reveals a unique wave component at 15-20km altitude in the rainband region (Fig. 9.2c; circled by red) that does not appear in the eyewall. We think that this secondary wave possibly contributes to the dominance of the stratospheric waves, since this wave is likely a result of the obstacle effect. This result suggests that the obstacle effect exists in both the eyewall and the rainband region of Bill.

Interestingly, the spectrograms in the eyewall and the rainband region of Bertha are very similar. This similarity suggests that the thermodynamics in the atmosphere of Bertha does not vary much at different radial distances.

Based on the discussion above, we conclude that the background wind filtering effect significantly weakens in the rainband region of a hurricane, where the trapping of the primary waves and the excitation of the secondary waves attenuates as the radial distance increases. In addition, on the same azimuth, the GW propagation varies significantly with the radial distance for intense hurricanes, which seem to maintain a consistent pattern for less intense hurricanes.

9.3 Two-layer convection and wave generation mechanism effects

According to the discussion on the GW characteristics as well as their variations with respect to the hurricane intensity, we believe that the critical variations in the vertical propagation of the GWs occur in the transition layer between the convective layer and the stable layer that is, the tropopause. In recent studies, the tropopause is sometimes referred to as the *tropopause transition layer* (TTL) that exhibits properties of both the troposphere and the stratosphere (Ryu & Lee, 2010).

Specifically, the temperature inversion around the tropopause is crucial in determining the occurrence of the overshooting convection. The tropopause also appears to be an inter-layer that traps the primary waves below and excites the secondary waves above. Furthermore, as the hurricane intensity drops, the variation of the tropospheric GWs seems opposite to the stratospheric wave variation.

Hence, we consider the convection in the UTLS region of a hurricane as a two-layer convection, which is illustrated in Fig. 9.3. The two-layer convection model is composed

of an unstable layer at the bottom and a stable layer at the top, which simulate the convective troposphere and the steady stratosphere in the hurricane-disturbed region, respectively. These two layers are separated by a transition layer, namely the tropopause, which plays a key role in the two-layer convection (cf., Fig. 9.3).

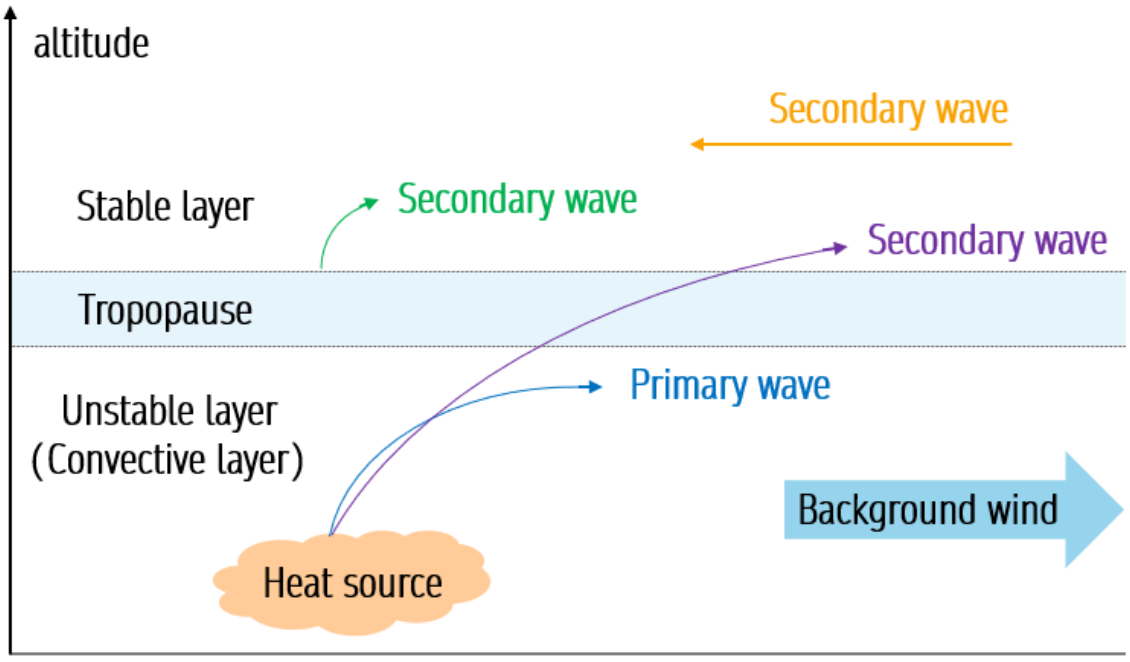

Figure 9.3. Diagram of two-layer convection that simulates the convective regime of hurricanes.

A heat source located in the unstable layer is considered to represent the thermal forcing that localizes the convective storms. The heat source is assumed to generate the primary waves (Fig. 9.3; blue arrow) that dominate at a close radial distance from the thermal forcing and can be observed in the unstable layer. In addition, the heat source is also considered to produce secondary waves (Fig. 9.3; purple arrow) that dominate at a further distance and are easy to observe in the stable layer (Alexander & Holton, 2004; Nolan, 2020).

According to the wave generation mechanisms introduced in Chapter 2, we assume that the heat source in the unstable layer generates the GWs through the pure thermal forcing

mechanism. In addition, we consider that the hurricane-induced GWs propagate vertically upward in both layers depending on the wind conditions, following the mathematical two-layer model proposed by Sayed (2014).

Specifically, the upward propagating GWs experience the background wind filtering if they propagate in a similar (opposite) horizontal direction to the background wind, leading to the decrease (increase) of the vertical wavelength and intrinsic frequency (Mukherjee et al., 2010). When a strong horizontal wind is present, the GWs are trapped at their critical level and eventually dissipate (Cowling et al., 1971). Figure 9.3 briefly illustrates the trapping of the primary waves given the direction of the horizontal background wind.

Alternatively, overshooting convection exists when the temperature inversion caps the convective boundary layer, which also excites the secondary waves (Fig. 9.3; green arrow) in the stable layer above the tropopause. Similarly, the obstacle effect produces the GWs that propagate in the opposite direction to the background wind, when the strong stratospheric wind is present. These mechanisms usually contribute to the domination of the secondary waves in the stable layer.

Hence, we think that the transition layer mainly serves two purposes. Firstly, when the GWs propagate upward from the surface (cf., Fig. 9.3), the tropopause acts as a low-pass filter and traps the primary waves in the unstable layer below via the background wind filtering and the critical level filtering. Secondly, the tropopause also behaves as a boundary layer at the base of the stable layer, which excites the small-scale secondary waves through the overshooting convection and possibly the obstacle effect as well.

As introduced above, the two-layer convection is suitable for simulating the convection regime of the hurricanes, as it connects the wave generation mechanisms in the UTLS region to describe the GW generation. Moreover, the two-layer convection is also valid for

simulating hurricanes of different intensities. As the hurricane intensity drops, the tropopause becomes less active in trapping the primary waves, but more vigorous in exciting the secondary waves in the stable layer.

Chapter 10

Conclusions

10.1 Summary

This chapter concludes our analyses of the small-scale gravity waves (GWs) that are generated by the hurricanes in the upper troposphere and the lower stratosphere (UTLS) region. Specifically, we carried out the investigation using the high vertical resolution temperature retrievals from the GPS-RO technique and the fine horizontal resolution wind data from the ERA5 dataset. Four hurricanes of different intensities were selected namely, Hurricane Dean (category 5), Julia (category 4), Bill (category 4) and Bertha (category 3).

We first presented the thermodynamics and the GW characteristics in the eyewall region. The double-tropopause feature was observed with a temperature inversion around the undisturbed tropopause altitude, which we considered as a favorable condition for the occurrence of the overshooting convection. This result verifies the finding of Vergados et al. (2014) who also used the GPS-RO temperature retrievals to study the eyewall thermodynamics of different hurricanes.

For the first time, via the wavelet analysis, we observed the primary waves that are likely generated by the pure thermal forcing mechanism. We also confirmed the generation of the secondary waves that justifies the theoretical assumption of Stull (1976) regarding the vertically propagating GWs produced by the overshooting convection. These findings are innovative because for the first time, they connect our analytical results with the

conceptual mechanisms that are widely accepted for the GW generation (Beres et al., 2002; Kuester et al., 2008).

In addition, using the wavelet analysis, we uniquely provided the observational evidence that verifies the concept of the background wind filtering (Cowling et al., 1971; Mukherjee et al., 2010) that is, the GW vertical wavelength decreases for Dean and Julia while the stratospheric GW wavelength increases for Bill. Similarly, we demonstrated the critical level filtering where the primary wave generated by Julia was shifted towards a shorter vertical wavelength and was eventually trapped below 20km altitude.

To the best of our knowledge, such illustrations have not been accomplished before. We think that it was imperative and convincing to demonstrate the GW wavelength variability with respect to the ambient background wind during the GW vertical propagation, more so than simply comparing the GW properties at different altitude levels as presented in previous studies.

Based on the wave-induced wind perturbations, we observed a spiral propagation of the GWs in the troposphere for all hurricanes, which transited into a concentric ring structure in the lower stratosphere. Our finding verified the modeled simulation of the GW spiral propagation for Hurricane Joaquin (Wu et al., 2022) as well as the observational results of the concentric GWs for Hurricane Matthew using the Aqua satellite measurements (Xu et al., 2019).

We also noticed a dominance of the eastward-propagating GWs in the lower stratosphere for most hurricanes as a consequence of both the background wind filtering and the obstacle effect. This anisotropic wave field agreed well with previous studies, such as Kim and Chun (2010) who observed a similar GW asymmetry for Typhoon Saomai (2006) using numerical simulations.

We found a significant intensity attenuation of the GWs (about 99% as almost constant) for all hurricanes during the GW upward propagation that positively correlates to the GW energy loss, justifying the numerical results presented in previous studies using Lidar measurements (Zhao et al., 2022) and mathematical modeling (Stull, 1976). The estimated GW intensity for different hurricanes also provided observational evidence that verifies the strong correlation between the GW intensity and the hurricane intensity, as suggested by Wu et al. (2022) through model simulations.

We studied the variation of the thermodynamics and the GW characteristics in different regions of a hurricane. The temperature perturbations exhibit similar characteristics along the same azimuth in the eyewall and the rainband region, while the perturbation magnitude decreases with the radial distance. This result confirms the effects of the deep convection distribution on hurricane intensity (Rogers et al., 2016) and further hypothesizes the variability of the convection along the radial and azimuthal directions, which is described for the first time.

For each selected hurricane, we found that the eyewall and the rainband region reveal a common primary wave ($\lambda_z \approx$ 3-20km) that usually dominates in the eyewall. In contrast, the smaller-scale secondary wave seems to prevail in the rainband region ($\lambda_z \approx$ 3.3-10km) that propagates straight upward without been trapped. Our observation here is original and precisely interprets the physics of the hurricane thermodynamics.

We continued our analysis by examining the GW behaviours as the hurricane intensity drops. We found that the pure thermal forcing mechanism seems almost identical in generating the primary waves for different hurricanes, but the likelihood of the overshooting convection occurrence diminishes in weak hurricanes. In addition, the wind-filtering effect appears to weaken as the hurricane intensity drops, which allows the

primary waves to propagate upward and enter the stratosphere. Alternatively, the obstacle effect seems to prevail in the lower stratosphere regardless of the hurricane intensity.

The variability of the GW generation and dissipation mechanisms with hurricane intensity is a major contribution of this work that differs from the similar studies. We inventively identify the distinct GW types (Alexander & Holton, 2004) with respect to their wave generation mechanisms, which overcomes the difficulties of distinguishing the GWs due to their varying intrinsic frequency and spectral properties. The combination of the diverse GW theories also helps to establish the missing link between the wave generation or modification mechanisms with the observed wave properties.

We considered a two-layer convection model to simulate the convective regime of a hurricane, similar to the mathematical model proposed by Sayed (2014). We believe that the tropopause acts as a transition layer in this conceptual model, which traps the primary waves at the bottom of the unstable layer and excites the secondary waves in the overlying stable layer. The two-layer convection is still valid as the hurricane intensity drops, while the trapping and the excitation of the GWs weaken accordingly.

Through a series of analyses and comparisons, we identified and described the GW characteristics and their variations in hurricanes of different intensities. Our findings were based on the numerical or the observational results, which verified a number of theories that were heuristically concluded by the previous studies. We believe that the high vertical resolution RO temperature retrievals and the tropopause behaviour are key to solve for the small-scale GWs in the UTLS region. Lastly, we hope this work can contribute to filling the gaps that exist in the current studies of the GWs and the hurricanes.

10.2 Future work

Recent research has shown a rising interest in the small-scale GWs that are generated via convection. The discussion in Chapter 2 also demonstrated a number of limitations for the CGW parametrization as well as the GW source identification. More studies in these areas are needed to better understand the coupling between the CGWs and the atmosphere.

Specifically, the estimation of the GW intrinsic frequency using the GW linearized theory is required to study the CGW variability and to accurately justify the wind filtering theory (Fritts & Alexander, 2003). The asymmetric distribution of the diabatic heating and the background wind shear is not fully understood yet, which introduces complicities in the CGW parametrization (Choi et al., 2009; Kim & Chun, 2010). Furthermore, the analysis of the vertical wind perturbation in a time-evolving model is needed to solve the time variability of the CGWs with respect to the fast-developing background environment.

Moreover, the dynamics that modify the GWs at the tropopause level need to be further studied and clarified, since the GW variations in this transition zone are significant. This coupling helps to understand the breaking and the dissipation of the GWs, which possibly also lead us to a detailed interpretation for the GW activities in the upper atmosphere (Hung & Kuo, 1978).

Bibliography

[1] Alexander, Holton, J. R., & Durran, D. R. (1995). The gravity wave response above deep convection in a squall line simulation. *J. Atmos. Sci.,* **52(12)**, 2212–2226.

[2] Alexander, & Holton, J. R. (2004). On the spectrum of vertically propagating gravity waves generated by a transient heat source. *Atmos. Chem. Phys.,* **4(4)**, 923–932.

[3] Ao, Hajj, G. A., Meehan, T. K., Dong, D., Iijima, B. A., Mannucci, A. J., & Kursinski, E. R. (2009). Rising and setting GPS occultations by use of open-loop tracking. *J. Geophys. Res. Atmos.,* **114(D4)**, D04101–n/a.

[4] Aragão, & Porcù, F. (2022). Cyclonic activity in the Mediterranean region from a high-resolution perspective using ECMWF ERA5 dataset. *Clim. Dyn.,* **58(5-6)***,* 1293–1310.

[5] Avila, L. A. (2009, October 21). Tropical Cyclone Report Hurricane Bill.

[6] Beres, Alexander, M. J., & Holton, J. R. (2002). Effects of tropospheric wind shear on the spectrum of convectively generated gravity waves. *J. Atmos. Sci.,* **59(11)**, 1805–1824.

[7] Beres, Alexander, M. J., & Holton, J. R. (2004). A method of specifying the gravity wave spectrum above convection based on latent heating properties and background wind. *J. Atmos. Sci.,* **61(3)**, 324–337.

[8] Beven II, & Landsea, C.W., (2010, December 9). Tropical Cyclone Report Hurricane Julia.

[9] Chartier. (2005). *Introduction to Optics* (1st ed. 2005.). Springer New York.

[10] Chen, Chen, Z., & Lü, D. (2012). Simulation of the stratospheric gravity waves generated by the Typhoon Matsa in 2005. *Sci. China. Earth Sci.,* **55(4),** 602–610.

[11] Choi, Chun, H.-Y., Gong, J., & Wu, D. L. (2012). Comparison of gravity wave temperature variances from ray-based spectral parameterization of convective gravity wave drag with AIRS observations. *J. Geophys. Res. Atmos.,* **117(D5)**.

[12] Choi, Chun, H.-Y., & Song, I.-S. (2009). Gravity wave temperature variance calculated using the ray-based spectral parameterization of convective gravity waves and its comparison with Microwave Limb Sounder observations. *J. Geophys. Res.*, **114(D8)**, D08111–n/a.

[13] Clark, T. L., Hauf, T., & Kuettner, J. P. (1986). Convectively forced internal gravity waves: Results from two-dimensional numerical experiments. *Q. J. R. Meteorol.*, **112(474)**, 899 –925.

[14] COSMIC Project Office. (2005). *Variational Atmospheric Retrieval Scheme (VARS) for GPS Radio Occultation Data.* University Corporation for Atmospheric Research.

[15] Cowling, Webb, H. D., & Yeh, K. C. (1971). Group rays of internal gravity waves in a wind-stratified atmosphere. *J. Geophys. Res.*, **76(1)**, 213–220.

[16] Davis. (2018). Resolving tropical cyclone intensity in models. *Geophys. Res. Lett.,* **45**, 2082–2087.

[17] Davison, M. (1999). *Shallow/Deep Convection* [PowerPoint Slides]. National Centers for Environmental Prediction.

[18] DeHart, Houze, R. A., & Rogers, R. F. (2014). Quadrant Distribution of Tropical Cyclone Inner-Core Kinematics in Relation to Environmental Shear. *J. Atmos. Sci.,* **71(7)**, 2713–2732.

[19] Dutta, Ajay Kumar, M. C., Vinay Kumar, P., Venkat Ratnam, M., Chandrashekar, M., Shibagaki, Y., Salauddin, M., & Basha, H. A. (2009). Characteristics of high-frequency gravity waves generated by tropical deep convection: Case studies. *J. Geophys. Res.*, **114(D18)**, D18109–n/a.

[20] Ehard, Kaifler, B., Kaifler, N., & Rapp, M. (2015). Evaluation of methods for gravity wave extraction from middle-atmospheric lidar temperature measurements. *Atmos. Meas. Tech.,* **8(11)**, 4645–4655.

[21] Eichinger, Garny, H., Šácha, P., Danker, J., Dietmüller, S., & Oberländer-Hayn, S. (2020). Effects of missing gravity waves on stratospheric dynamics; part 1: climatology. *Clim. Dyn.,* **54(5-6)**, 3165–3183.

[22] Emanuel. (1986). An Air-Sea Interaction Theory for Tropical Cyclones. Part I: Steady-State Maintenance. *J. Atmos. Sci.,* **43(6)**, 585–605.

[23] Emanuel, Ravela, S., Vivant, E., & Risi, C. (2006). A statistical deterministic approach to hurricane risk assessment. *Bulletin of the American Meteorological Society*, **87(3)**, 299–314.

[24] Foelsche, Borsche, M., Steiner, A. K., Gobiet, A., Pirscher, B., Kirchengast, G., Wickert, J., & Schmidt, T. (2008). Observing upper troposphere-lower stratosphere climate with radio occultation data from the CHAMP satellite. *Clim. Dyn.,* **31(1)**, 49–65.

[25] Fovell, Durran, D., & Holton, J. R. (1992). Numerical simulations of convectively generated stratospheric gravity waves. *J. Atmos. Sci.,* **49(16 A)**, 1427–1442.

[26] Franklin, J. (2008, April 7). Tropical Cyclone Report Hurricane Dean.

[27] Fritts, & Alexander, M. J. (2003). Gravity wave dynamics and effects in the middle atmosphere. *Rev. Geophys (1985)*, **41(1)**, 1003–n/a.

[28] Gettelman, Salby, M. L., & Sassi, F. (2002). Distribution and influence of convection in the tropical tropopause region. *J. Geophys. Res. Atmos.,* **107(D10)**, ACL 6–1–ACL 6–12.

[29] Ghaderpour, E. (2021). JUST: MATLAB and python software for change detection and time series analysis. *GPS Solut.*, **25(3)**.

[30] Ghaderpour, Ince, E. S., & Pagiatakis, S. D. (2018). Least-squares cross-wavelet analysis and its applications in geophysical time series. *J. Geod.,* **92(10)**, 1223–1236.

[31] Ghaderpour, E., & Pagiatakis, S. D. (2019). LSWAVE: a MATLAB software for the least-squares wavelet and cross-wavelet analyses. *GPS Solut.*, **23(2)**.

[32] Ghaderpour, & Pagiatakis, S. D. (2017). Least-squares wavelet analysis of unequally spaced and non-stationary time series and its applications. *Math. Geosci.,* **49(7)**, 819–844.

[33] Goody, Walker, J. C. G., & Walker, J. C. G. (1972). *Atmospheres.* Prentice-Hall.

[34] Guo, J., Wang, Z., Zheng, J., Cui, J., Wei, Y., & Wan, W. (2019). Unusual Multiple Excitation of Large-Scale Gravity Waves by Successive Stream Interactions: The Role of Alfvenic Fluctuations. J. Geophy. Res. Space Phys., **124(7)**, 6281 –6287.

[35] Hand. (2015). WEATHER FORECASTING. CubeSats promise to fill weather data gap. *Sci. (American Association for the Advancement of Science)*, **350(6266)**, 1302–.

[36] Hajj, Ao, C. O., Iijima, B. A., Kuang, D., Kursinski, E. R., Mannucci, A. J., Meehan, T. K., Romans, L. J., de la Torre Juarez, M., & Yunck, T. P. (2004). CHAMP and SAC-C atmospheric occultation results and intercomparisons. *J. Geophys. Res.,* **109(D6)**, D06109-n/a.

[37] Healy, S. (2017). *GPS radio occultation: Principles and NWP use* [PowerPoint slides]. Radio Occultation Meteorology Satellite Application Facility.

[38] Hersbach, Bell, B., Berrisford, P., Hirahara, S., Horányi, A., Muñoz‐Sabater, J., Nicolas, J., Peubey, C., Radu, R., Schepers, D., Simmons, A., Soci, C., Abdalla, S., Abellan, X., Balsamo, G., Bechtold, P., Biavati, G., Bidlot, J., Bonavita, M., … Thépaut, J. (2020). The ERA5 global reanalysis. *Q. J. R. Meteorol.,* **146(730)**, 1999–2049.

[39] Hewitt, & Jackson, A. V. (2003). *Handbook of atmospheric science.* Blackwell Pub.

[40] Hindley, Wright, C. J., Smith, N. D., & Mitchell, N. J. (2015). The southern stratospheric gravity wave hot spot: individual waves and their momentum fluxes measured by COSMIC GPS-RO. *Atmos. Chem. Phys.,* **15(14)**, 7797–7818.

[41] Hoffmann, L., Wu, X., & Alexander, M. J. (2018). Satellite observations of stratospheric gravity waves associated with the intensification of tropical cyclones. *Geophys. Res. Lett.,* **45**, 1692–1700.

[42] Hoinka. (1999). Temperature, humidity, and wind at the global tropopause. *Monthly Weather Review*, **127(10)**, 2248–2265.

[43] Hung, & Kuo, J.P. (1978). Ionospheric observation of gravity-waves associated with Hurricane Eloise. *J. Geophys.,* **45(1)**, 67 -80.

[44] Innerkofler, Kirchengast, G., Schwärz, M., Marquardt, C., and Andres, Y.(2003). GNSS radio occultation excess phase processing for climate applications including uncertainty estimation, *Atmos. Meas. Tech. Discuss.* [Preprint under review].

[45] Jenkins, & Watts, D. G. (1968). *Spectral analysis and its applications.* Holden-Day.

[46] Khaykin, Funatsu, B. M., Hauchecorne, A., Godin-Beekmann, S., Claud, C., Keckhut, P., Pazmino, A., Gleisner, H., Nielsen, J. K., Syndergaard, S., & Lauritsen, K. B. (2017). Postmillennium changes in stratospheric temperature consistently resolved by GPS radio occultation and AMSU observations: Temperature Change from GPS-RO and AMSU. *Geophys. Res. Lett.,* **44(14)**, 7510–7518.

[47] Kim, & Chun, H.-Y. (2010). Stratospheric Gravity Waves Generated by Typhoon Saomai (2006): Numerical Modeling in a Moving Frame Following the Typhoon. *J. Atmos. Sci.,* **67(11)**, 3617–3636.

[48] Kim, Chun, H.-Y., & Baik, J.-J. (2007). Sensitivity of typhoon-induced gravity waves to cumulus parameterizations: Sensitivity of typhoon-induced gravity waves. *Geophys. Res. Lett.,* **34(15)**.

[49] Kim, Chun, H.-Y., & Baik, J.-J. (2005). A numerical study of gravity waves induced by convection associated with Typhoon Rusa. *Geophys. Res. Lett.,* **32(24)**, L24816–n/a.

[50] Kim, Chun, H.-Y., & Wu, D. L. (2009). A study on stratospheric gravity waves generated by Typhoon Ewiniar: Numerical simulations and satellite observations. *J. Geophys. Res.,* **114(D22)**.

[51] Kishore, Venkat Ratnam, M., Namboothiri, S. P., Velicogna, I., Basha, G., Jiang, J. H., Igarashi, K., Rao, S. V. B., & Sivakumar, V. (2011). Global (50°S–50°N) distribution of water vapor observed by COSMIC GPS RO: Comparison with GPS radiosonde, NCEP, ERA-Interim, and JRA-25 reanalysis data sets. *J. Atmos. Sol. Terr. Phys.,* **73(13)**, 1849–1860.

[52] Krisch, Ern, M., Hoffmann, L., Preusse, P., Strube, C., Ungermann, J., Woiwode, W., & Riese, M. (2020). Superposition of gravity waves with different propagation characteristics observed by airborne and space-borne infrared sounders. *Atmos. Chem. Phys.,* **20(19)**, 11469–11490.

[53] Kuester, Alexander, M. J., & Ray, E. A. (2008). A Model Study of Gravity Waves over Hurricane Humberto (2001). *J. Atmos. Sci.,* **65(10)**, 3231–3246.

[54] Kuettner, Hildebrand, P. A., & Clark, T. L. (1987). Convection waves: Observations of gravity wave systems over convectively active boundary layers. *Q. J. R. Meteorol.,* **113(476)**, 445–467.

[55] Lane, & Reeder, M. J. (2001). Convectively generated gravity waves and their effect on the cloud environment. *J. Atmos. Sci.,* **58(16)**, 2427–2440.

[56] Lu, Chu, X., Fong, W., Chen, C., Yu, Z., Roberts, B. R., & McDonald, A. J. (2015). Vertical evolution of potential energy density and vertical wave number spectrum of Antarctic gravity waves from 35 to 105km at McMurdo (77.8°S, 166.7°E). *J. Geophys. Res. Atmos.,* **120(7)**, 2719–2737.

[57] Majdzadeh, M. (2017). *Gravity wave generation and momentum deposition in the atmosphere* [Doctoral dissertation]. York University.

[58] Mallat, S. (1999). *A wavelet tour of signal processing.* Academic Press, Cambridge (2nd edition)

[59] Markowski, & Richardson, Y. (2010). *Mesoscale meteorology in midlatitudes.* Wiley-Blackwell.

[60] Nicholls, Pielke Sr., R. A., Wheeler, D., Carrio, G., & Smith, W. P. (2018). A numerical modelling investigation of the role of diabatic heating and cooling in the development of a mid-level vortex prior to tropical cyclogenesis – Part 1: The response to stratiform components of diabatic forcing. *Atmos. Chem. Phys.,* **18(19)**, 14393–14416.

[61] Noh, Cheon, W. G., Hong, S. Y., & Raasch, S. (2003). Improvement of the K-profile model for the planetary boundary layer based on large eddy simulation data. *Boundary-Layer Meteorology*, **107(2)**, 401–427.

[62] Nolan. (2007). What is the trigger for tropical cyclogenesis? *Australian Meteorological Magazine,* **56(4)**, 241–266.

[63] Nolan. (2020). An Investigation of Spiral Gravity Waves Radiating from Tropical Cyclones Using a Linear, Nonhydrostatic Model. *J. Atmos. Sci.,* **77(5)**, 1733–1759.

[64] Mukherjee, R, P. S., Parihar, N., Ghodpage, R., & Patil, P. T. (2010). Studies of the wind filtering effect of gravity waves observed at Allahabad (25.45°N, 81.85°E) in India. *Earth, Planets, and Space,* **62(3)**, 309–318.

[65] Müller, S. K., Manzini, E., Giorgetta, M., Sato, K., & Nasuno, T. (2018). Convectively Generated Gravity Waves in High Resolution Models of Tropical Dynamics. *J. Adv. Model. Earth Syst.*, **10(10)**, 2564–2588.

[66] Pagiatakis. (1999). Stochastic significance of peaks in the least-squares spectrum. *J. Geod.,* **73(2)**, 67–78.

[67] Pahlavan, H. A., Wallace, J. M., & Fu, Q. (2023). Characteristics of Tropical Convective Gravity Waves Resolved by ERA5 Reanalysis. *J. Atmos. Sci.*, **80(3)**, 777–795.

[68] Rauthe, Gerding, M., & Lübken, F.-J. (2008). Seasonal changes in gravity wave activity measured by lidars at mid-latitudes. *Atmos. Chem. Phys.,* **8(22)**, 6775–6787.

[69] Rhome, J. R. (2008, October 15). Tropical Cyclone Report Hurricane Bertha.

[70] Rogers, Zhang, J. A., Zawislak, J., Jiang, H., Alvey, G. R., Zipser, E. J., & Stevenson, S. N. (2016). Observations of the Structure and Evolution of Hurricane Edouard (2014) during Intensity Change. Part II: Kinematic Structure and the Distribution of Deep Convection. *Monthly Weather Review*, **144(9)**, 3355–3376.

[71] Ryu, J.-H., & Lee, S. (2010). Effect of Tropical Waves on the Tropical Tropopause Transition Layer Upwelling. *J. Atmos. Sci.*, **67(10)**, 3130–3148.

[72] Sayed, A. M. (2014). *Internal gravity waves and convection generated by a thermal forcing in the atmosphere* [Doctoral dissertation]. Carleton University.

[73] Shi, Hu, X., Yao, Z., Guo, W., Sun, M., & Gong, X. (2021). Case study on stratospheric and mesospheric concentric gravity waves generated by deep convection. *Earth and Planetary Physics*, **5(1)**, 79–89.

[74] Smith, & Montgomery, M. T. (2016). Understanding hurricanes. *Weather,* **71(9)**, 219–223.

[75] Smith, & Weintraub, S. (1953). The Constants in the Equation for Atmospheric Refractive Index at Radio Frequencies. *Proceedings of the IRE,* **41(8)**, 1035–1037.

[76] Song, & Chun, H.-Y. (2005). Momentum flux spectrum of convectively forced internal gravity waves and its application to gravity wave drag parameterization. Part I: Theory. *J. Atmos. Sci.,* **62(1)**, 107–124.

[77] Song, B. ‐G., Song, I. ‐S., Chun, H. ‐Y., Lee, C., Kam, H., Kim, Y. H., Kang, M. ‐J., Hindley, N. P., & Mitchell, N. J. (2021). Activities of Small ‐Scale Gravity Waves in the Upper Mesosphere Observed From Meteor Radar at King Sejong Station, Antarctica (62.22°S, 58.78°W) and Their Potential Sources. *J. Geophys. Res. Atmos.*, **126(10).**

[78] Steiner, & Kirchengast, G. (2000). Gravity Wave Spectra from GPS/MET Occultation Observations. *J. Atmos. Ocean. Technol.,* **17(4)**, 495–503.

[79] Strelnikova, Almowafy, M., Baumgarten, G., Baumgarten, K., Ern, M., Gerding, M., & Lübken, F.-J. (2021). Seasonal Cycle of Gravity Wave Potential Energy Densities from Lidar and Satellite Observations at 54° and 69°N. *J. Atmos. Sci.,* **78(4),** 1359–1386.

[80] Stull. (1976). Internal Gravity Waves Generated by Penetrative Convection. *J. Atmos. Sci.,* **33(7),** 1279–1286.

[81] Stull. (1988). *An introduction to boundary layer meteorology.* Kluwer Academic Publishers.

[82] Sutherland. (1999). Propagation and reflection of internal waves. *Physics of Fluids (1994)*, **11(5)**, 1081–1090.

[83] Taylor, Ryan, E. H., Tuan, T. F., and Edwards, R. (1993), Evidence of preferential directions for gravity wave propagation due to wind filtering in the middle atmosphere, *J. Geophys. Res.,* **98(A4),** 6047– 6057, doi:10.1029/92JA02604.

[84] Tory, & Dare, R. A. (2015). Sea Surface Temperature Thresholds for Tropical Cyclone Formation. *J. Clim.,* **28(20)**, 8171–8183.

[85] Tory, Montgomery, M. T., Davidson, N. E., & Kepert, J. D. (2006). Prediction and diagnosis of tropical cyclone formation in an NWP system. Part II: A diagnosis of tropical cyclone Chris formation. *J. Atmos. Sci.,* **63(12),** 3091–3113.

[86] Tsuda, Lin, X., Hayashi, H., and Noersomadi, (2011). Analysis of vertical wave number spectrum of atmospheric gravity waves in the stratosphere using COSMIC GPS radio occultation data, *Atmos. Meas. Tech.,* **4**, 1627–1636.

[87] Vergados, Luo, Z. J., Emanuel, K., & Mannucci, A. J. (2014). Observational tests of hurricane intensity estimations using GPS radio occultations. *J. Geophys. Res. Atmos.,* **119(4)**, 1936–1948.

[88] Vergados, Mannucci, A. J., & Su, H. (2013). A validation study for GPS radio occultation data with moist thermodynamic structure of tropical cyclones. *J. Geophys. Res. Atmos.,* **118(16)**, 9401–9413.

[89] Wang, Zhang, L., Wang, Y., & Zhang, Y. (2021). Influences of the Mid ‐Latitude Westerly Trough on Stratospheric Gravity Waves Generated by Typhoon Lekima (2019). *J. Geophys. Res. Atmos.,* **126(23)**.

[90] Wells, D., Vaníček, P., Pagiatakis, S., (1985). Least squares spectral analysis revisited. *Department of Geodesy & Geomatics Engineering Technical Report 84,* University of New Brunswick, Canada

[91] Wright, & Banyard, T. P. (2020). Multidecadal Measurements of UTLS Gravity Waves Derived From Commercial Flight Data. *J. Geophys. Res. Atmos.,* **125(19)**.

[92] Wu, Hoffmann, L., Wright, C. J., Hindley, N. P., Kalisch, S., Alexander, M. J., & Wang, Y. (2022). Stratospheric Gravity Waves as a Proxy for Hurricane Intensification: A Case Study of Weather Research and Forecast Simulation for Hurricane Joaquin. *Geophys. Res. Lett.,* **49(1)**.

[93] Xu, Yue, J., Xue, X., Vadas, S. L., Miller, S. D., Azeem, I., Straka, W., Hoffmann, L., & Zhang, S. (2019). Dynamical Coupling Between Hurricane Matthew and the Middle to Upper Atmosphere via Gravity Waves. *J. Geophys. Res. Space Phys.,* **124(5)**, 3589–3608.

[94] Yano. (2021). Initiation of deep convection through deepening of a well‐mixed boundary layer. *Q. J. R. Meteorol.,* **147(739)**, 3085‐3095.

[95] Zhao, Deng, Y., Wang, J., Zhang, S., & Lin, C. Y. (2020). Tropical Cyclone‐Induced Gravity Wave Perturbations in the Upper Atmosphere: GITM‐R Simulations. *J. Geophys. Res. Space Phys.,* **125(7)**.

[96] Zhao, Hu, X., Pan, W., Yan, Z., & Guo, W. (2022). Mesospheric Gravity Wave Potential Energy Density Observed by Rayleigh Lidar above Golmud (36.25° N, 94.54° E), Tibetan Plateau. *Atmos,* **13(7)**, 1084-.

Appendix A

Algorithms of Least Squares Spectral Analysis and Wavelet Analysis

Least Squares Spectral Analysis (LSSA) computes the optimum spectrum of an unequally or equally spaced time (data) series with some of the constituents of known forms (Wells et al., 1985). In the case of a time series, given a vector $\underline{t}$ with a series of observation times, a vector $\underline{f(t)}$ with a series of observed values and a vector $\underline{\omega}$ with frequencies for which the spectral values are required, the vector $\underline{s(\omega)}$ of the spectral values can be computed.

The computation of the spectrum fits sinusoids (the base functions) to the input signal, where the base functions are tabulated as an orthogonal matrix $\underline{\Phi}$ and the observations $\underline{f}$ follows:

$$\underline{f} = \underline{\Phi c}\,. \tag{1}$$

Here the designed matrix $\underline{\Phi}$ models the relationship between the observations $\underline{f}$ and the unknow parameters $\underline{c}$. The LSSA aims to find the best fitting estimation $\underline{p}$ to $\underline{f}$ with an estimated coefficients $\underline{\hat{c}}$, where $\underline{p}$ reads as:

$$\underline{p} = \underline{\Phi \hat{c}}\,, \tag{2}$$

so that the residuals $\underline{\hat{v}} = \underline{f} - \underline{p}$ is minimized following the least squares approach.

The spectral values $\underline{s}$ are considered as a measure of the fractional content of $\underline{f}$ that is represented by the frequency $\underline{\omega}$. Therefore, the spectral values $\underline{s}$ can be computed via:

$$\underline{s} = \frac{\underline{f}^T \underline{p}}{\underline{f}^T \underline{f}} \,. \tag{3}$$

JUST software (Ghaderpour, 2021) implements the algorithm of the LSSA method. By imputing the observation times and the observation values with a frequency band of interest, the estimated frequency spectrum can be computed as the output from the software. Based on the choice of significance level α (usually 0.01 or 0.05), a critical value is also calculated for the spectrum, above which the spectral peaks are considered as statistically significant. Advanced options are also provided to consider the weight, trend or possible gaps of the input signal (Pagiatakis, 1999; Ghaderpour, 2021).

Similarly, the Least Square Wavelet Analysis (LSWA) computes the spectrogram for any non-stationary and equally or unequally time (data) series with an associated covariance matrix. To be specific, the LSWA decomposes a time series into the time-frequency domain, which allows the detection of the short-duration signals as well as signals with a changing frequency and/or amplitude (Ghaderpour & Pagiatakis, 2018). More information on the concepts of the wavelet analysis can be found in Mallat (1999).

The computation of the spectrogram requires a proper segmentation of the input series with a designed, translating window to calculate the spectral peaks for each segment based on the LSSA method (ibid., 2018). The determination of the window size (number of data points) and window length (length in the time or space domain) differ for an equally-spaced and an unequally-spaced series.

The LSWAVE software (Ghaderpour & Pagiatakis, 2019) is designed for the LSWA approach. Given the same input as the JUST software and an additional information of

the desired time resolution for the output, the spectrogram can be computed as well as a stochastic surface that demonstrates the statistical confidence level. Advanced options are also provided to enter the known forms of the constituents and the numerical constants that determine the translating window characteristics (ibid., 2019).